

Dissertation in Physics
submitted to the
Combined Faculties of the Natural Sciences and Mathematics
of the Ruperto-Carola University of Heidelberg, Germany.
for the degree of
Doctor of Natural Sciences

presented by
M. Sc. Physics. *Marik Barnabé Heider*
born in Laval, Canada

Oral examination: 27.05.2009, 14:00 pm

**Performance and stability tests
of bare high purity germanium
detectors in liquid argon
for the GERDA experiment**

Referees: Prof. Dr. Wolfgang Hampel
Prof. Dr. Karl-Tasso Knöpfle

Abstract

GERDA will search for neutrinoless double beta decay of ^{76}Ge by using a novel approach of bare germanium detectors in liquid argon (LAr). Enriched germanium detectors from the previous Heidelberg-Moscow and IGEX experiments have been reprocessed and will be deployed in GERDA Phase-I. At the center of this thesis project is the study of the performance of bare germanium detectors in cryogenic liquids. Identical detector performance as in vacuum cryostats (2.2 keV FWHM at 1.3 MeV) was achieved in cryogenic liquids with a new low-mass detector assembly and contacts. One major result is the discovery of a radiation induced leakage current (LC) increase when operating bare detectors with standard passivation layers in LAr. Charge collection and build-up on the passivation layer were identified as the origin of the LC increase. It was found that diodes without passivation do not exhibit this feature. Three month-long stable operation in LAr at ~ 5 pA LC under periodic gamma irradiation demonstrated the suitability of the modified detector design. Based on these results, all Phase-I detectors were reprocessed without passivation layer and subsequently successfully characterized in LAr in the GERDA underground Detector Laboratory. The mass loss during the reprocessing was ~ 300 g out of 17.9 kg and the exposure above ground ~ 5 days. This results in a negligible cosmogenic background increase of $\sim 5 \cdot 10^{-4}$ cts/(keV·kg·y) at ^{76}Ge $Q_{\beta\beta}$ for ^{60}Co and ^{68}Ge .

Zusammenfassung

Das GERDA Experiment wird nach dem neutrinolessen Doppelbetazerfall von ^{76}Ge suchen. Dazu wird der neue Ansatz verfolgt, nackte Germaniumdetektoren in flüssigem Argon (LAr) zu betreiben. Angereicherte Germaniumdetektoren aus den vorangegangenen Heidelberg-Moskau und IGEX Experimenten wurden überarbeitet und werden in GERDA Phase-I eingesetzt. Im Mittelpunkt dieser Dissertation steht die Untersuchung der Leistungsfähigkeit nackter Germaniumdetektoren in tiefkalten Flüssigkeiten. Mit einer neuen nieder-massigen Detektorhalterung und Kontaktierung wurde in tiefkalter Flüssigkeit die gleiche Detektorleistung wie in Vakuum-Kryostaten (2.2 keV FWHM bei 1.3 MeV) erzielt. Eine wichtige Entdeckung ist der Anstieg von strahlungsinduziertem Leckstrom (LC) bei dem Betrieb der Detektoren mit üblichen Passivierungsschichten (PS) in LAr. Als Ursache des Leckstromanstiegs wurden Ladungssammlung und -anhäufung auf der PS ausgemacht. Es wurde gezeigt, dass Dioden ohne PS dieses Merkmal nicht aufweisen. Ein dreimonatiger stabiler Betrieb in LAr bei ~ 5 pA LC unter regelmässiger Gammabestrahlung zeigte die Eignung des modifizierten Detektoraufbaus. Basierend auf diesen Ergebnissen wurden alle Phase-I Detektoren ohne PS überarbeitet und anschliessend erfolgreich in LAr im GERDA Detektorlabor charakterisiert. Der Masseverlust während der Überarbeitung betrug ~ 300 g von 17.9 kg bei einer oberirdischen Strahlenbelastung von ~ 5 Tagen. Damit ergibt sich eine vernachlässigbare Zunahme des kosmogenen Untergrunds von $\sim 5 \cdot 10^{-4}$ cts/(keV·kg·y) bei ^{76}Ge $Q_{\beta\beta}$ für ^{60}Co und ^{68}Ge .

Contents

1	Introduction	11
1.1	Neutrino masses and neutrinoless double beta decay	11
1.2	Experimental constraints	14
1.3	The GERDA experiment	17
1.4	Operation of bare germanium detectors in cryogenic liquid	20
1.5	Thesis overview	21
2	GERDA Phase-I detector assembly design	23
2.1	Introduction to high purity germanium detectors	23
2.1.1	Properties of germanium	24
2.1.2	Semiconductor detector principle	25
2.1.3	Germanium detector technology	26
2.2	GERDA Phase-I detector design	28

2.3	Design of Phase-I low-mass holder and contacts	30
2.4	Studies of the detector assembly performance	32
2.4.1	Mounting procedure	33
2.4.2	Test of mechanical stability	34
2.4.3	Test of electrical contact quality	34
2.4.4	First spectroscopy measurement at the detector manufacturer . . .	36
2.4.5	Conclusion	37
3	Study of germanium detectors in the GERDA underground Detector Laboratory	39
3.1	Infrastructures of GDL	39
3.2	Experimental set-up	40
3.2.1	Liquid argon/liquid nitrogen test benches	40
3.2.2	Electronic read-out	44
3.3	Handling of germanium diode	45
3.3.1	Mounting procedure	45
3.3.2	Procedure to cool down and warm up detector assemblies	46
3.3.3	Storage of the diodes	48
3.4	Optimization of the bare detector performance in the test benches	49
3.4.1	Results of leakage current measurements	49
3.4.2	Results of spectroscopic measurements	49
3.5	Conclusion	56
4	Investigation of the leakage current response of bare detectors in liquid argon and liquid nitrogen to γ-radiation	57
4.1	Introduction	57

4.2	Leakage current studies with a prototype detector with a full passivation layer	59
4.2.1	Gamma-radiation induced increase of leakage current in liquid argon	59
4.2.2	Reversibility of the γ -radiation induced leakage current	62
4.2.3	Role of the passivation layer in the γ -radiation induced leakage current	63
4.3	Leakage current studies with prototype detectors with modified groove passivation procedures	65
4.4	Dependence of the γ -radiation induced leakage current on high voltage polarity	67
4.5	Irradiation measurement summary	69
4.6	Explanation of the γ -radiation induced leakage current	75
4.6.1	Electric field calculation	75
4.6.2	Charge production in LAr	75
4.6.3	Charge collection on the passivation layer	76
4.6.4	Conductivity of the passivation layer	78
4.6.5	Ultraviolet curing effect	79
4.7	Discussion	79
4.8	Conclusions	80
5	Long-term stability tests with bare detectors in liquid argon	81
5.1	First stability measurement with Prototype 1	81
5.1.1	Search for neutrinoless double electron capture of ^{36}Ar	83
5.2	Six month stability measurement with the first prototype in liquid argon .	84
5.3	Long-term stability measurements with Prototype 2 and Prototype 3 . . .	86
5.4	Conclusion	88
6	Preparation of the existing HPGe diodes for Phase-I of GERDA	89

6.1	Characterization of the Phase-I diodes prior to their modifications for GERDA	89
6.1.1	Dimensions and masses of the enriched diodes	92
6.1.2	Natural germanium diodes from GENIUS-TF	96
6.2	Reprocessing of the Phase-I diodes at the detector manufacturer	96
6.2.1	Dimensions and masses of the diodes after reprocessing	97
6.2.2	Characterization of the detectors at the manufacturer site after the reprocessing	100
6.3	Internal background of the enriched diodes from cosmogenic ^{60}Co and ^{68}Ge production	104
6.4	Conclusion	107
7	Characterization of the Phase-I detectors in liquid argon	109
7.1	Mounting of the diodes in their low-mass holders	109
7.2	Investigation of the detector performance	111
7.2.1	Current-Voltage curve measurements	111
7.2.2	Operational voltage measurement	116
7.2.3	Study of the spectroscopic performance	120
7.3	Measurement of the active masses	122
7.4	Conclusion	128
8	Summary and outlook	129
A	Heidelberg-Moscow and IGEX cryostats and detector holders	143
B	Phase-I detector holders and contacts	153

1.1 Neutrino masses and neutrinoless double beta decay

According to the Standard Model of particle physics, neutrinos are massless fermions. The neutrinos, always left-handed, and the anti-neutrinos, always right-handed, are different particles. There are three known flavors of neutrino, each associated to a charged lepton (e and ν_e , μ and ν_μ , τ and ν_τ). Neutrinos interact with matter only in weak processes through the exchange of charged and neutral bosons (W^\pm and Z^0). In the standard electroweak model, the total lepton number and the individual flavor lepton numbers are conserved [1].

However, results from atmospheric [2], solar [3], reactor [4] and accelerator [5] neutrino oscillation experiments have convincingly shown that neutrinos have a finite mass, indicating new physics beyond the Standard Model. Neutrino oscillation occurs because the detectable neutrino flavor eigenstates $|\nu_l\rangle$ are not equal to the mass eigenstates $|\nu_j\rangle$ but are a superposition of those:

$$|\nu_l\rangle = \sum_j U_{lj} |\nu_j\rangle, \quad (1.1)$$

where $l = e, \mu, \tau$, $j = 1, 2, 3$ and U_{lj} represents the Pontecorvo-Maki-Nakagawa-Sakata (PMNS) mixing matrix [6]. In contrast to what is predicted by the Standard Model, the individual lepton numbers are not conserved. Neutrino propagation can be described by a plane wave and the probability that a neutrino of flavor α will be observed as flavor β after a traveled distance L is given by

$$P_{\alpha \rightarrow \beta} = |\langle \nu_\beta | \nu_\alpha(t) \rangle|^2 = \left| \sum_j U_{\alpha j}^* U_{\beta j} e^{\frac{-im_j^2 L}{2E}} \right|^2, \quad (1.2)$$

with m_j and E the mass and the energy of the mass-eigenstate j . The oscillation probability between neutrino types at a given time depends on the differences in the absolute squared-masses. This is valid for pure vacuum oscillations. Because of the presence of electrons and the absence of muons and tauons in ordinary matter, the propagation of neutrinos is different in matter than in vacuum. This results in an additional potential in the equation of propagation which changes the oscillation probability of neutrinos in matter. The propagation of a neutrino through a medium of varying density is accompanied by resonant oscillation phenomena, described by the Mikheev-Smirnov-Wolfenstein effect [7].

Until now, the questions concerning the nature of the neutrino, namely its charge conjugation property, and the mechanisms of neutrino mass generation remain unanswered. While the charged leptons are Dirac particles, the neutrino may be the only fermion identical to its own anti-particle, as predicted by Ettore Majorana. Neutrino can have a Dirac or a Majorana mass term, or a mixture of both. Dirac fermions are four-component objects including helicity and charge (not necessary electrical) states. The particles can be distinguished from their anti-particles and the total lepton number remains a conserved quantity. In contrast, Majorana fermions are two-component objects. Since the neutrino has no electrical charge, the lepton number is the only indicator to differentiate a neutrino from an anti-neutrino. Because the neutrino has mass, its speed is always lower than the speed of light. Theoretically, an observer can move faster than the left-handed neutrino and see a right-handed anti-neutrino. There is no way to distinguish between a particle and its anti-particle, and the total lepton number is violated. The Majorana nature of the neutrino ($\nu_i = \nu_i^c = C\bar{\nu}_i^T$ where ν_i^c is the charge conjugate and C the charge conjugation operator) is predicted by most of the mechanisms trying to explain neutrino masses [8].

Although neutrino oscillation experiments provide differences of neutrino masses, they do not infer the absolute magnitude of the masses and cannot separate different scenarios. For the mass hierarchy there are three possible cases: the normal hierarchy $m_1 < m_2 < m_3$, the inverted hierarchy $m_3 < m_1 < m_2$ and the degenerate mass scale where the lightest neutrino mass is large compared to the mass differences. The oscillation experiment results cannot infer either about the properties of the neutrino under charge conjugation. Neutrinoless double beta ($0\nu\beta\beta$) decay is the only feasible process that enables to test experimentally the Majorana nature of neutrinos. In addition, it could give information on the absolute mass scale.

The double beta-decay ($\beta\beta$) is observable in some even-even nucleus configurations if the simple beta-decay is forbidden because the neighbor isobar has less binding energy. It is expected in approximately 60 nuclei, including ^{76}Ge (Fig.1.1). There are two basic modes

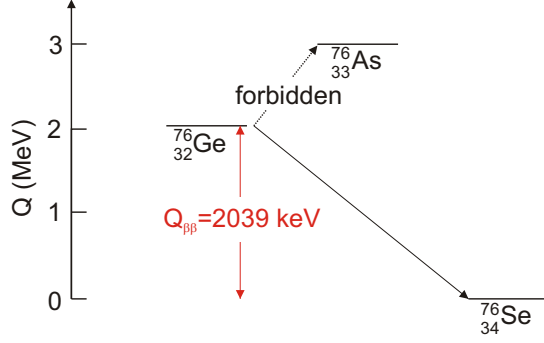


Figure 1.1: Energy scheme for the double beta decay from ^{76}Ge to daughter nucleus ^{76}Se . The single beta decay to the intermediate isotope ^{76}As is forbidden by the energy conservation law. The $Q_{\beta\beta}$ value is 2039 keV.

of $\beta\beta$ decay. The two neutrino mode

$$(A, Z) \rightarrow (A, Z + 2) + 2e^- + 2\bar{\nu} \quad (2\nu\beta\beta) \quad (1.3)$$

is a second-order weak interaction process, allowed in the Standard Model. So far, it has been observed in ten nuclei and proceeds with a typical half-life of $\sim 10^{20}$ years [9]. For ^{76}Ge , the half life is $T_{1/2} = (1.3 \pm 0.1) \cdot 10^{21}$ years [10]. In the neutrinoless mode

$$(A, Z) \rightarrow (A, Z + 2) + 2e^- \quad (0\nu\beta\beta) \quad (1.4)$$

only two electrons are emitted. This nuclear process, which is forbidden in the Standard Model, clearly violates the law of lepton number conservation. In $0\nu\beta\beta$ decay, one nucleon absorbs the neutrino emitted by another nucleon. This is possible only if the neutrino is a Majorana particle ($\nu \equiv \bar{\nu}$). Figure 1.2 shows the Feynman diagrams of the $\beta\beta$ decay processes. For the $0\nu\beta\beta$, only the simplest case of light Majorana neutrinos is considered. Other mechanisms (e.g. SUSY) can also generate such a process [11]. Experimentally, measuring the energy of the electrons allows to distinguish between the two modes. In the $2\nu\beta\beta$ mode, the sum energy spectrum is continuous and peaked below $Q_{\beta\beta}$. In the $0\nu\beta\beta$ mode, no neutrino is emitted, so both electrons share the full energy of the $Q_{\beta\beta}$ value. The two-electron spectrum is characterized by a discrete energy release higher than the continuous energy spectrum of the $2\nu\beta\beta$ decay (Fig.1.3). The half life of the $0\nu\beta\beta$ process is expressed as [12]:

$$(T_{1/2}^{0\nu})^{-1} = G^{0\nu}(E_0, Z) |M^{0\nu}|^2 |m_{ee}|^2. \quad (1.5)$$

The first term $G^{0\nu}(E_0, Z)$ is the calculable phase-space integral which depends on the $Q_{\beta\beta}$ value and includes Coulomb effect on the nuclear charge Z . The nuclear matrix $M^{0\nu}$ can

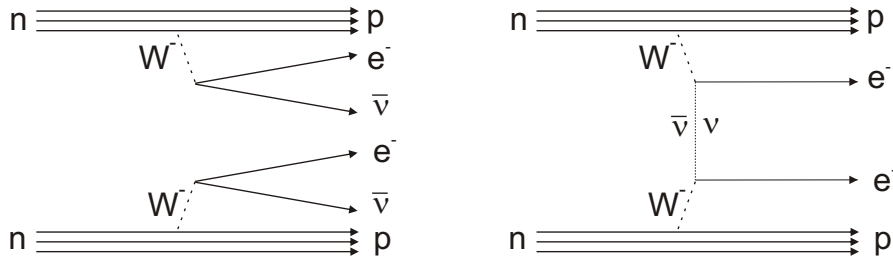


Figure 1.2: **Left:** Feynman diagram for $2\nu\beta\beta$ decay. **Right:** Feynman diagram for $0\nu\beta\beta$ decay under exchange of a massive Majorana neutrino.

be evaluated, but with considerable uncertainty. The absolute value of m_{ee} is called the effective mass. It is related to the mixing angles θ_{ij} from the PMNS matrix determined or constrained by the oscillation experiments, the absolute neutrino masses m_i and the so-called Majorana phase $\alpha(i)$:

$$|m_{ee}| = \left| \sum_j |U_{ej}|^2 e^{i\alpha(j)} m_j \right|, \quad (1.6)$$

where U_{ej} are the elements of the first row of the PMNS mixing matrix. In addition to confirm the Majorana nature of the neutrino and to give information on the absolute neutrino mass scale (i.e. the value of the smallest neutrino mass), observing $0\nu\beta\beta$ would potentially infer also on the neutrino mass hierarchy and the Majorana phases.

1.2 Experimental constraints

Observing $0\nu\beta\beta$ is very challenging since it must be detected above the inevitable presence of radioisotope traces which have similar decay energies but lifetimes more than 10 orders of magnitude shorter. The background is quoted in term of a background index (B), in units of cts/(keV·kg·y), in the relevant energy range. For a given background index, the effective neutrino mass scales as

$$|m_{ee}| \propto \left[\frac{B\Delta E}{MT} \right]^{1/4}, \quad \text{with background} \quad (1.7)$$

and if zero background is observed it varies as

$$|m_{ee}| \propto \frac{1}{\sqrt{MT}}, \quad \text{without background} \quad (1.8)$$

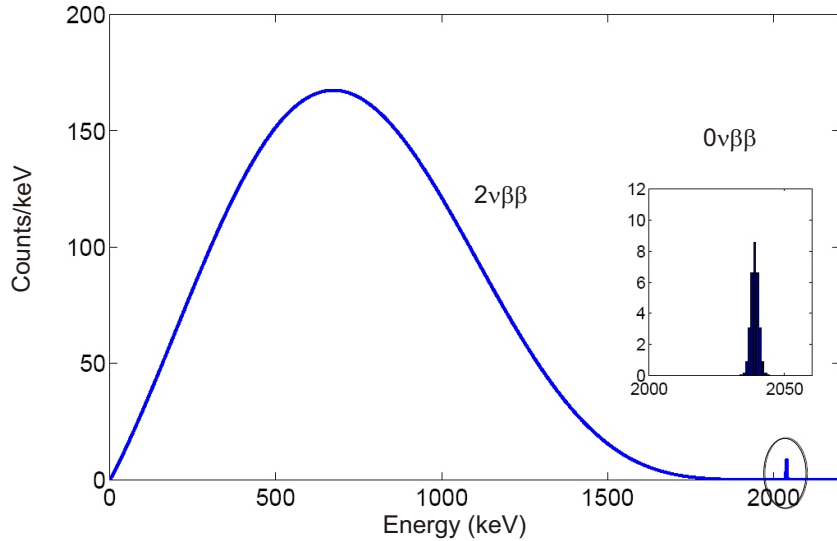


Figure 1.3: Spectrum of the sum of the electron kinetic energies for the $2\nu\beta\beta$ and $0\nu\beta\beta$ decays of ^{76}Ge corresponding to an exposure of 72 kg.y. The $2\nu\beta\beta$ continuum was calculated with a half-life of $1.7 \cdot 10^{21}$ years, and the peak at the $Q_{\beta\beta}$ value corresponds to $0\nu\beta\beta$ decay with a half-life of $1.2 \cdot 10^{25}$ years [13]. Here, the energy resolution is 3 keV (FWHM) at 2039 keV, typical for germanium detector.

where ΔE is the energy window, M is the mass of the isotope and T is the running time of the experiment. To achieve the best sensitivity, a detector must maximize the $0\nu\beta\beta$ count rate while suppressing the background. Therefore, it must be capable of good energy resolution. Any radioactive isotope which decays with greater energy than the $Q_{\beta\beta}$ value is a potential background. The radioactivity of the source, the detector and the shielding must be extremely low. These ultra-low background experiments must be located deep underground to protect the detectors from cosmic rays. It is also advantageous to use an isotope with a large $Q_{\beta\beta}$ value, a high matrix element and a long $2\nu\beta\beta$ half-life. Finally, the source material must be available in high purity and should contain a large fraction of the double beta decay isotope.

Numerous experiments have been carried out to search for $0\nu\beta\beta$ decay using different isotopes and different detection techniques: ionization detectors, scintillation detectors, tracking chambers, time projection chambers (TPC), cryogenic bolometers. The most sensitive experiments to date have been Heidelberg-Moscow (HdM) [14] and the International Germanium Experiment (IGEX) [15]. These experiments used conventional p-type high purity germanium (HPGe) detectors, enriched in ^{76}Ge to approximately 86%, operated in vacuum cryostats. Figures 1.4 and 1.5 show pictures of the HdM and IGEX

setups. Using radiopure materials, active and passive shieldings, and by operating in deep-underground laboratories these experiments reduced the background rate around 2039 keV to $\sim 10^{-1}$ counts/(keV·kg·y). Both experiments obtained similar limits: $T_{1/2} > 1.9 \cdot 10^{25}$ and $T_{1/2} > 1.6 \cdot 10^{25}$ years with 90% CL for HdM and IGEX, respectively. A subset of members of the Heidelberg-Moscow collaboration reanalyzed the HdM data and claimed evidence for $0\nu\beta\beta$ decay in ^{76}Ge with $T_{1/2} \approx 1.2 \cdot 10^{25}$ years, corresponding to $|m_{ee}| = 0.24 - 0.58$ eV [16]. This claim has been criticized by many in the nuclear and particle physics communities (e.g. [17]) and has in any case to be verified by other experiments.

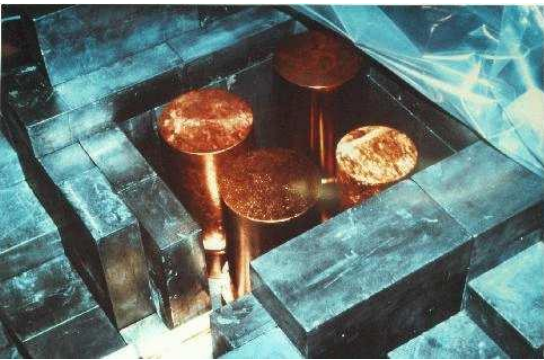


Figure 1.4: Four of the Heidelberg-Moscow detectors installed at the Laboratori Nazionali del Gran Sasso, Italy.



Figure 1.5: Photo of some IGEX detectors installed in the Canfranc underground laboratory, Spain.

A new generation of $0\nu\beta\beta$ experiments is starting. These experiments aim to probe the effective Majorana mass down to 0.1 eV and below. The most developed experiments which have the potential to reach the 50 meV region for the effective neutrino mass include CUORE [18] (TeO_2 bolometers), EXO [19] (Xe TPC), SuperNEMO [20] (Mo and Nd foils in plastic scintillator), GERDA [21] and Majorana [22] (HPGe detectors). In particular, germanium technology offers excellent capabilities and sensitivities for the search of $0\nu\beta\beta$:

- germanium acts as source and detector simultaneously,
- intrinsic HPGe is available and the possibility to enrich natural germanium from 7% to 86% in ^{76}Ge has been demonstrated in the past for the HdM and IGEX experiments,
- HPGe detectors have excellent energy resolution,
- powerful background rejection techniques are available (e.g. pulse shape analysis, segmentation),

- germanium spectrometry is a well understood technology and several large gamma ray spectrometer arrays (e.g. Gammasphere, TIGRESS, AGATA, GRETINA) already use this technology.

1.3 The GERDA experiment

GERmanium Detector Array (GERDA) is designed to search for $0\nu\beta\beta$ decay in ^{76}Ge by operating bare HPGe detectors enriched in ^{76}Ge in liquid argon (LAr) [21]. The high-purity LAr acts simultaneously as a cooling medium and as a shield against external radiation. The aim is to surpass the state-of-art in $0\nu\beta\beta$ sensitivity through one order of magnitude improvement in passive background reduction by shielding external radioactivity and minimizing the amount of material in the detector support structure. In addition, by operating HPGe detectors GERDA aims at an excellent energy resolution (3-4 keV at $Q_{\beta\beta}$).

GERDA is located at the depth of 3800 meters water equivalent at the Laboratori Nazionali del Gran Sasso (LNGS), Italy. The construction of the experiment started in 2008 and data taking will start in 2009. Figure 1.6 shows a schematic view of the experiment. GERDA uses LAr as a primary shield contained in a 70 m³ vacuum-isolated stainless steel

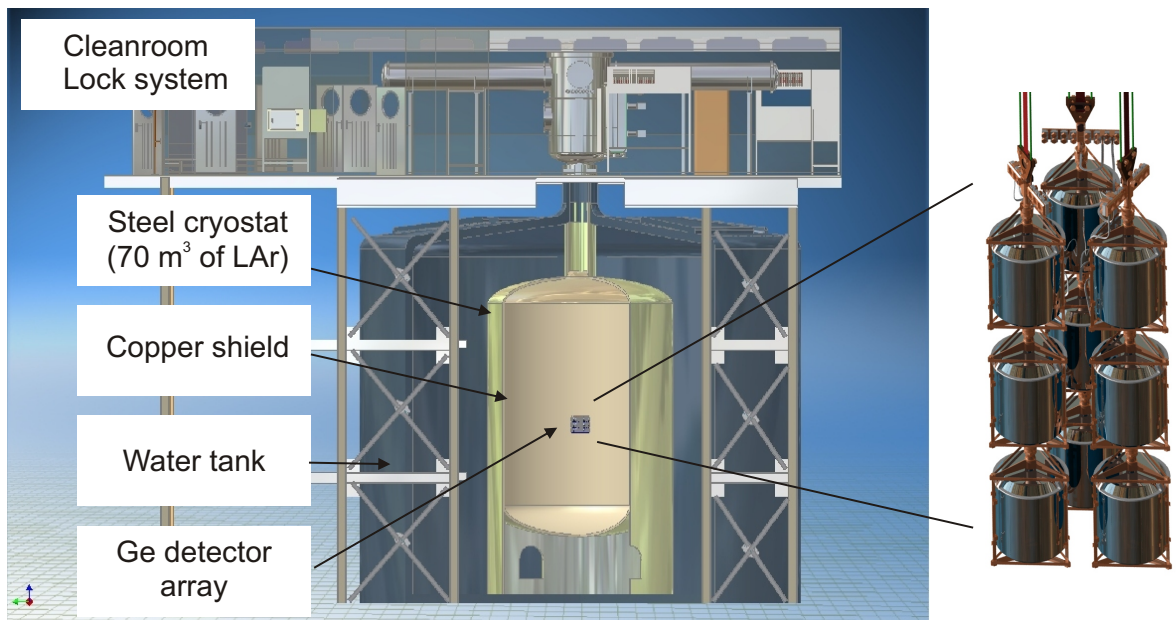


Figure 1.6: View of the GERDA experiment and the enriched HPGe detector array for the first phase of GERDA.

cryostat. Liquid argon can be purified to an extremely high degree [23]. Originally, both LAr and LN₂ filling was considered. On one hand, LAr is advantageous because of its higher stopping power due to its higher density ($\rho_{LAr} = 1.4$ kg/l, $\rho_{LN_2} = 0.8$ kg/l). On the other hand, the cosmogenic ³⁹Ar isotope introduces background, but at lower energies than $Q_{\beta\beta}$. As copper is more radiopure than stainless steel, it was first envisaged to operate the bare detectors in a copper cryostat. However, the safety concerns of the LNGS and the cost of such construction was too high. It led to the final design of a stainless steel cryostat lined with an additional copper layer at the level of the detector array and filled with LAr. The diameter of the cryostat is sufficient so the LAr shields the detectors from the low residual activity of the cryostat walls. The cryostat is located inside a tank filled with highly purified water (650 m³). The outer tank complements the shielding against γ -rays and neutrons from the surrounding environment. In addition, it is equipped with photomultipliers and serves as an active veto against cosmic muons. The detectors are assembled in a modular arrangement of strings. Each string contains three detectors mounted in a low-mass holder. The detector handling will be performed in a cleanroom environment. A lock and a suspension system on top of the cryostat allow to insert and remove the detectors without contaminating the vessel.

The GERDA experiment design reduces the background from external sources but contaminations intrinsic to the germanium detectors remain. Above ground, the germanium can be activated by radiation from cosmic rays which causes spallation in the germanium and produces a variety of radioactive isotopes. Some of them may contribute to the background at $Q_{\beta\beta}$. Most important are the decays of ⁶⁸Ge and ⁶⁰Co (see Chapter 6). Great care is taken to minimize the exposure of the germanium above ground. The enriched material is stored underground between all the detector processing steps.

The experiment will proceed in phases. In GERDA Phase-I, reprocessed enriched diodes from the HdM and IGEX experiments will be deployed. In total, 8 HPGe detectors (total mass ~ 18 kg) enriched in ⁷⁶Ge to 86% and 6 reprocessed natural HPGe detectors from Genius-TF [24] will be operated. A total background index of less than 10^{-2} cts/(keV·kg·y) should be achieved in Phase-I. Assuming an exposure of ~ 15 kg·y and an energy resolution of 3.6 keV, the expected number of background events is < 0.5 counts. If no event is observed, a $T_{1/2} > 3.0 \cdot 10^{25}$ y (90% C.L.) can be established with a detection efficiency of 95%. This results in an upper limit on the effective neutrino mass of $m_{ee} < (0.3 - 0.9)$ eV, depending on the nuclear matrix elements used [12]. Therefore, the Phase-I sensitivity should allow a statistically unambiguous statement concerning $0\nu\beta\beta$ with a lifetime around $1.2 \cdot 10^{25}$ y, corresponding to the claim of detection [16].

In GERDA Phase-II, new enriched diodes (~ 20 kg) will be added to achieve 100 kg·y of exposure within three years. Additional active background suppression techniques (e.g.

detectors with enhance pulse shape capability [25], detector segmentation [26], LAr scintillation light [27]) will be required to reduce the background index by one order of magnitude below 10^{-3} cts/(keV·kg·y). At the end of Phase-II, GERDA should reach a sensitivity of $T_{1/2} > 2 \cdot 10^{26}$. Depending on the achieved physics results, a ton scale experiment with a background index of $<10^{-4}$ cts/(keV·kg·y) is considered in the framework of a new worldwide collaboration (Phase-III).

Figure 1.7 shows the expected sensitivity of GERDA to the effective Majorana mass [28]. Phase-I and Phase-II are sensitive to the degenerate neutrino mass scenario. An hypothetical one ton experiment could be sensitive to the inverted ordering scenario (i.e. $m_2 > m_1 > m_3$).

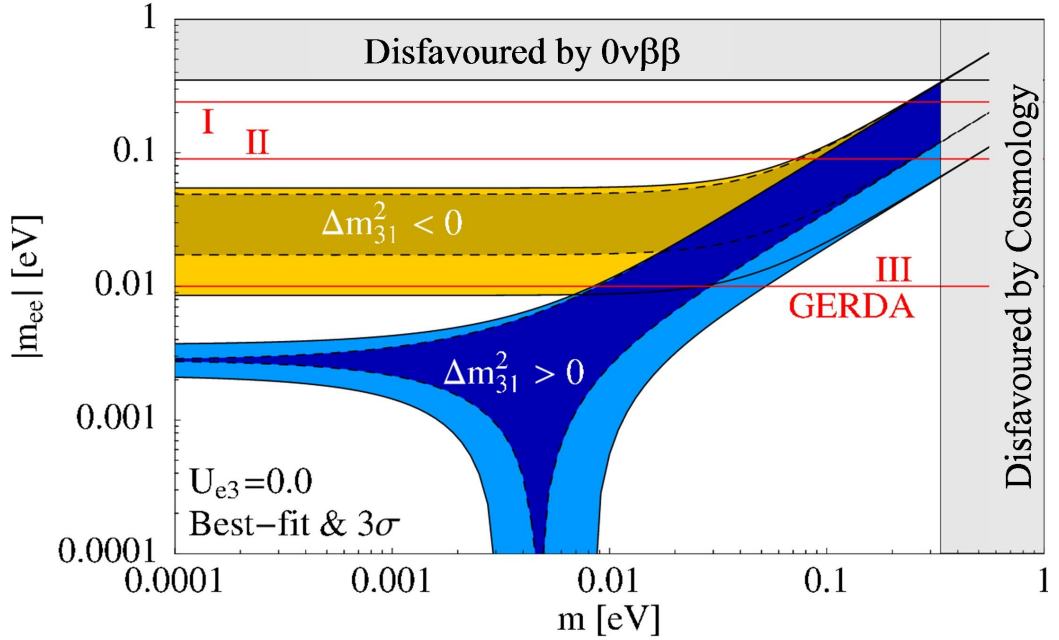


Figure 1.7: Effective Majorana mass $|m_{ee}|$ in function of the lightest neutrino mass m [28]. The expected sensitivity of the two phases of GERDA are shown (Phase-III refers to an hypothetical one ton experiment). The blue and yellow bands correspond respectively to the normal ($m_3 > m_2 > m_1$) and the inverted ($m_2 > m_1 > m_3$) mass ordering. Phase-I and Phase-II are sensitive to the degenerate neutrino masses (where the normal and the inverted ordering converge). The regions disfavoured up to date by $0\nu\beta\beta$ decay experiments and cosmology are indicated.

1.4 Operation of bare germanium detectors in cryogenic liquid

By operating bare germanium detectors inside a cryogenic fluid shield, the approach of GERDA follows an idea proposed several years ago in [29]. The result from the HdM experiment showed that the dominant background of the experiment was due to radioactivity external to the germanium, mainly to the copper cryostat [14]. Unlike solid materials, gases or liquids can be continuously purified. In the frame of the Borexino solar neutrino experiment [30], new radon purification techniques for liquid nitrogen (LN_2) were developed and the ^{222}Rn activity was reduced below $1 \mu\text{Bq}/\text{m}^3$ in the gas phase at standard temperature and pressure [31]. Moreover, bare HPGe diodes have been operated in LN_2 since many years at some detector manufacturers for short term tests. Consequently, the technique to operate with bare HPGe detectors in LN_2 was proposed to reduce the background by several order of magnitude with respect to conventionally operated detectors in vacuum cryostats. The great advantage is that the LN_2 which is very clean acts simultaneously as a cooling medium and a shield against external activities. The optimal operating temperature is maintained without the use of a standard vacuum cryostat and the external activity is outside the LN_2 volume.

This novel experimental concept was first considered in the GENIUS [32] and GEM [33] proposals. A first test with a bare detector in LN_2 was performed and the result indicated that the performance of the detector was comparable to a detector operated in a conventional vacuum cryostat [34]. Then, GENIUS-TF was constructed to test the feasibility of the full GENIUS project proposal [24]. In total, 6 HPGe detectors (total mass ~ 15 kg) were operated naked in LN_2 in the period from 2004 to 2006. After the successful start of the experiment with four naked detectors, significant problems were reported with a background from ^{222}Ra diffusing into the setup, and more importantly with an unacceptable increase of the detector leakage current. At the end of GENIUS-TF, none of the detectors was working at its operation voltage [35]. Obviously, it was necessary to study the performance and the stability of bare detectors in cryogenic liquid before the start of GERDA. The overall work presented in this thesis shows the feasibility of a long-term experiment with bare HPGe detectors submerged in LAr. It is the first time that this novel technique is applied in LAr.

1.5 Thesis overview

Prior to this work, the possibility to operate bare HPGe detectors for extended periods (\sim few years) without deteriorating the detector parameters was questioned. The results and measurements presented in this dissertation have significant impact on the GERDA experiment. For more than three years, tests have been performed with prototype detectors using the same technology as the Phase-I detectors. Tests were carried out at the detector manufacturer site and in the GERDA Detector underground Laboratory (GDL) at LNGS. During the test with the prototype detectors, the Phase-I detectors have been reprocessed at the detector manufacturer. Subsequently, the enriched diodes were mounted in their low-mass holders and the detector characterization in LAr was performed. We have operated more than ten detectors successfully, three of them for long-term measurements. We gained a lot of experience concerning the handling of HPGe diodes and the operation of bare detectors. The main scientific goal achieved with this research was to show the ability to operate bare HPGe detectors in LAr over a long time period.

Chapter 2 presents the detector technology, and the low-mass holder with the electrical contact scheme for GERDA Phase-I. In Chapter 3, GDL, the experimental setup, and the handling procedure are described. The performance of bare prototype detectors operated in the GDL test benches is also reported. Chapter 4 summarizes the study of the leakage current of detectors operated in LAr and in LN₂ under varying γ irradiations. Chapter 5, short but very important for GERDA, summarizes the long-term stability tests with different prototype detectors. Chapter 6 and 7 refer to the operations and measurements performed with the Phase-I enriched and non-enriched detectors in preparation for GERDA. The diodes were reprocessed, mounted in their final low-mass holders, and the detectors parameters were measured in the LAr test facility of GDL.

Chapter 2

GERDA Phase-I detector assembly design

In GERDA Phase-I, enriched germanium detectors, which were previously operated by the Heidelberg-Moscow and IGEX collaborations, will be redeployed. In addition, natural germanium detectors operated in the GENIUS-TF experiment will be used. In preparation for GERDA, the Phase-I detectors were reprocessed in order that all detectors use the same technology and to assure the good working condition of the enriched detectors after the dismounting from their cryostats. A low-mass holder has been designed and tested with a prototype detector which uses the same technology as the Phase-I detectors. This chapter first gives an introduction to germanium detectors. Then, it presents the design for the detectors and the low-mass holder with the electrical contacts for GERDA Phase-I. The study of the detector assembly regarding the mounting procedure, the mechanical stability and the electrical contact quality is reported. Finally, the first test of the spectroscopic performance at the detector manufacturer facility is summarized.

2.1 Introduction to high purity germanium detectors

The energy lost by ionizing radiation in semiconductor detectors ultimately results in the creation of electron-hole pairs: a number of electrons is transferred from the valence band to the conduction band, and an equal number of holes is created in the valence band. Under the influence of an electric field, electrons and holes travel to the detector electrodes, where they induce a displacement current that can be measured in an outer circuit. As the number of electron-hole pairs produced is proportional to the absorbed energy, measuring the charge created by the electrons and holes allows the energy of the incident radiation to be measured.

2.1.1 Properties of germanium

Germanium is the predominant material for high-resolution gamma-ray detectors due to its high absorption coefficient, its suitable semiconductor properties and its availability in high purity. Table 2.1 gives the properties of natural germanium.

Atomic number	Density (g/cm ³)	Band gap (eV)	Pair creation energy (eV)	Dielectric constant	Mobility (cm ² V ⁻¹ s ⁻¹)	
					Electrons	Holes
32	5.32	0.67	2.96	16· ϵ_0	3.6·10 ⁴	4.2·10 ⁴

Table 2.1: Properties of natural germanium [36]. The band gap, the electron-hole pair creation energy and the mobilities are given at 77 K.

Several fundamental physical properties are relevant for γ -spectrometry based on germanium semiconductor detectors. They are summarized below.

- The absorption coefficients for all the significant γ -radiation interaction processes (photoelectric absorption, Compton scattering and pair production) increase with atomic number, making germanium advantageous compared to silicon.
- The energy difference between the conduction band and the valence band (the band gap) in germanium is relatively small (0.67 eV), on the order of the energies achievable by thermal excitation. Therefore, germanium detectors must be cooled down to below 120 K, otherwise thermal induced noise would destroy the energy resolution of the detector. Liquid nitrogen (LN₂), which has a temperature of 77 K, is the common cooling medium for germanium detectors.
- The low value of the average energy ϵ necessary to create an electron-hole pair in germanium results in a small statistical variation of the pulse height compared to other γ -ray spectrometry detectors, and leads to superior spectroscopic performance.
- Compared to other semiconductors, the mobility of the charge carriers is relatively high in germanium so the charge collection is fast which facilitates complete charge collection even in large volume detectors. In addition to reduce the thermal generated noise, operating germanium detector at LN₂ temperature also increases the mobility of the charge carriers.
- Increasing the size of the detector increases the detection efficiency. High purity material is necessary for large-volume detectors. Because of the great improvements

in the crystal pulling technique, extremely pure germanium crystal can be grown with a minimum of crystal defects. Today, the concentration of electrically active impurities in germanium can be reduced down to 10^9 cm^{-3} [37].

2.1.2 Semiconductor detector principle

Impurity atoms introduce extra energy states and have a significant effect upon the conductivity. If the impurity atom has one fewer electron in its valence band, then at the impurity lattice site there will be one electron too few (i.e. a hole) in the covalent bond. Such impurities are referred to as acceptor impurities and a semiconductor material with this type of impurity is called p-type. On the other hand, impurities with an extra electron of that required for electronic uniformity of the lattice bond are donor atom and the material with such impurities is n-type. Typically, semiconductors contain both types of impurity and the net character of the material depends upon the type of impurity in excess.

When different semiconductor types are placed in contact with each other, electronic redistribution takes place. Because of the concentration gradient, holes move from the p-side to the n-side of the junction and electrons in the opposite direction. At the junction, the border region where the two semiconductor types meet, the excess of holes and electrons recombine together. The migration of the charge carriers results in a region where no free charge exists, the so called depletion region which is the sensitive volume of the detector. It gives rise to a space charge in the depletion region which suppresses further charge carrier diffusion. A net potential difference builds up across the p-n junction, called contact voltage.

If the p-n junction is forward biased (p-type material connected to positive voltage and n-type to negative voltage) the electrons and holes are pushed towards the junction. It reduces the width of the depletion zone and electric charge flows freely due to the reduced resistance of the p-n junction. On the contrary, if a reverse bias is applied (p-type material connected to negative voltage and n-type to positive voltage) the electrons and holes are pulled away from the junction increasing the width of the depletion region. The junction potential barrier and the resistance increases, and no current flows. In other words, the p-n junction allows electric charges to flow only in one direction.

To measure the ionization-induced charge well above the noise, conventional semiconductor detectors are operated in reverse-biased diode configuration. Applying reverse bias to semiconductor detectors also increases the active volume. The width of the depletion layer, d , can be estimated with the following equation [36]

$$d \approx \sqrt{2 \cdot \epsilon \cdot \mu \cdot \rho \cdot (V_0 + V_b)}, \quad (2.1)$$

where V_0 is the contact voltage (the potential difference across the junction without applying high voltage), V_b the bias voltage, ϵ the dielectric constant, μ the mobility and ρ the resistivity. The latter depends on the impurity concentration in the material N :

$$\rho = \frac{1}{\mu \cdot e \cdot N}, \quad (2.2)$$

where e is the charge on the electron. Typically, V_b is very much greater than V_0 giving $d \propto \sqrt{V_b}$. The active size of the detector can be maximized by increasing the bias voltage to extend the depletion region across the whole available detector volume. In practice, the bias is raised above this depletion voltage to improve the charge collection process. To reach the full depletion depth at low voltages, it is advantageous to utilize material with a concentration of impurities as low as possible. As the size of the detector increases the impurity concentration must be reduced otherwise the necessary bias voltage would be too high (>5 kV), inducing surface currents and high voltage (HV) breakdowns. The great improvement in the size of germanium detectors over the recent years is a consequence of the increased availability of extremely high purity germanium. Germanium can have a depleted, sensitive thickness of 10 cm using $\epsilon = 16 \cdot \epsilon_0$, $\epsilon_0 = 8.854 \cdot 10^{12} \text{ J}^{-1}\text{C}^{-2}\text{m}^{-1}$, $V_b = 5000 \text{ V}$ and $N = 10^9 \text{ cm}^{-3}$ in Eq.2.1 and 2.2.

2.1.3 Germanium detector technology

High purity germanium (HPGe) detectors are constructed by converting one face of a suitably HPGe block into the opposite semiconductor type by evaporation and diffusion or by ion implantation. At very high dopant concentration and high conductivity, the semiconductor is designated as p+ or n+. Such materials are produced to assure the electrical contacts. In a p-type detector, the n+ contact is typically rectifying, initiating the depletion by applying positive voltage. The hole-collecting p+ contact is a blocking contact for the minority carrier. The n+ contact is formed by diffusing lithium onto the appropriate parts of the detector surface and the p+ contact is created by ion-implantation of boron atoms onto the surface.

Germanium detectors are available in a number of different configurations. Their efficiency versus energy curves differ depending upon their size and type. The most standard configuration is the p-type closed-end coaxial detector (Figure 2.1). A close-end coaxial detector has a hole machined into one end to provide a location for the central contact. The p-n junction is always near the outer surface (to obtain the highest electrical fields outside where most of the detection volume is located) and the depleted region grows inwards. Consequently, a p-type detector has a p+ central contact and a n-type detector has a n+ central contact. The thickness of the n+ and p+ contacts represents a dead layer around

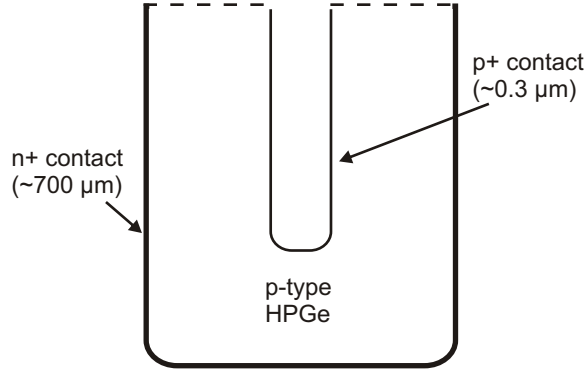


Figure 2.1: Configuration of a p-type HPGe close-end coaxial detector. It has a thin p+ central contact and a thick n+ outer contact. The dashed line refers to the non-contact surface. Typically, positive high voltage is applied on the n+ conductive lithium layer and the signal is read from the boron-implanted p+ contact.

the surface of the crystal within which energy depositions do not result in detector signals. A typical lithium n+ contact produces a dead layer of impure germanium about 500-1000 μm thick because of the high mobility of interstitial lithium donors in germanium. In contrast the dead layer caused by the ion-implanted p+ contact is only 0.3 μm thick. One challenge in the fabrication of germanium detectors is the passivation of the non-contact surface areas which should resist high voltages with low reverse current.

The construction of a junction detector is effectively a p+ and n+ conductor separated by an insulating layer, which is similar to a capacitor. The capacitance depends on the shape and the size of the detector and has an effect on the resolution. Comparing a true coaxial detector to a cylindrical capacitor gives

$$C = \frac{2 \cdot \pi \cdot \epsilon \cdot h}{\ln(r_2/r_1)}, \quad (2.3)$$

where h is the height of the detector, and r_2 and r_1 the detector and core radii respectively. The detector capacitance reduces as the ratio r_2/r_1 increases. Therefore, the central contact hole should be kept as small as possible. A closed-end coaxial detector has a capacitance slightly different than that. Nevertheless, the capacitance calculated for a detector which is 80 mm long, with a detector and a core diameter of 80 mm and 12 mm, respectively, gives a good estimate (38 pF).

In order to obtain the full depletion over the whole detector volume, a reverse bias voltage of typically thousands of Volts must be applied to the detector. Even in the absence of ionizing radiation, all detectors show some finite conductivity and therefore a steady-state

leakage current (LC) is observed. The origins of the LC are related to both the bulk volume and the surface of the detector. Minority carriers attracted across the junction are one source of bulk LC. However, this current is small and its contribution to the total LC is normally negligible. Another source of bulk LC is the thermal generation of electron-hole pairs within the depletion region, which is suppressed by operating the detector at LN_2 temperature. Leakage current across the surface of the detector often become more significant than bulk LC. Surface LC takes place at the edges of the junction where relatively large voltage gradients must be supported over small distances. The surface LC depends on many factors (e.g. surface contamination, humidity). Fluctuation in the LC represents a source of noise, and to avoid significant resolution degradation the LC must not exceed $\sim 1 \text{ nA}$.

Throughout this thesis, the term *crystal* will refer to the pure material in its final shape, the term *diode* to the germanium crystal with the p+ and n+ contact, and the term *detector* to the diode mounted and connected to the electrical read-out system.

2.2 GERDA Phase-I detector design

The standard p-type HPGe detector technology from Canberra Semiconductor NV, Olen [38], was chosen for Phase-I (Figure 2.2). The diodes have a 'wrap around' n+ conductive lithium layer which is separated from the p+ contact by a groove. The p-type HPGe

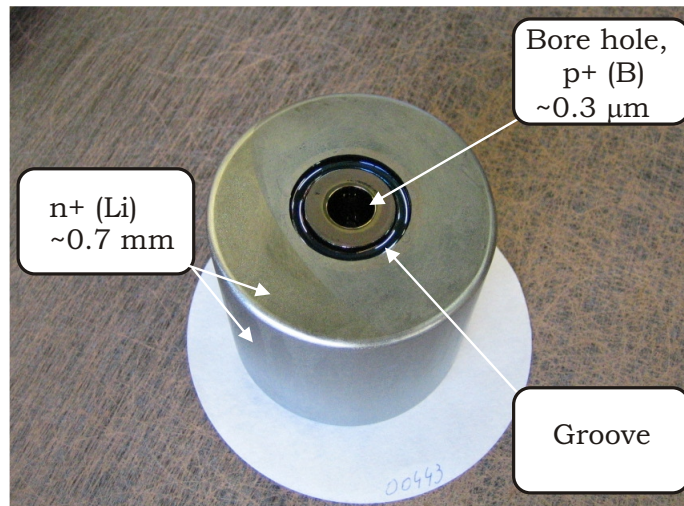


Figure 2.2: P-type HPGe diode from Canberra Semiconductor NV, Olen [38]. The conductive lithium layer (n+ contact) is separated from the boron implanted hole (p+ contact) by a groove.

diodes used in the Heidelberg-Moscow (HdM) and IGEX experiments were accordingly reprocessed for GERDA Phase-I. A typical reprocessing included:

- the machining of a groove,
- the diffusion of a new lithium layer,
- and the implantation of a new boron inner contact.

Prior to the reprocessing of the Phase-I diodes, three prototype diodes were reprocessed with different groove passivation procedures (Fig.2.3).

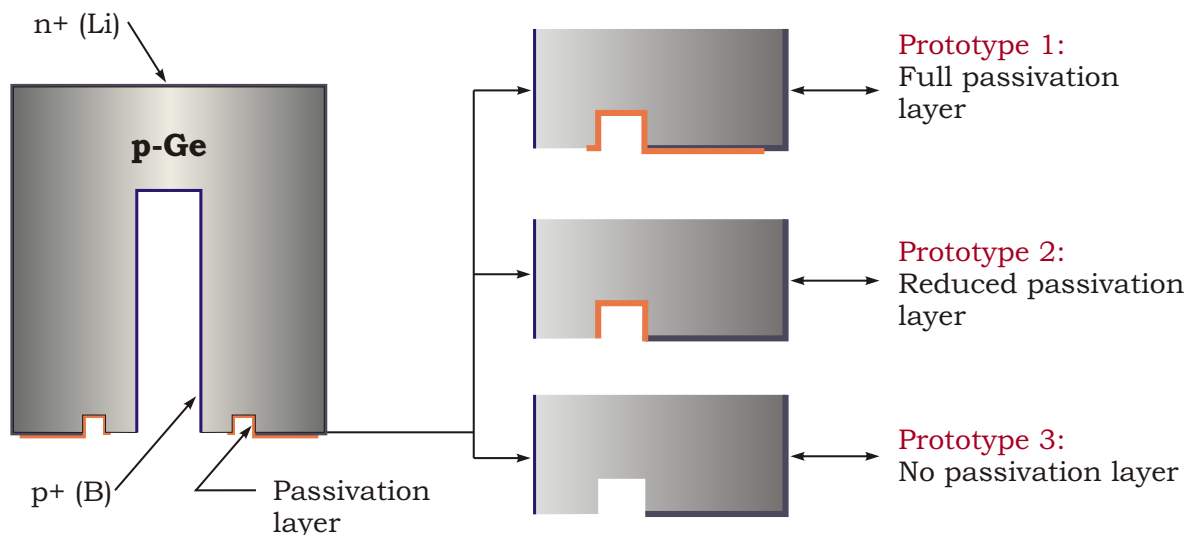


Figure 2.3: Groove passivation procedure for the three prototype diodes (drawings not on scale).

Table 2.2 gives the total mass and the dimensions of the three prototype diodes. The first prototype had a full passivation layer covering the groove and extending to the inner and outer surfaces on the bore-hole side (the side of the diode where the bore hole enters). The second and the third prototypes, originally from PerkinElmer instruments [39] which distributes ORTEC products, were operated previously in the Genius-TF experiment. Prototype 2 had a passivation layer limited to the groove and Prototype 3 had no passivation layer.

Detector	Serial number	Mass (kg)	Diameter (mm)	Height (mm)	Bore hole diam. (mm)	Bore hole depth (mm)
Prototype 1	00443	1560	75	69	12	60
Prototype 2	00461	2467	85	82.5	11.5	42.5
Prototype 3	00469	2465	84	84	12	46

Table 2.2: Total mass, Canberra serial number and dimensions of the three prototype diodes.

2.3 Design of Phase-I low-mass holder and contacts

The design of the Phase-I detector holder takes into account several aspects. First, in order to obtain the background level aimed at by GERDA, the amount of material in the detector support structure has to be minimized, and only selected high radiopurity materials can be used. The envisaged background index in Phase-I is 10^{-2} cts/(keV·kg·y), thus the background index contribution from the detector holder and contacts should not exceed $\sim 10^{-3}$ cts/(keV·kg·y). Second, the quality of the HV and the signal contact is of prime importance for the spectroscopic performance of the detector assembly. Third, the detector support and contacts must be mechanically stable with respect to temperature transients. The thermal contraction of the different materials must be considered. Finally, the detector mounting procedure has to be simple to minimize the manipulations with the germanium diodes.

The GERDA Phase-I detector holder was designed at the Max-Planck-Institut für Kernphysik, Heidelberg. Figure 2.4 illustrates the construction details of the detector support and contacts. It is made of selected high radiopurity materials: copper (~ 80 g), PTFE (~ 10 g) and silicon (~ 1 g). The results of the γ -ray spectroscopy measurements for these materials are given in Table 2.3. These values combined with Monte Carlo simulations [21] give an upper limit on the background index contribution from the detector support of $\leq 10^{-3}$ cts/(keV·kg·y) [40].

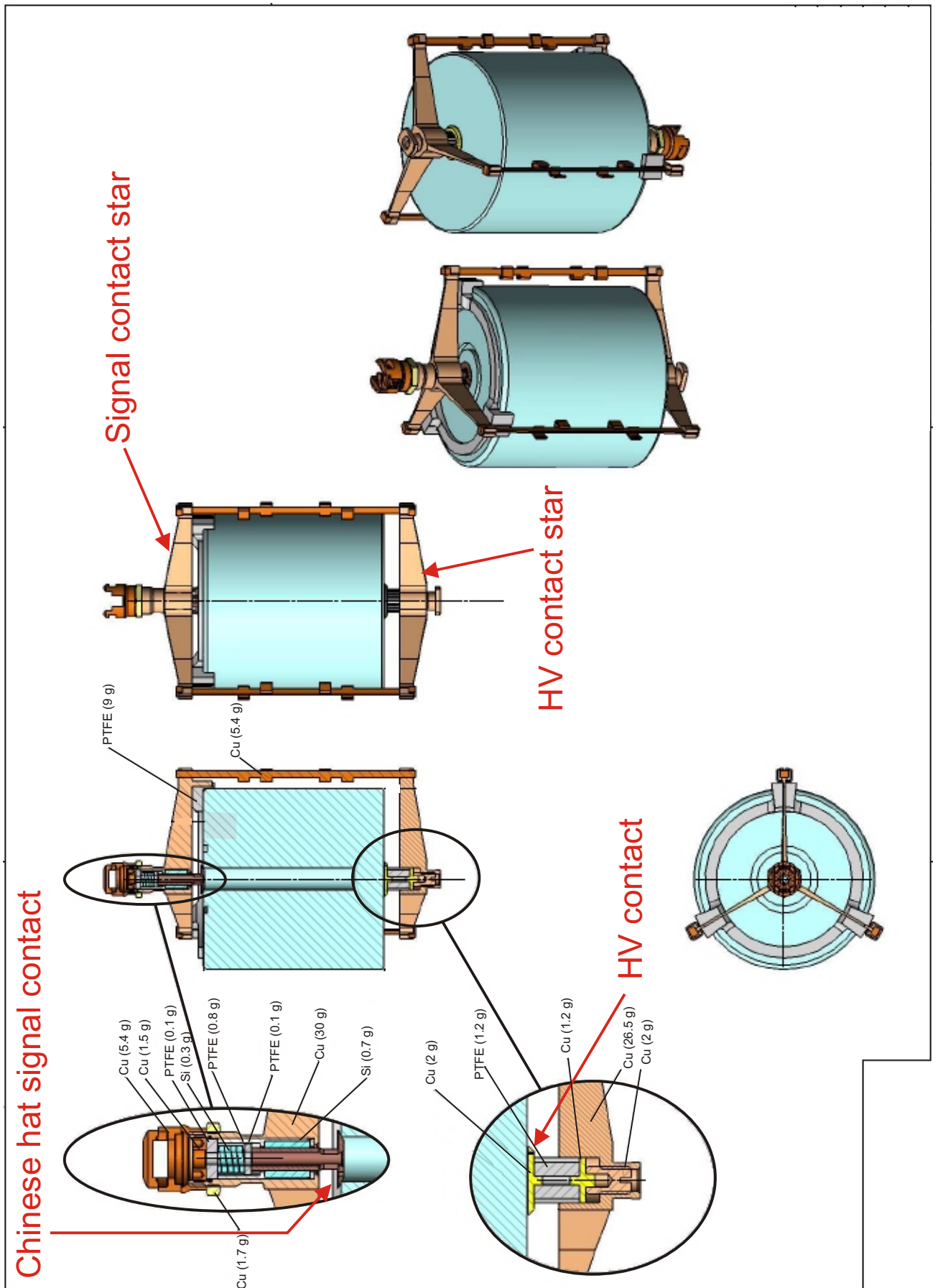


Figure 2.4: Details of a GERDA Phase-I detector holder and contacts.

Material	^{226}Ra ($\mu\text{Bq/kg}$)	^{228}Th ($\mu\text{Bq/kg}$)	^{60}Co ($\mu\text{Bq/kg}$)
Copper	≤ 16	≤ 12	≤ 10
PTFE	25 ± 9	31 ± 14	n.a.
Si	< 12	< 5	n.a.

Table 2.3: Results of screening measurements for the Phase-I detector holder materials. The specific activity is reported for the elements that contain isotopes in their decay chains which produce background at the $Q_{\beta\beta}$ value. The copper is electrolytic of NOSV quality from Norddeutsche Affinerie AG and the PTFE is Dyneon TF 1620 from ElringKlinger Kunststofftechnik GmbH. Both copper and PTFE activities were measured with γ -ray spectrometry [41, 42]. For silicon, the specific activities given were calculated from the concentrations of the primordial mother isotopes assuming secular equilibrium in the decay chains [43]. No cosmogenic production of ^{60}Co occurs for PTFE and silicon.

The diode is mounted in between two *stars*: the signal contact star and the HV contact star. The signal contact is of the so called *chinese hat* design. The presence of a groove allows an external signal contact at the edge of the boron implanted hole (in opposition to ORTEC type diodes, in which there is no groove and the contact is made inside the hole). A silicon spring housed in the signal star applies a force on the chinese hat. The HV contact is located in the middle of the diode surface opposite to the bore hole side. To avoid cryogenic liquid trapping in the inner hole of the diode when it is removed from the dewar, and to avoid mounting manipulations above the inner hole, the diode is mounted with the bore hole side at the bottom and the HV contact side at the top of the detector assembly.

2.4 Studies of the detector assembly performance

A Phase-I detector holder with the electrical contacts as well as a mock-up were constructed according to the dimensions of the first prototype detector. The detector assembly was tested at the detector manufacturer site with the first prototype in 2006. A series of measurements with the detector assembly was carried out, both at room temperature and at liquid nitrogen (LN_2) temperature (submerging the assembly in LN_2) to test the performance of the system. The mounting procedure, the mechanical stability, the signal and the central HV contact quality and the spectroscopic performance have been studied. The operations, measurements and results of the detector assembly testing are summarized below.

2.4.1 Mounting procedure

Before using a real detector, the mounting procedure was defined using an aluminum mock-up. Figure 2.5 presents the mounting sequence.

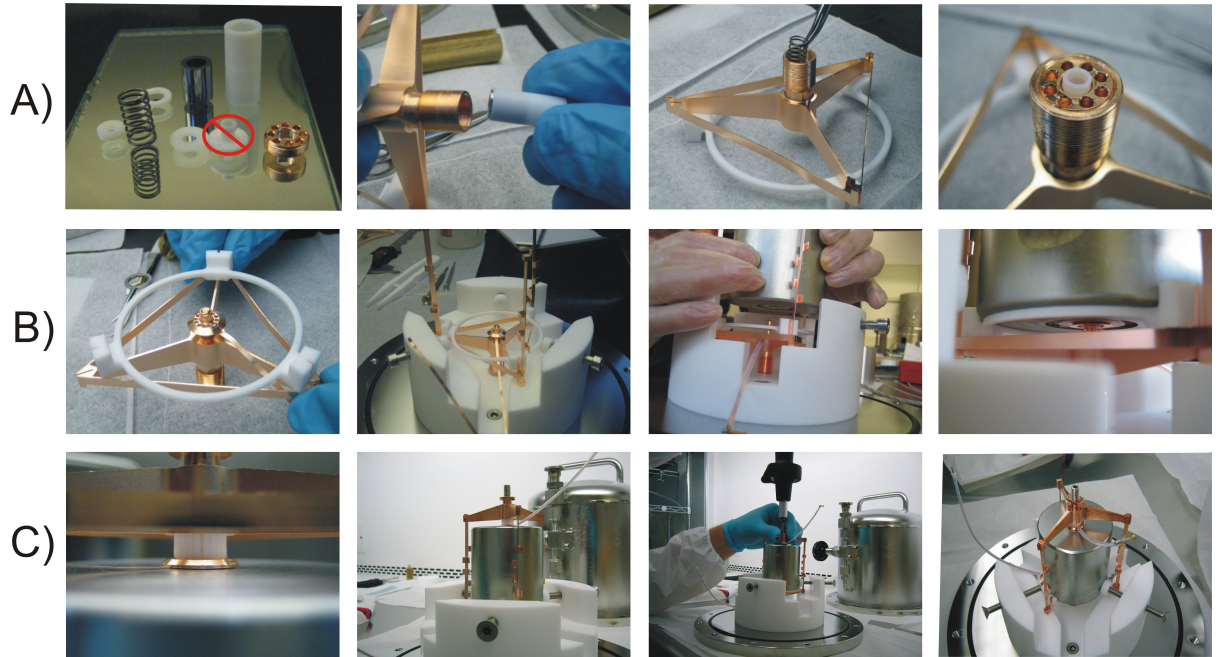


Figure 2.5: Mounting sequence: A) the signal contact star is assembled, B) the chinese hat is inserted in the signal star, the three legs are mounted and the diode is placed on the bottom of the assembly with the chinese hat well aligned with the bore hole, C) the high voltage contact star is assembled, a torque is applied to the screw pressing the high voltage contact on the diode surface and the detector assembly is ready to be submerged in cryogenic liquid.

First, the signal contact star is assembled. It consists of three PTFE rings (a fourth one was designed but its use is not necessary), a silicon tube, a PTFE tube, a spring and a copper part to secure the assembly. The radiopurity of the prototype assembly was not relevant for the detector performance study and, even though the Phase-I detectors are mounted with silicon springs, stainless steel springs were used in part of the tests to simplify the mounting procedure with the prototype detector.

Second, the PTFE ring, on which the detector sits, the three lateral legs and the chinese hat are mounted. Then, the diode is placed on the bottom part of the assembly, with the chinese hat well aligned with the bore hole. This is the most delicate step as the boron implantation is very thin and any scratch can cause severe damage to the detector. Finally, the HV star is assembled and a torque (~ 60 N·cm) is applied to the screw pressing the

copper HV contact on the diode surface. Once again, stainless steel screws were used instead of copper screws to simplify the mounting with the prototype.

Some modifications to the detector support were done to improve the detector assembly. The stars have no longer the lateral bar but thicker radial parts (last picture of Fig.2.5). The mounting process inside a glove box takes approximately 15 minutes.

2.4.2 Test of mechanical stability

For the design of the low-mass holder, the thermal properties of the different materials were considered (Table 2.4). Cooling the detector assembly from room to LN₂ temperature, copper shrinks more than germanium by a factor ~ 3 . The amount of PTFE, which shrinks more than copper by a factor ~ 6 , was chosen so that the contraction of PTFE and germanium is equivalent to that of copper. The mechanical stability of the support with respect to temperature transients was tested using an aluminum mock-up mounted in a low-mass holder (the contraction of aluminum is similar to that of germanium). The mock-up assembly was cooled down in LN₂ and then warmed up in an isopropanol bath. No deformation of any support part was measured.

Material	Thermal expansion (%)	Length at 293 K (mm)	Length at 80 K (mm)
Copper	-0.30	91.1	90.8
Germanium	-0.09	80.0	79.9
PTFE	-1.93	11.1	10.9

Table 2.4: Thermal expansion ($[L_{80K} - L_{293K}] / L_{293K}$) of copper, germanium and PTFE [44, 45]. The lengths of the different parts of a detector holder at 293 K and at 80 K are given as an example ($L_{copper} - L_{PTFE} = L_{Ge}$ at 293 K and 80 K).

If too much force is applied onto the HV contact screw, the arms of the star can bend downward. A deformation of 1 mm was measured after applying a torque of ~ 70 N·cm, which is tolerable as no deterioration of the contact was measured.

2.4.3 Test of electrical contact quality

The contact quality is systematically monitored before, during and after the cooling of the detector assembly measuring the electrical resistance between the signal and the HV

contact (the contact quality improves when the resistivity decreases). Figure 2.6 illustrates the warm and the cold resistance measurement. The resistivity of germanium diodes

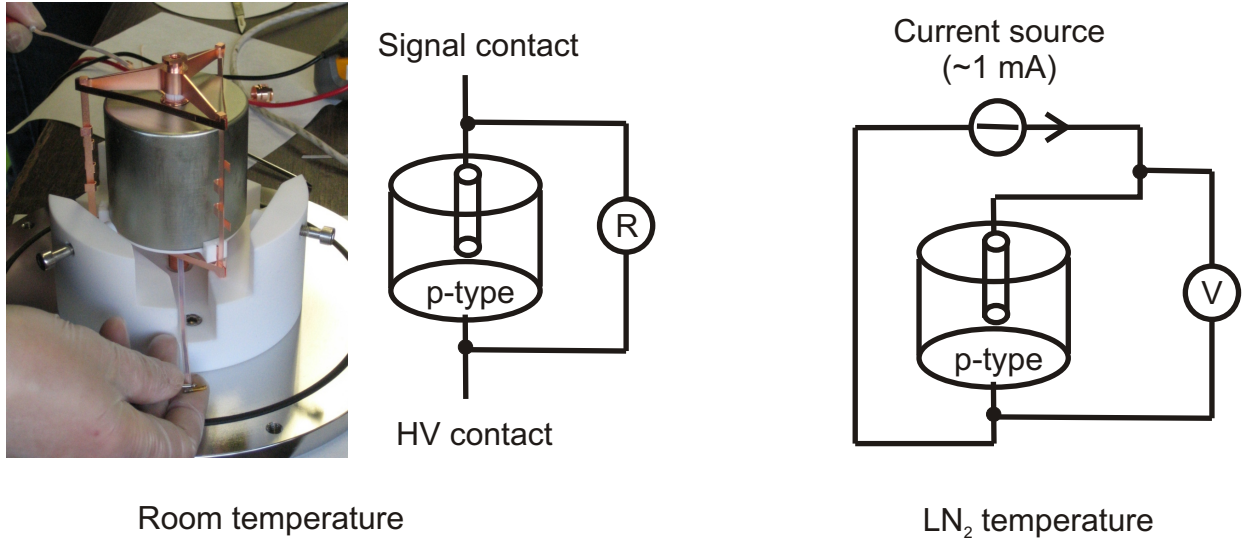


Figure 2.6: **Left:** Warm resistance measurement between the signal and the high voltage contact using a multimeter after the mounting of the diode in its holder. **Right:** Cold resistance measurement sending a current (~ 1 mA) in the forward direction of the diode and measuring the voltage drop.

depends strongly on temperature. At room temperature, the abundance of free charge carriers is dominated by thermally excited electron-hole pairs and the resistivity is not significantly reduced from the intrinsic value of $50 \Omega\cdot\text{cm}$ for germanium [46]. Therefore, the electrical resistance of the warm detector assembly is measurable with a multimeter and typical values are $R_{warm} \approx 30 - 50 \Omega$. On the contrary, the resistivity of the diode at LN_2 temperature is much higher than what can be measured directly with a multimeter. The carrier density in the depletion region reduces to $N \approx 10^2 \text{ cm}^{-3}$ [46]. Inserting this value in Equation 2.2 gives $\rho \approx 10^{12} \Omega\cdot\text{cm}$. Consequently, the electrical resistance of the cold assembly is measured by sending a current of ~ 1 mA in the forward direction of the diode and measuring the voltage drop between the signal and the HV contact. The contact potential is about 1 Volt giving a typical value of $R_{cold} \approx 1 - 2 \text{ k}\Omega$ at LN_2 temperature.

Germanium oxide forms on the diode surface when it is exposed to air which reduces the conductivity of the lithium layer. The outer n+ contact (HV contact) is critical, and therefore it was optimized (Table 2.5). The quality of the HV contact was not improved by adding a gold patch between the copper and the lithium conductive layer. Indium is soft and has an excellent conductivity. It is typically used to improve the contact

Operation	R_{warm} (Ω)
Simple mounting	130
Adding a gold patch	130
Adding an indium patch	30
Adding an indium patch reaching the cylindrical side	30
Polishing the diode surface at the HV contact point	42

Table 2.5: Operations and measurements performed at the detector manufacturer facility to optimize the high voltage contact. The corresponding electrical resistance between the signal and the high voltage contact of the warm assembly is given.

quality but because of its high intrinsic radioactivity, it cannot be used with the Phase-I detectors. As the HV contact is commonly made on the cylindrical side of the detector, it was necessary to verify that a good quality contact can be achieved on the flat detector surface opposite to the bore hole side. Central and lateral contacts were compared attaching indium patches at several regions of the diode surface. Resistance measurements between the signal contact and the indium patches showed no significant difference between the central and the cylindrical side. Moreover, the addition of a long indium patch underneath the central HV contact reaching the cylindrical side did not further improve the contact quality. The surface polishing procedure with abrasive paper is efficient to remove the germanium oxide and to improve the HV contact. Tests showed that a copper to lithium contact is comparable to an indium to lithium contact provided that the diode surface is polished prior to the mounting.

2.4.4 First spectroscopy measurement at the detector manufacturer

Prior to these tests, the first prototype had been operated in a standard vacuum cryostat by the detector manufacturer and an energy resolution of 2.2 keV at the full-width at half maximum (FWHM) at the 1.332 MeV spectral line of ^{60}Co was measured. The spectroscopic performance of the GERDA Phase-I detector assembly was tested in a 50 l dewar filled with LN_2 . A total of eight temperature cycles (cooling the assembly in LN_2 and warming it up in methanol baths, see Chapter 3) were carried out. Each time, modifications to the detector assembly and/or to the electronics were performed to optimize the energy resolution of the naked detector. Figure 2.7 shows the prototype assembly and the dewar in which the detector was operated. A copper sheet was mounted above the diode to shield the detector from the infrared radiation (coming mainly from the dewar lid).



Figure 2.7: **Left:** Infrared shield mounted on top of the prototype assembly. **Right:** Dewar filled with liquid nitrogen in which the detector was operated.

At the first cooling down of the assembly, a high LC (> 1 nA at 3000 V) was observed. This problem was resolved by etching the groove followed by the evaporation of a new passivation layer. Subsequently, low LC (10 pA) was measured up to 5000 V. Then, the HV contact and the performance of the electrical read-out system were improved. Finally, an energy resolution of 2.2 keV (FWHM) for the 1.332 MeV γ -line of ^{60}Co was obtained (Fig.2.8). The detector was connected with a ~ 40 cm long cable to a warm preamplifier mounted on the dewar lid. Afterwards, the diode was warmed-up, stored under vacuum in a transportation container and brought to the Laboratory Nazionali del Gran Sasso where the testing of the prototype assembly resumed.

2.4.5 Conclusion

The p-type HPGe detector technology from Canberra Semiconductor NV, Olen, was chosen for GERDA Phase-I. Three prototype diodes were reprocessed with different groove passivation procedures to test the detector technology. A low-mass holder with the electrical contacts made of ultrapure materials was designed and tested successfully at the manufacturer site with the first prototype detector. The procedure to mount the diodes was defined, and several temperature cycles and mechanical tests were performed. Good quality of the HV contact was achieved by polishing the diode surface prior to the mounting of the contact. The energy resolution of the first prototype detector mounted in the Phase-I low-mass holder was 2.2 keV (FWHM) at the 1.332 MeV spectral line of ^{60}Co , the same as measured in a standard vacuum test cryostat. The detector was connected to the preamplifier with a ~ 40 cm long cable. These tests showed that the GERDA Phase-I detector assembly is very robust and gives excellent spectroscopic performance. The detector holder design thus meets the experimental specifications for the Phase-I of GERDA.

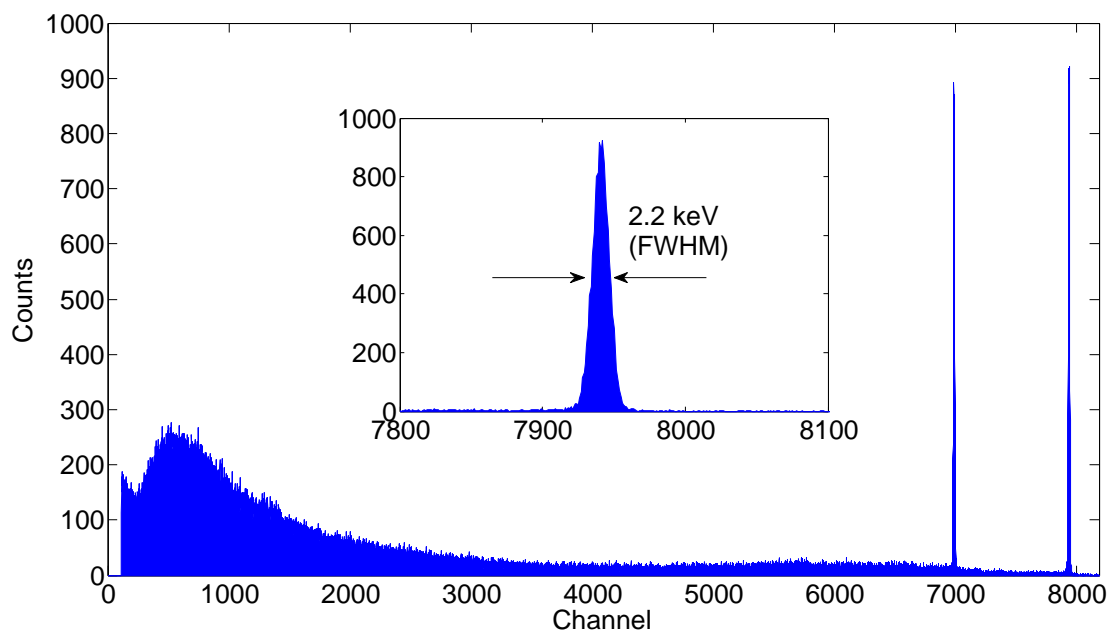


Figure 2.8: An energy resolution of 2.2 keV (FWHM) for the 1.332 MeV γ -line of ^{60}Co was obtained with the first prototype detector mounted in the Phase-I low-mass holder, the same as measured in a standard vacuum test cryostat.

Chapter 3

Study of germanium detectors in the GERDA underground Detector Laboratory

As exposed in the introduction, the high purity germanium diodes have to be stored and tested underground to prevent the cosmogenic activation of the germanium. In addition, the diodes must be handled in a cleanroom where the atmosphere is controlled in terms of dust, humidity and radon, to avoid surface contamination which may result in surface leakage current or in background at $Q_{\beta\beta}$. To satisfy these requirements, the GERDA underground Detector Laboratory (GDL) was constructed at the Laboratori Nazionali del Gran Sasso transforming the former LENS [47] barrack. The laboratory is located in a close neighborhood to the main GERDA site in hall A. The facility offers all the equipment for the handling of the diodes and the operation of bare germanium detectors. GDL was designed to test the Phase-I detectors before their operation in GERDA.

This chapter presents the infrastructures of GDL, the experimental set-up including the design of the liquid argon/liquid nitrogen test benches, the handling protocol, and finally, the leakage current and the spectroscopic performance of bare prototype detectors operated in the GDL test benches.

3.1 Infrastructures of GDL

The GERDA Detector Laboratory is situated at the Laboratori Nazionali del Gran Sasso (LNGS) at the depth of 3800 meters water equivalent. It is a clean room of level 10000 equipped with level 10 clean benches¹. The ^{222}Rn concentration in the air of the LNGS halls is 50 Bq/m³ in average. Fresh air supply to GDL allows to reduce the ^{222}Rn concentration to ~ 10 Bq/m³ [48]. To prevent air from the halls to enter in GDL, it is kept over-

¹The cleanroom level is specified by the number of particles at a specified size per cubic meter.

pressurized. The ^{222}Rn concentration is measured once per day with a 7 l Lucas cell which has a sensitivity of $\sim 2 \text{ Bq/m}^3$. The degree of humidity in the tunnel is rather high ($\sim 60\%$). The humidity of GDL is reduced to $\sim 30\%$ with three dehumidifier units running permanently. The temperature and the humidity of GDL are constantly monitored.

Figure 3.1 shows a view of GDL. The laboratory is equipped with a chemical hood, distilled and deionized water systems, a clean bench, a radon-reduced clean bench and liquid argon/liquid nitrogen (LAr/LN₂) test benches in which the detectors are operated. The radon-reduced clean bench is flushed with evaporated LN₂ stored in a 200 l dewar. The pure N₂ gas flux at the entrance of the bench is of $\sim 2 \text{ m}^3/\text{h}$. After several hours of flushing, the ^{222}Rn concentration measured falls to the level of the Lucas cell intrinsic background.

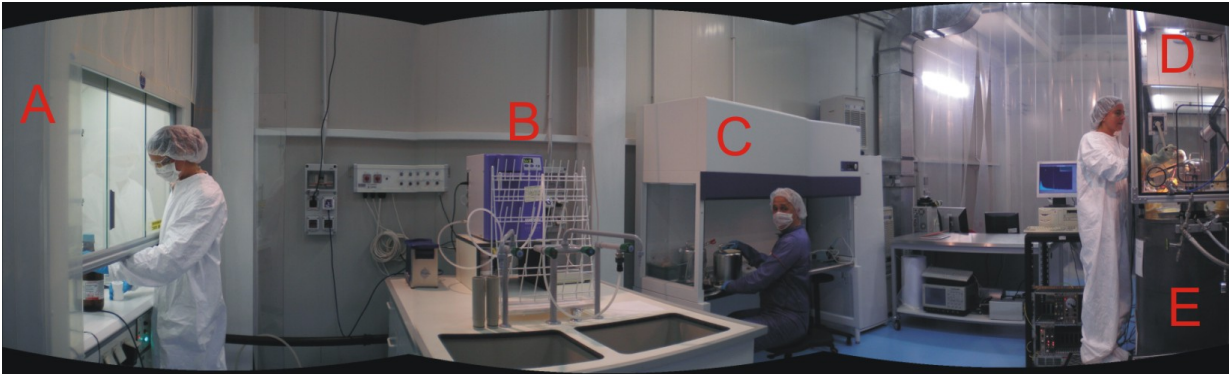


Figure 3.1: View of the GERDA underground Detector Laboratory. It is equipped with: A) a chemical hood, B) distilled and deionized water systems, C) a clean bench, D) a radon-reduced clean bench and E) liquid argon/liquid nitrogen test benches.

3.2 Experimental set-up

3.2.1 Liquid argon/liquid nitrogen test benches

There are two test benches in GDL which were designed to operate bare germanium detectors (Fig.3.2). Each test bench consists of a double-wall electro-polished dewar and an attached glove-box to manipulate the high purity germanium (HPGe) diodes in a closed environment. The 70 l inner vessels are filled with LAr or LN₂. Before filling them with cryogenic liquid, the dewars were flushed with Ar or N₂ gas during at least one day to prevent radon contamination. Test Bench 1 is connected to the radon-reduced clean bench

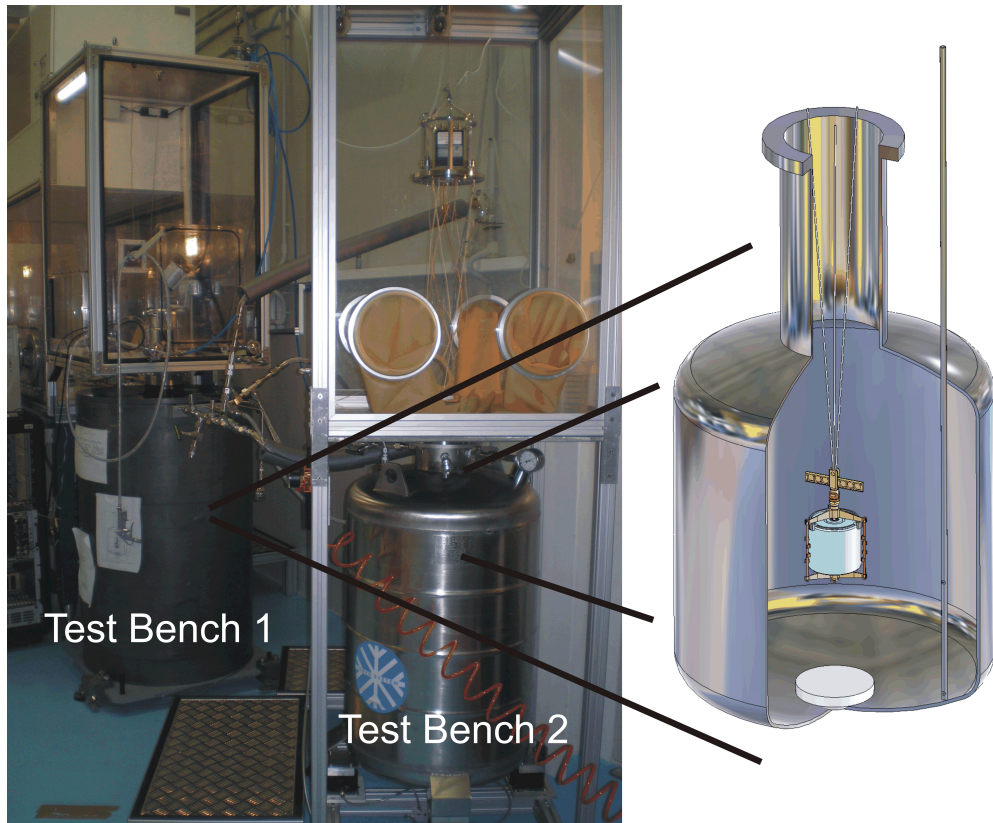


Figure 3.2: The two liquid argon/liquid nitrogen test benches of GDL, each consisting of a double-wall dewar and an attached glove box. Test Bench 1 is connected to the radon-reduced clean bench. A view of the 70 l inner vessel, in which the bare detectors are operated, is also shown.

and has a moderate shield consisting of 2.5 cm of lead surrounding the dewar, which suppresses the external γ -radiation by a factor ~ 10 . Its level of LAr/LN₂ is monitored by weighing cells with an accuracy of 0.2 kg which translates in a height precision of 1 mm for LAr. Test Bench 2 was designed one year after the test with bare detectors in Test Bench 1 started, to be able to operate simultaneously two detectors in GDL. It is mounted on inflatable stands allowing to mechanically decouple the dewar from the glove-box, reducing the vibration transmitted to the detector assembly. Its level of LAr/LN₂ is monitored with temperature sensors. When the detector assembly is ready to be submerged in the cryogenic liquid, it is suspended using Kevlar strings to the dewar flange. A pulley system connected on one side to the dewar flange and on the other side to a handle located outside the glove-box allows to insert (or remove) the detector assembly in the inner vessel.

In the test benches, the bare detectors were sensitive to infrared radiation coming mainly

from the neck as it is less insulated than the rest of the dewar. It increased the detector bulk current. Consequently, metal cylinders were implemented in the inner vessel of both dewars (Fig.3.3). The cylinder (diameter = 128 mm, height = 323 mm, thickness = 2 mm) is fixed at the bottom of the dewar inner vessel and sits on a PTFE disk which isolates it from the dewar. In Test Bench 1, the infrared shield is made of copper and in Test Bench 2, it is made of stainless steel.

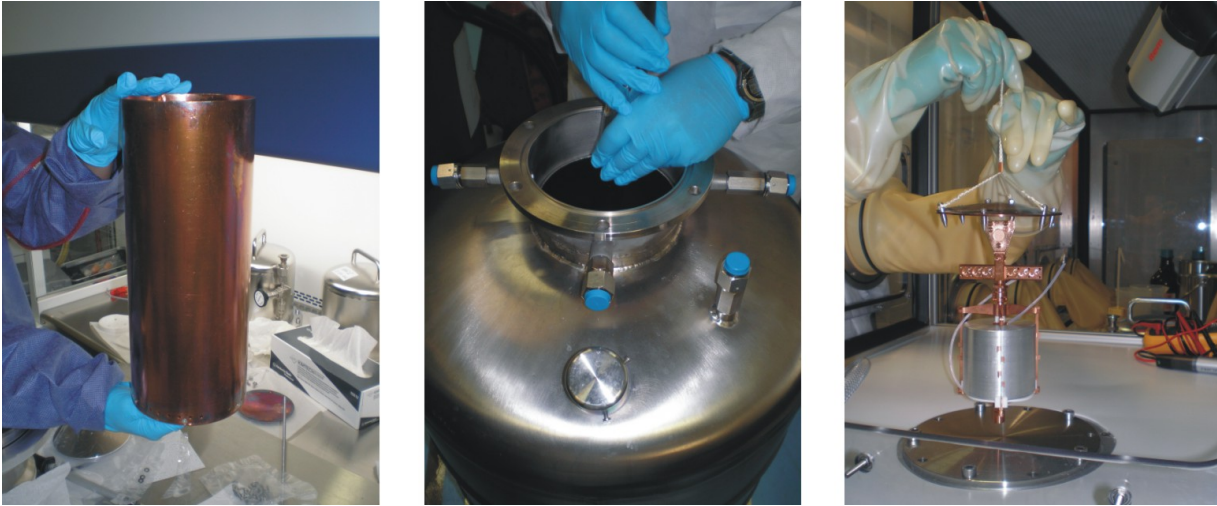


Figure 3.3: **Left, middle:** Installation of a copper cylinder used as infrared shield in Test Bench 1. **Right:** Detector assembly attached to the top of the infrared shield.

Figure 3.4 shows a view and a schematic drawing of the LAr/LN test benches equipped with an infrared shield. Both dewars contain a tube to insert a radioactive source in the proximity of the detector. Two source positions are indicated. At these positions, the distances between the source and the detector assembly are similar but the source in Position 1 irradiates mainly the LAr volume facing the bottom side (bore hole side) and the source in Position 2 irradiates mainly the LAr volume facing the top side (high voltage contact side) of the detector assembly (see Chapter 4). For most of the measurements, a ^{60}Co point source with an activity of 44 kBq (in February 2007) encapsulated in a steel container and mounted on a steel wire was used. Additional measurements were performed with an encapsulated 95 kBq ^{226}Ra source. The breakdown voltage in Ar gas is ~ 5 times lower than in N_2 gas. Therefore, to prevent discharges in Ar gas special care was taken for the high voltage (HV) feed-throughs.

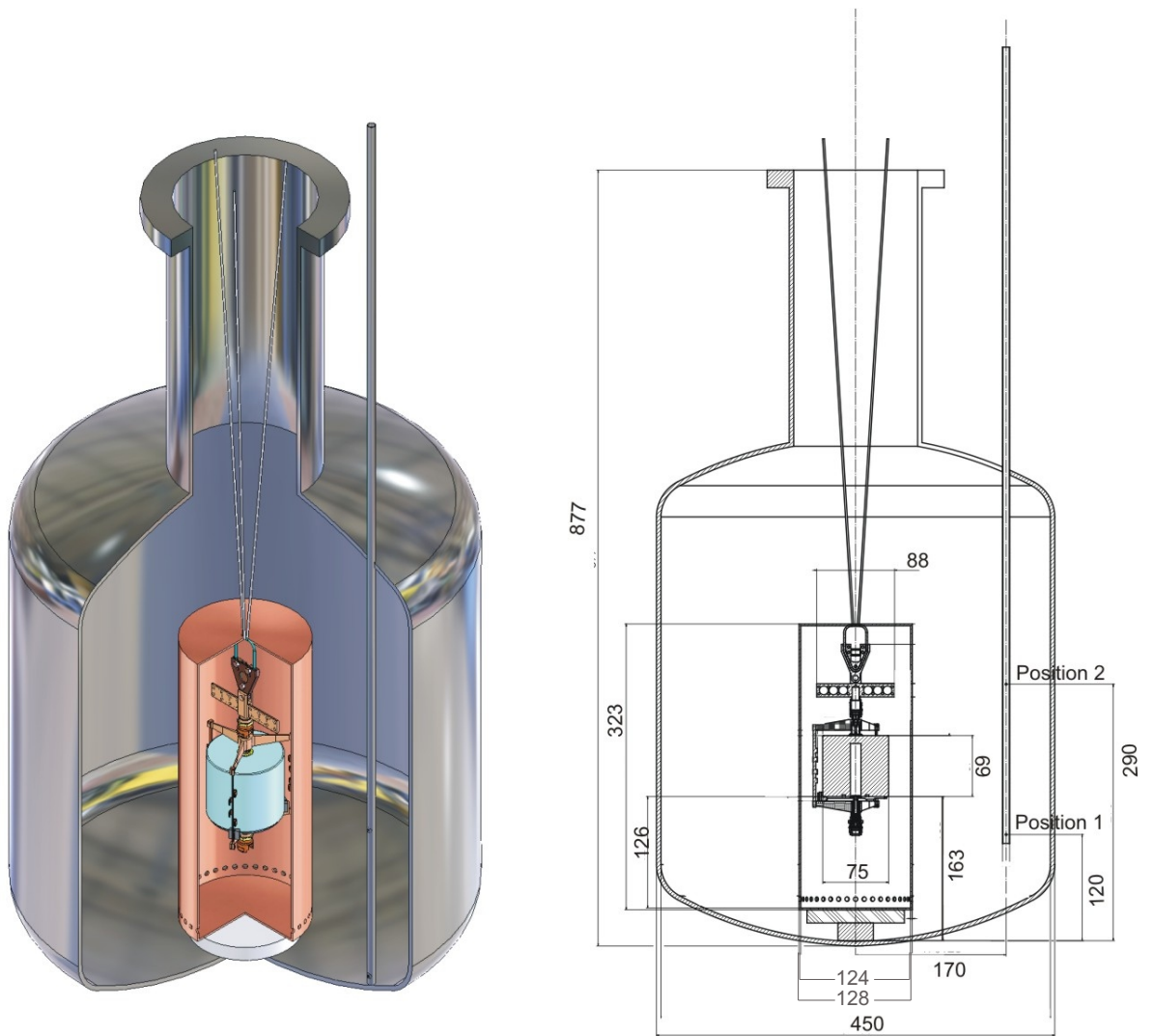


Figure 3.4: View and schematic drawing of the test bench inner vessel equipped with an infrared shield. A tube to insert a radioactive source in the proximity of the detector is shown. Two source positions are indicated (see Chapter 4). The distances between the detector assembly, the infrared shield and the source positions are given in mm.

In these dewars, the evaporation rate of LAr is ~ 4.5 kg/day, which corresponds to a reduction of 2 cm/day. The dewars were refilled on average once per week with 99.999% pure LAr or LN₂ to have always a minimum of 2 cm of cryogenic liquid on top of the infrared shield. The detectors stayed submerged during the refillings. Both test benches are connected to the same refilling system. To prevent any particles coming from the refilling system to reach the test bench dewars, a 0.5 μm filter was installed in the refilling line.

3.2.2 Electronic read-out

The electronic system collects the charge produced in the detector, measures it and stores the information (Fig.3.5).

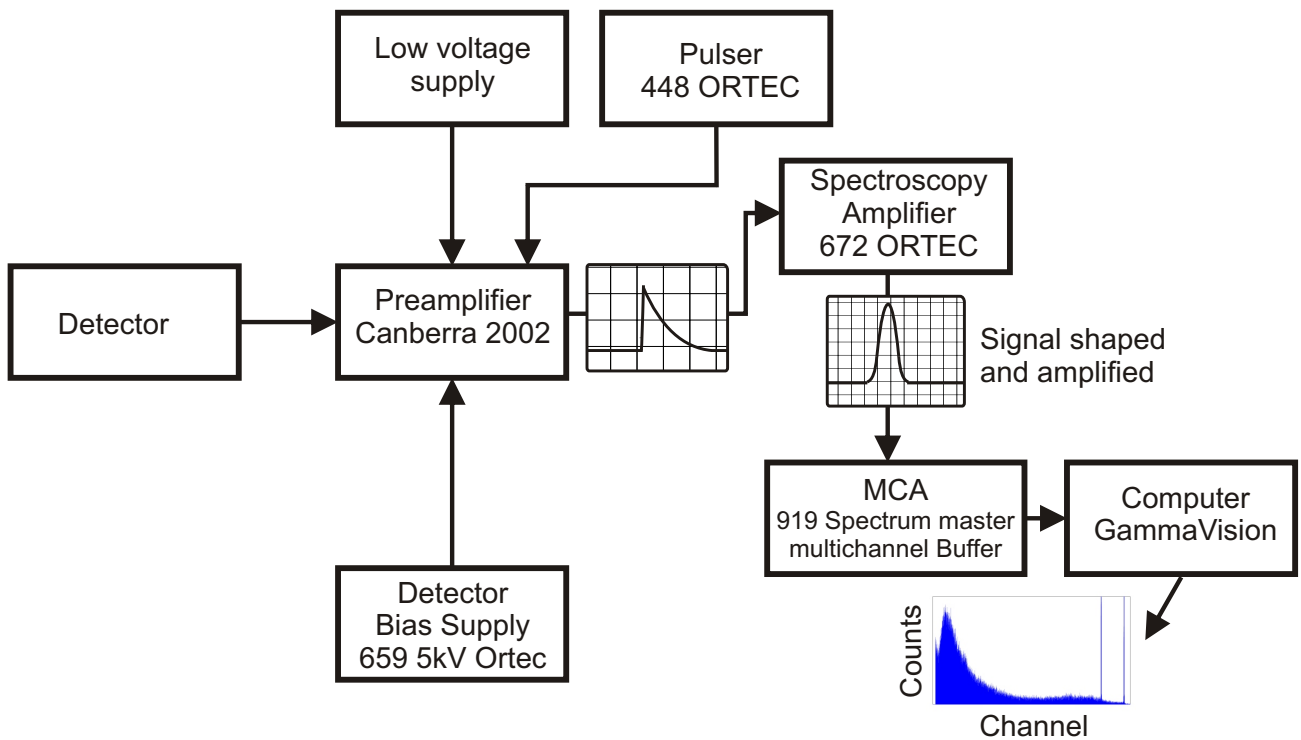


Figure 3.5: Schematic of the electronic system. The bias supply provides the electric field in the detector, the charge sensitive preamplifier converts the charge into a voltage pulse, the spectroscopy amplifier shapes and amplifies the signal, and the Maestro multichannel analyzer (MCA) together with the computer records the spectra.

Standard HV supplies, charge sensitive preamplifiers, spectroscopy amplifiers and Maestro multichannel analyzers were used for the measurements. The spectra were recorded and analyzed with the ORTEC GammaVision software [49].

Figure 3.6 presents a scheme of the detector connection to the first stage of the preamplifier. The first stage includes the field-effect transistor (FET), and the feedback capacitor (C_f) and feedback resistor (R_f). The detector leakage current (LC) was monitored by measuring the test point voltage (TPV) which depends linearly on R_f and the detector LC. In addition, the total current flowing to ground was measured on the HV line with an amperemeter made of a commercial voltmeter reading the voltage drop on a 100 M Ω resistor.

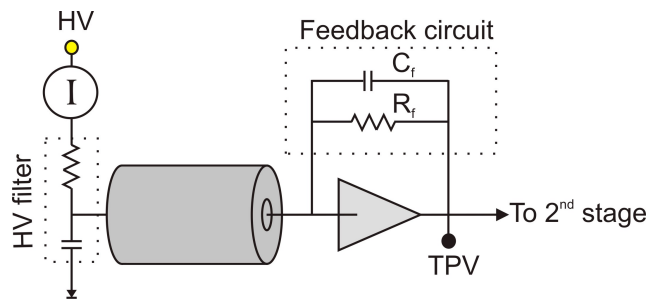


Figure 3.6: Simplified scheme of the detector connection to the first stage of the resistive feedback charge sensitive preamplifier. The total current flowing to ground was measured with an amperemeter on the high voltage side and the detector leakage current was measured with the test point voltage (TPV).

3.3 Handling of germanium diode

High purity germanium diodes must be kept extremely clean both for operational and low background reasons. Even slight traces of surface impurities could give rise to surface LC. The detector surface must be protected from moisture and condensable contaminants. Glove use is mandatory and to avoid any contamination, gloves were changed after touching any other objects when manipulating bare diodes.

3.3.1 Mounting procedure

To prevent cosmogenic activation of the copper, the holder parts must also be stored underground. The exposure above ground of the copper parts was minimized during the

construction and the transportation (the total exposure was approximately 2 days). During the construction, they were stored in the Low-Level Laboratory of the Max-Planck-Institut für Kernphysik, which is located under approximately 15 meters of water equivalent. Prior to their transportation to LNGS, the copper holder parts were electro-polished at Poligrat [50]. An additional cleaning was done in GDL before the mounting according to the following procedure: a first bath with a solution of 1% of H_2SO_4 and 3% of H_2O_2 for five minutes, and a second bath with a solution of 1% of citric acid ($\text{C}_6\text{H}_8\text{O}_7$) for another five minutes. The PTFE and silicon parts were cleaned in a solution of HNO_3 (3%). All parts were rinsed with ultra-pure water in an ultra-sonic bath and then with isopropanol.

The diode mounting procedure is as follow. The signal contact star is assembled in the clean bench. Then, the holder parts and the transportation container housing the diode are inserted in the radon-reduced clean bench. The bench is closed and N_2 flushing started. As the diodes are exposed for short time in the bench (~ 30 min), a minimum of one hour of flushing is performed before mounting the detector assembly inside the radon-reduced clean bench. This way, the HPGe diodes are always manipulated in a closed environment with low concentration of oxygen ($\sim 2\%$), humidity ($\sim 15\%$) and radon (< 2 Bq/m³). When the diode is mounted in its holder, a torque is applied on the HV contact screw and the warm electrical resistance between the signal and the HV contact is measured. Figure 3.7 shows the electrical resistance between the signal and the HV contact of the warm detector assembly in function of the torque applied on the HV contact screw (measured with Prototype 1). Typically, a torque of 60 N·cm is applied. When the HV contact is satisfying, the detector assembly is put back in the transportation container and transferred to the glove-box of the LAr/LN₂ test bench. In Test Bench 1, this step is performed without opening the clean bench.

3.3.2 Procedure to cool down and warm up detector assemblies

Compared to cooling down and warming up HPGe detectors operated in vacuum cryostats, which take days, our procedures are extremely fast (several minutes). For the cooling process, the detector assembly is attached to the cross which is suspended on the dewar flange, the signal and the HV contact is connected, the assembly is lowered down into the inner vessel filled with cryogenic liquid and the dewar flange is tightly closed. It takes ~ 5 minutes for the detector to reach the cryogenic temperature. Then, HV can be applied.

For the warming process (Fig.3.8), 2 polyethylene containers (2 l each) are filled with electronic-grade methanol. The first methanol bath can be at room temperature but the second bath is heated up to 50-60°C (the boiling point of methanol is 64°C). At the detector

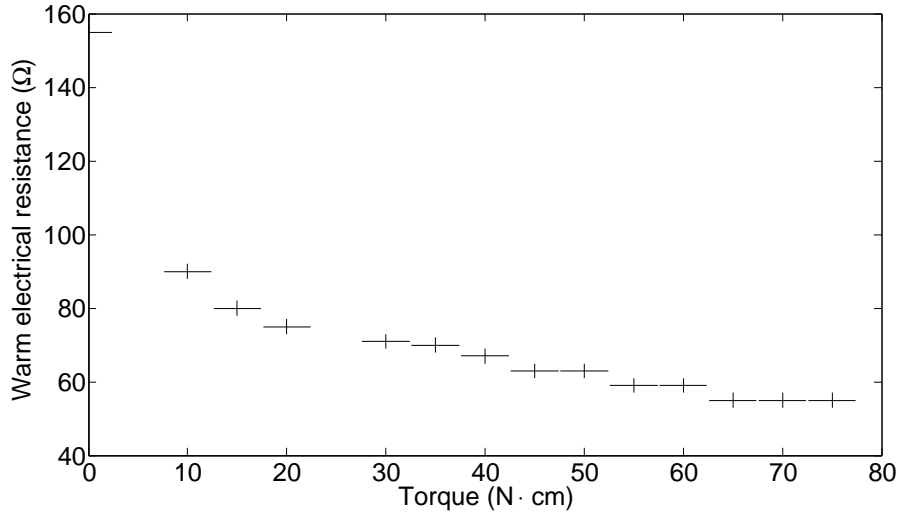


Figure 3.7: Electrical resistance between the signal and the high voltage contact of the warm detector assembly in function of the torque applied on the high voltage contact screw (measured with Prototype 1). Typically, a torque of 60 N·cm is applied.

manufacturer site, bain-marie (i.e. water baths) are used to heat up the methanol. When the detectors are operated in Test Bench 1, the methanol is warmed-up in the closed environment of the radon-reduced bench and the use of a bain-marie would increase the humidity inside the bench. Therefore, the methanol is warmed up inside a thick aluminum bucket which sits on an heating plate. When the methanol is warmed, the detector assembly is taken out from the dewar and inserted in the first bath. The signal and the HV contact is disconnected, the assembly is unattached from the cross and the container is transported to the other section of the radon-reduced bench which is cleaner as it is right below the high-purity filter². When no more convection is observed in the first bath, the diode is transferred to the second bath. To reduce the risk of contamination, the diode should be manipulated (dismounted from its holder and/or placed into a transportation container) when its temperature is slightly higher than the ambient temperature.

Within the first year of testing, 43 cooling-warming cycles have been performed with the first prototype to do mounting and/or electronics modifications. In total, more than 100 temperature cycles were accomplished with the prototypes and the Phase-I detectors. None of the detectors has ever been damaged by this procedure.

²When the detectors are operated in Test Bench 2, the methanol is heated before being transported inside the bench and the described operations are performed in the glove box under N₂ atmosphere. The Phase-I enriched detectors were only operated in Test Bench 1.

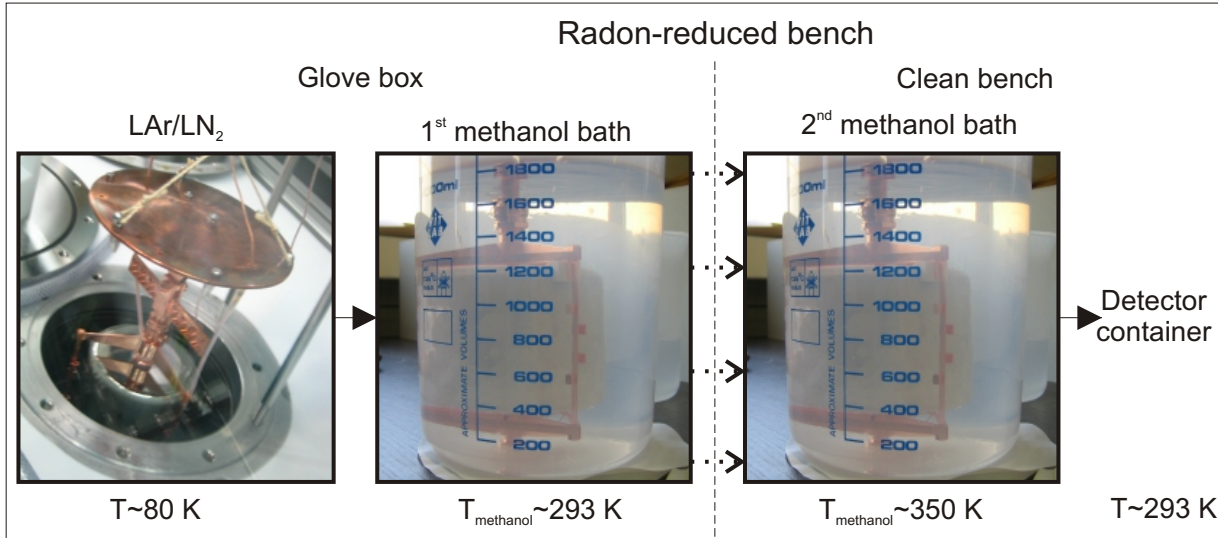


Figure 3.8: Warming up process for the detectors operated in Test Bench 1: the detector is taken out from the dewar and inserted in a first methanol bath where the signal and the high voltage cable is disconnected. Then, the first bath containing the diode is transferred to the cleanest section of the radon-reduced bench and the diode is submerged in the second methanol bath. Finally, the diode is stored in a transportation container. The whole process takes approximately 10 minutes.

3.3.3 Storage of the diodes

The diodes are stored at room temperature under vacuum in an electro-polished stainless steel transportation container (Fig.3.9). Three screws with PTFE protective caps hold the diode in the middle of the support structure. The container is pumped down to 10^{-6} mbar to avoid surface contamination of the diode. If the diodes are stored over a long-period of time, the containers are pumped every month. Typically, the pressure goes from 10^{-6} mbar to 10^{-4} mbar within one month. The measured radon emanation of these containers is $45 \pm 17 \mu\text{Bq}$ in saturation. It has been observed that improper storage can result in an increase of the detector LC. It happened to the first prototype, which had a full passivation layer, after staying several days under normal atmosphere. The diode was healed by a repair of the passivation layer. Since then, the prototype diodes are never exposed to normal air for more than one hour³. They stay under N₂ atmosphere or they are stored under vacuum.

³The enriched diodes were never exposed to the normal air of the laboratory.

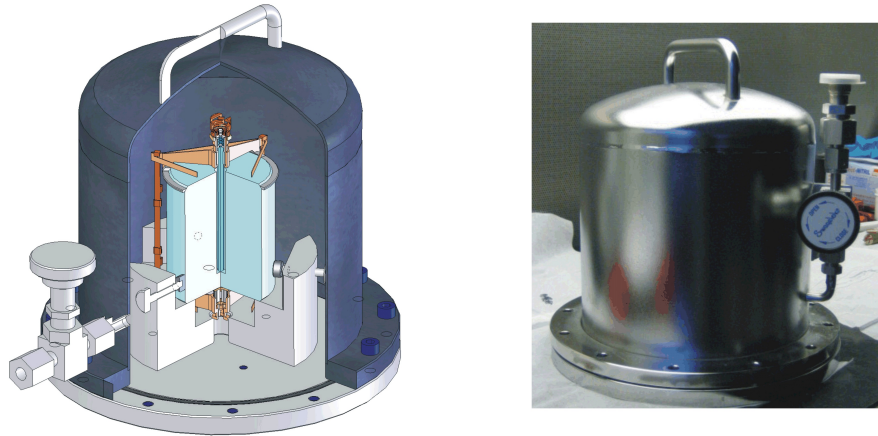


Figure 3.9: A drawing and a picture of a transportation container in which the HPGe diodes are stored under vacuum. The weight of the container is ~ 10 kg and its dimensions are 260 mm (diameter) x 265 mm (height).

3.4 Optimization of the bare detector performance in the test benches

To improve the bare detector performance, the LAr/LN₂ test benches and the electrical read-out system were optimized for low LC measurement and good energy resolution.

3.4.1 Results of leakage current measurements

In GDL test benches, the bare detectors were sensitive to infrared radiation if only a thin copper sheet mounted on top of the detector assembly was used (Fig.2.7). At low HV, the LC was at the level of several hundred pA (Fig.3.10), which is still acceptable in terms of energy resolution but significantly higher than measured at the detector manufacturer (~ 10 pA). After the installation of the infrared shield in the test benches, the current-voltage (I-V) curves measured in GDL were similar to those measured at the detector manufacturer.

3.4.2 Results of spectroscopic measurements

The testing of the Phase-I detector assembly was first performed using a standard pre-amplifier (Canberra 2002) mounted on the top of the dewar flange. To improve the spec-

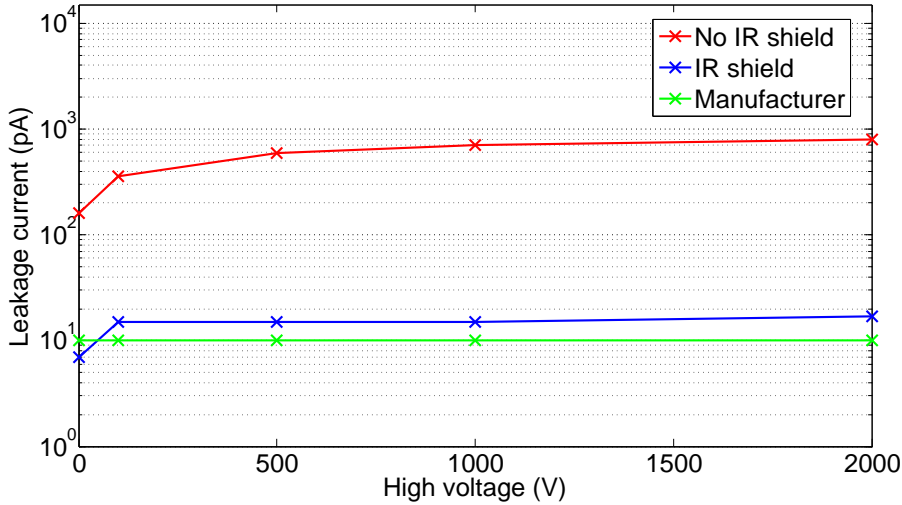


Figure 3.10: Current-voltage curves measured at the detector manufacturer, and in a GDL test bench before and after the installation of the infrared shield. The uncertainty of the leakage current is ~ 10 pA.

trosopic performance of the bare detectors, measurements were done using the first stage preamplifier from one of the Heidelberg-Moscow (HdM) cryostats operated in Ar gas in the dewar neck (the warm second stage was equivalent as in a standard preamplifier). Figure 3.11 presents the functional schematic of the Canberra 2002 preamplifier and a picture of the HdM first stage mounted below the flange. The handling of the detector and, if necessary, the repair of electronic components are easier with warm preamplifiers located outside the dewar. However, operating the preamplifier closer to the detector is advantageous in terms of energy resolution. First, shortening the signal cable, which connects the detector to the first stage preamplifier, reduces the electronic noise. Second, operating the first stage preamplifier at colder temperature reduces the thermal noise in the feedback resistor.

Before operating the detectors with the above described preamplifiers, tests were performed with a capacitor ($C = 27$ pF) mounted between the FET and the HV line (no HV was applied). The resolution of the pulser at 1 MeV was measured. Table 3.1 summarizes the measurements with the capacitor and the spectroscopic measurements with Prototype 1 in different setup configurations.

Without infrared shield implemented, the detector assembly was operated in the middle of the inner vessel and the warm first stage preamplifier was connected to the detector assembly with a 80 cm long cable. An energy resolution of 2.8 keV (FWHM) at the 1.332

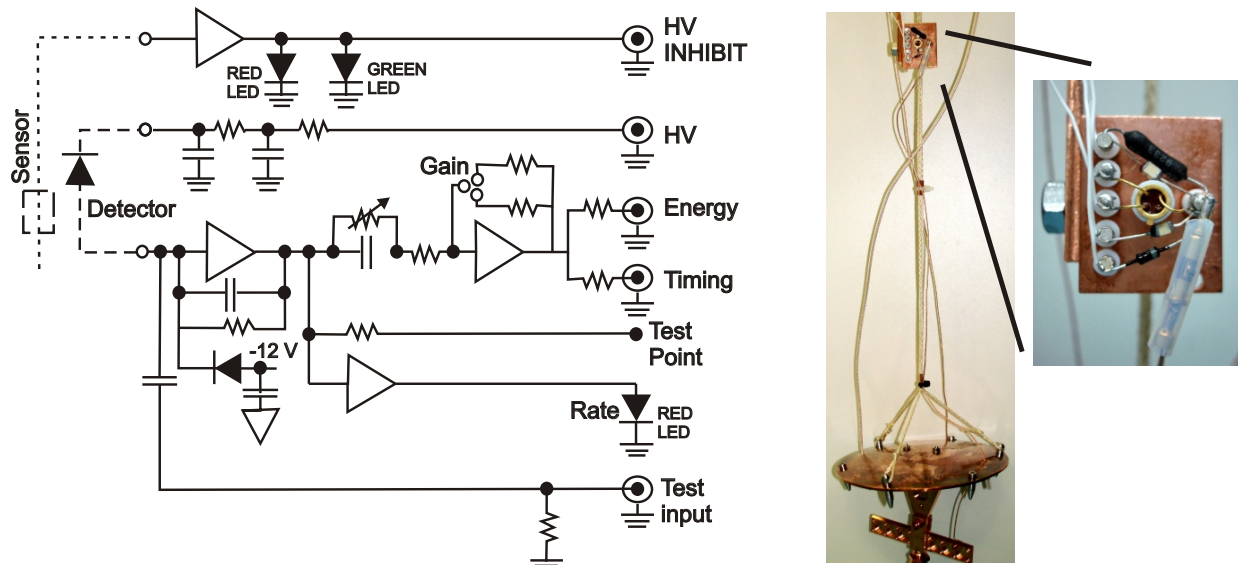


Figure 3.11: **Left:** Schematic of the Canberra 2002 preamplifier. **Right:** Photos of the first stage preamplifier from HdM cryostat mounted on a copper bar and attached to the dewar flange. The first stage includes the field-effect transistor, the feedback resistor and capacitor, the test capacitor and the protective diode.

MeV γ -ray line of ^{60}Co and 2.5 keV (FWHM) for the pulser line at 1.4 MeV was obtained. With the infrared shield, the detector assembly was situated deeper in the dewar so the signal cable went from 80 cm to 100 cm. In this configuration, the best resolution achieved was 3.5 keV (FWHM) for the ^{60}Co peak and 3.0 keV (FWHM) for the pulser peak at 1.4 MeV. The LC of the detector was ~ 10 pA.

The HdM first stage preamplifier was mounted on a copper bar attached to the dewar flange. The FET was located 40 cm below the flange, reducing the signal cable length between the detector and the FET to ~ 60 cm. An energy resolution of 2.6 keV (FWHM) for the ^{60}Co peak at 1.332 MeV and 2.0 keV (FWHM) for the pulser peak at 1.4 MeV was achieved with $10 \mu\text{s}$ shaping time (Fig.3.12). Therefore, using shorter signal cable and colder FET improves the resolution by ~ 1 keV. An additional measurement showed a deterioration of the energy resolution by more than 1 keV with an elongation of ~ 1 m of the signal cable.

During these test measurements, it was observed that the detector assembly is sensitive to microphonic noise. The electronic noise, and so the spectroscopic performance, depended on the level of the cryogenic liquid in the dewar. Noise was induced if the liquid was at the level of the neck of the dewar because of the boiling or if the liquid level fell below 10 cm above the infrared shield.

Preamplifier	Cable length (cm)	Temp. (K)	Shaping time (μ s)	Capacitor FWHM (keV)	Detector FWHM (keV)	
					^{60}Co	Pulser
Canberra 2002						
No IR shield	80	~ 293	6	-	2.8	2.5
IR shield	100	~ 293	6	2.6	3.5	3.0
HdM 1st stage						
On the flange	100	~ 293	6	2.6	-	-
In the neck	60	~ 200	10	1.6	2.6	2.0
Extra cabling	160	~ 200	10	2.9	-	-

Table 3.1: Spectroscopic performance of the first prototype detector operated in Test Bench 1 using the warm preamplifier (Canberra 2002) and the Heidelberg-Moscow (HdM) first stage preamplifier. The signal cable length, the shaping time and the energy resolution (FWHM) for the ^{60}Co peak at 1.332 MeV and for the pulser peak at 1.4 MeV are given. Measurements with a capacitor ($C=27$ pF) at the entrance of the FET simulating the detector were performed and the resolution of the pulser at 1 MeV is given.

The spectrum resolution depends both on the detector assembly and the electronic system. The overall uncertainty in the energy is the combination of the charge production and the charge collection uncertainties, and the electronic noise. The charge production uncertainty is an unavoidable physical limit (on the order of 1 keV). The charge collection uncertainty is in principle reduced to a negligible level by careful detector design. The electronic noises are grouped into categories [36]:

- The parallel noise w_p is associated with the current flowing in the preamplifier circuit, mainly from the detector LC and the thermal noise in R_f :

$$w_p^2 \propto w_{LC}^2 + \left(\frac{2 \cdot k \cdot T}{R_f} \right) \cdot \tau, \quad (3.1)$$

where w_{LC} is the contribution from the detector LC current, T the temperature of the feedback resistor R_f and τ the shaping time. The width of the LC contribution to the noise is calculated as the statistical fluctuation of the number of electron integrated by the spectroscopy amplifier:

$$w_{LC}(FWHM) = \sqrt{\frac{I_{LC} \cdot \tau \cdot f}{e}} \cdot 2.96 \text{ eV} \cdot 2\sqrt{2 \cdot \ln 2}, \quad (3.2)$$

where I_{LC} is the detector LC, τ the shaping time, f a factor depending on the amplifier filter ($f = 1.85$ for CR (high-pass) - RC (low-pass) filter [51]), e the charge on

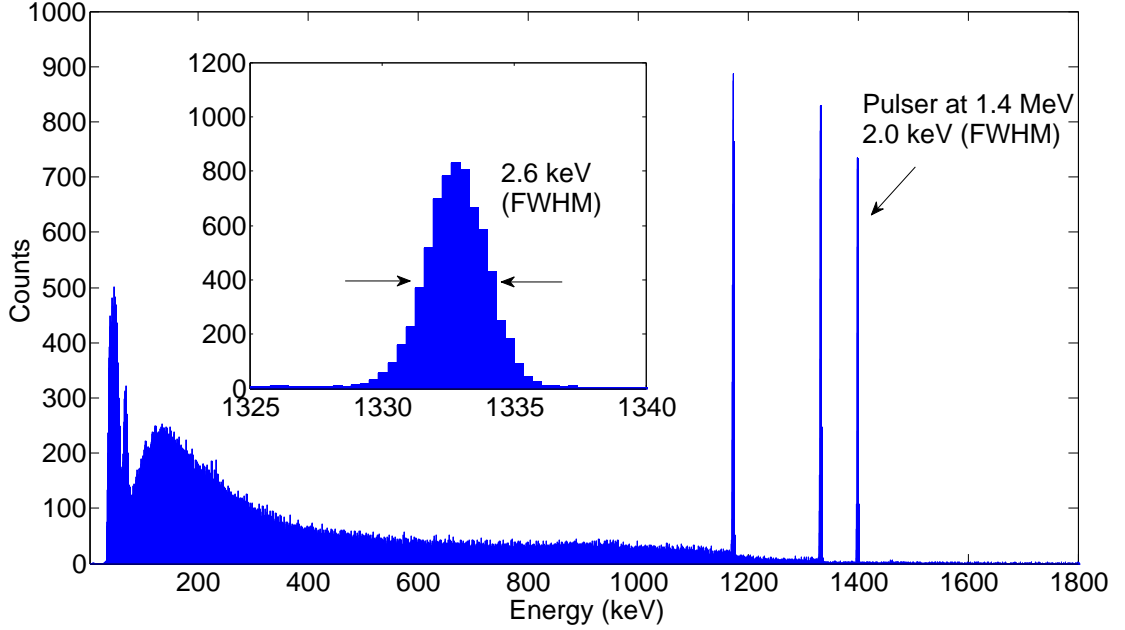


Figure 3.12: Spectrum measured with Prototype 1 exposed to a ^{60}Co source in the GDL test bench. A zoom on the ^{60}Co peak at 1.332 MeV and the resolution of the pulser at 1.4 MeV are shown.

the electron, 2.96 eV the energy needed to create an electron-hole pair in germanium at 80 K and $2 \cdot \sqrt{2 \cdot \ln 2}$ the factor to convert the standard deviation to FWHM. The parallel noise reduces with low LC (including low count rate), low R_f temperature, high value of R_f and small shaping time.

- The series noise w_s is mainly due to noise in the FET:

$$w_s^2 = C^2 \cdot \left(\frac{T}{g \cdot \tau} \right), \quad (3.3)$$

where C is the total capacitance at the preamplifier input and g the gain of the FET. The series noise reduces with smaller capacitance of the detector and the detector-preamplifier connection, cold FET, and long shaping time.

- The Flicker noise (w_f), which is also called $1/f$ noise because its power spectrum varies inversely with the frequency, depends on direct current variations in active devices. It is expressed as

$$w_f^2 = (I - I_m)^2 = k \cdot I^a \cdot \frac{\Delta f}{f}, \quad (3.4)$$

where k is the $1/f$ noise coefficient, I is the current and I_m is the mean current, a is a constant between 0.5 and 2 and f is the frequency. This component of noise is independent of the shaping time and increases with the count rate.

An analysis of the baseline noise was performed to investigate the spectroscopic performance of Prototype 1 operated in Test Bench 1 with the HdM first stage preamplifier. The detector LC was ~ 10 pA. Baseline pulses were collected using a 100 MHz 14 bit FADC and a sampling time of 1 ms. A fast Fourier transform (FFT) analysis was performed using the JSpecView software [52] and the results are shown in Fig.3.13.

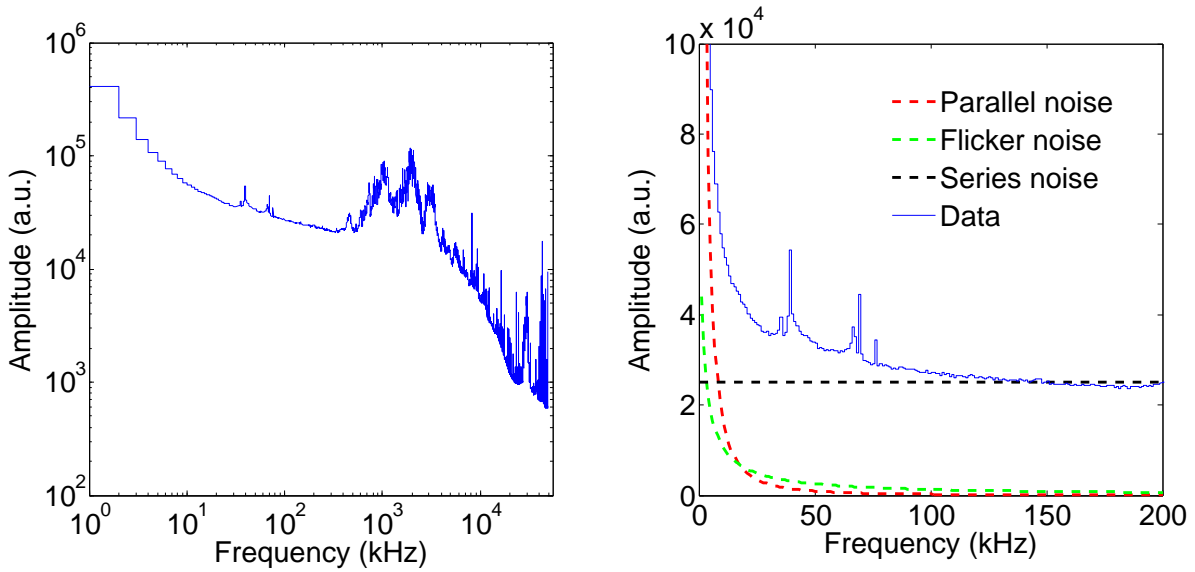


Figure 3.13: Fast Fourier transform analysis of baseline pulses collected with Prototype 1 operated in the GDL test bench. The frequency resolution was 1 kHz. **Left:** full spectrum in log-log scale; **right:** linear zoom showing the three components of the electronic noise.

Considering the usual shaping times for germanium detectors (1-10 μ s), the low frequency components of the noise up to around 500 kHz affect the energy resolution. The contribution from each category of noise is visible in Fig.3.13. The parallel noise appears as $1/f^2$, the series noise as constant and the Flicker noise as $1/f$. The parallel noise dominates the spectra at low frequency. The slope changes due to the contribution from the Flicker noise, and then the series noise becomes predominant. The peaks at low frequencies are produced by microphonic noise.

Figure 3.14 presents the energy resolution of the detector assembly in function of the shaping time. The best energy resolution was achieved at the longest shaping time. This is in agreement with the FFT analysis as the corner frequency, where the fit to the parallel

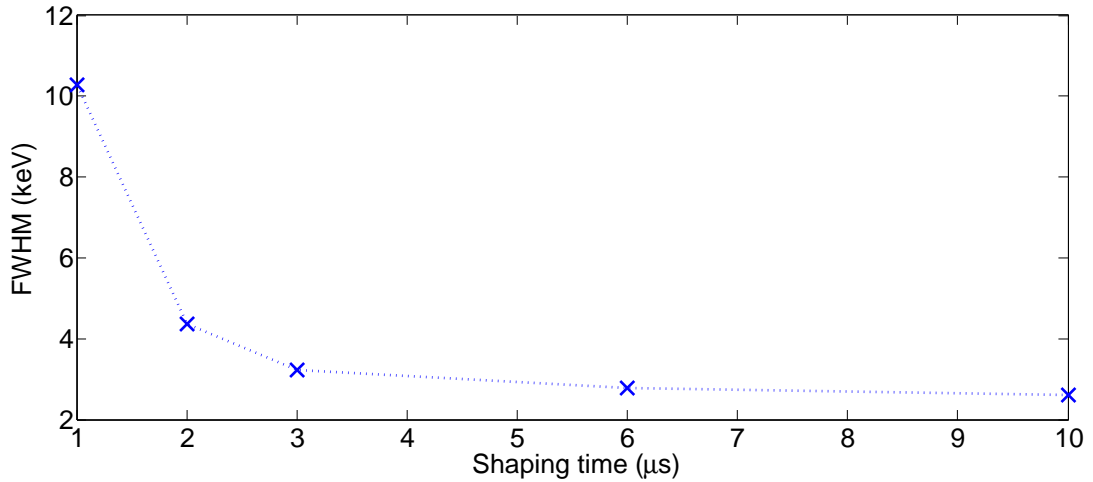


Figure 3.14: Energy resolution in function of the shaping time measured with Prototype 1 and the HdM first stage preamplifier. The measurements were performed with 10000 counts under the 1.332 MeV γ -line of ^{60}Co .

noise crosses with the fit to the series noise, is at low frequency. It suggests that the dominating noise was the series noise.

A lot of high frequency components of the noise can be seen in Fig.3.13. For the energy resolution of the detector, only the low frequency components are relevant. However, to perform pulse shape analysis and to see changes on the leading edge of the signal (which was not to goal of these measurements), one has to be concerned by the disturbances at higher frequencies.

In GERDA, the use of warm preamplifiers is not an option as it would imply the use of several meters long signal cables. The GERDA experiment requires first stage preamplifiers operated at cryogenic temperature. A development version of two of the candidate preamplifiers considered for GERDA Phase-I were tested in GDL test bench with a bare detector. The preamplifiers were attached on the cross of the detector support and submerged in LAr. The signal cable from the detector assembly to the FET was ~ 20 cm. The semi-integrated IPA 4 preamplifier [53] and the fully integrated PZ0 preamplifier [54] were tested. However, despite the short signal cable, the energy resolutions achieved were 3.5 keV and 2.7 keV (FWHM) for the 1.332 MeV ^{60}Co peak and for the pulser peak at 1.4 MeV, respectively. These results were worse than expected from previous measurements with a pulser and simulated detector capacitance giving an energy resolution of 1.5 keV (FWHM) at 1.4 MeV.

3.5 Conclusion

The GERDA underground Detector Laboratory was designed and constructed to handle and operate bare HPGe detectors. The diodes are manipulated in ultraclean environment under nitrogen atmosphere. Within the first year of testing, approximately 50 cooling-warming cycles have been performed with the first prototype to do mounting and/or electronics modifications. The cooling and the warming procedure is very quick and none of our detectors has ever been damaged by these processes. Two LAr/LN₂ test benches are operational in GDL. During the first year, the LAr/LN₂ test bench and the detector assembly were optimized for cleanliness, optimal mounting procedure, low LC measurement and spectroscopic performance. The I-V curves of the detectors measured in the GDL test benches are at the same level as measured at the detector manufacturer. The energy resolution obtained with the first prototype was 2.6 keV (FWHM) at 1.332 MeV, with a signal cable of ~ 60 cm connecting the detector to the first stage preamplifier. Even though the energy resolution was limited by the electronic noise, such resolution is acceptable for GERDA.

Chapter 4

Investigation of the leakage current response of bare detectors in liquid argon and liquid nitrogen to γ -radiation

During the test with the first bare prototype detector operated in liquid argon, we observed that the leakage current increased continuously when the detector was biased with high voltage and exposed to γ -radiation. Since germanium detectors were not operated bare in liquid argon before, γ -radiation induced leakage current was not predicted and is a newly discovered effect. We also discovered that the leakage current increase can be reverted by γ irradiation without applying bias voltage or by a temperature cycle. The leakage current response to γ -radiation has been extensively studied in the GERDA Detector Laboratory with three prototype detectors. This chapter summarizes leakage current measurements of bare detectors operated in liquid argon and in liquid nitrogen under varying γ irradiation conditions. First, measurements performed with the first prototype detector, which had a full passivation layer, are presented. The γ -radiation induced leakage current, its reversibility and its origin have been investigated. Next, leakage current studies with prototype detectors using different groove passivation procedures, and the dependence of the γ -radiation induced leakage current on the high voltage polarity are reported. Finally, an explanation of the observed phenomenon is given.

4.1 Introduction

A first indication of γ -radiation induced leakage current (LC) appeared already before the dedicated measurements reported in this chapter, in December 2006. Since the tests with the first prototype in the GERDA Detector Laboratory (GDL) test bench started, the LC was systematically monitored approximately once per day. Figure 4.1 illustrates the LC history of the first prototype detector from January 2006 to February 2007. In this period,

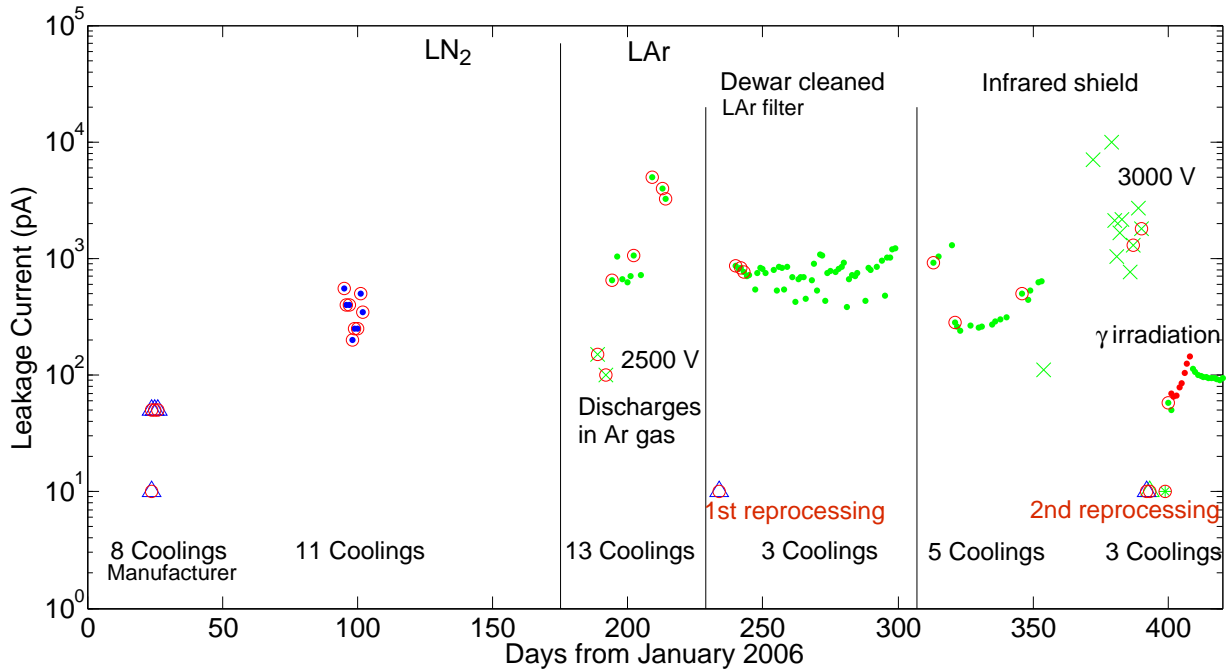


Figure 4.1: Leakage current history of the first prototype detector from January 2006 to February 2007. The blue (green) data have been taken with the detector submerged in liquid nitrogen (liquid argon). The cooling/warming cycles are indicated (\circ). The detector was biased at 4000 V (data with high voltage <4000 V are marked (\times)). Data taken at the detector manufacturer are indicated (Δ). The presence of the ^{60}Co source is shown (\bullet) only after the second reprocessing.

a total of 43 cooling/warming cycles were carried out. At the beginning, the sensitivity was not good enough to observe small changes of LC caused by γ irradiation. Only after eliminating the infrared-induced LC with the installation of the copper shield (see Chapter 3), a first indication of γ -radiation induced LC can be seen with a month-long continuous irradiation with a ^{60}Co source. At the beginning of the measurements, the LC was 100 pA at 3000 V and within one month, the LC increased up to 10 nA. Warming/cooling cycles were performed to restore the LC of the detector, however the LC could not be reduced below ~ 1 nA. The diode was sent to the detector manufacturer for the second reprocessing of the passivation layer¹. When it came back to GDL, the diode was reinserted in the test bench and its LC was constantly monitored. At this time, the origin of the LC increase was not understood. We realized only latter that the LC increase was due to γ irradiation.

¹The first reprocessing was done in August 2006. Prior to the reprocessing, the diode stayed several days under normal atmosphere. Subsequently, a step increase of the LC was observed. As exposed in Chapter 1, surface contamination leads to a deterioration of the passivation layer which results in surface LC.

At the beginning of February 2007 (after the second reprocessing of the diode), the LC of the prototype detector operated in LAr and exposed to a γ -source was observed to increase continuously. The source was subsequently removed, the LC stopped increasing and stabilized at a higher value than prior to the irradiation. This triggered a series of measurements to investigate quantitatively the increase and decrease of the LC of bare HPGe detectors in response to γ irradiation. The measurements were concluded one year later. Detailed descriptions of the tests and measurements with the first prototype detector are given in [48].

4.2 Leakage current studies with a prototype detector with a full passivation layer

For the following measurements, the LC was measured either via the test point voltage (TPV) of the preamplifier using a data logger (which has a range from 50 mV to 30 V) or with a Keithley amperemeter (resolution 10^{-14} A) connected to the detector signal contact. For the high precision measurements with an amperemeter, the preamplifier was disconnected so no spectroscopic measurement was performed. The LC was monitored each minute and the data were averaged over one hour periods. The uncertainty on the average LC was ~ 7 pA and ~ 0.5 pA for the data taken with the data logger and the amperemeter, respectively. As a consequence of the different sensitivities, the plots presented in this chapter show different spreads of the data.

4.2.1 Gamma-radiation induced increase of leakage current in liquid argon

Before coming to the discovered effect of γ -radiation induced increase of LC, let us recapitulate the common response of the detector to γ -radiation. The electron-hole pairs created in response to ionization events inside the germanium detector result in current pulses. This generates a bulk current, here referred to as I_{Bulk} , which is proportional to the count rate:

$$I_{Bulk} = \frac{C \langle E \rangle}{2.96 \text{ eV}/e}, \quad (4.1)$$

where C is the counting rate (Hz), $\langle E \rangle$ is the average energy deposited in the detector (eV), 2.96 eV is the energy necessary to produce an electron-hole pair in the germanium at 80 K and e is the charge on the electron.

For most of the measurements presented here, the detector was biased at 4000 V, slightly above its operational voltage (see Chapter 7). After its second reprocessing, the initial current of the detector was 40 pA in the GDL test bench. Spectroscopy measurements were performed with a ^{60}Co source located at the level of the bottom of the detector assembly, ~ 20 cm away from the center of the detector (Position 1 in Fig.3.4). With the source in Position 1, the total count rate was ~ 1.6 kHz and the measured average energy deposited was ~ 450 keV. Inserting these values in Eq.4.1 gives $I_{Bulk} \approx 39$ pA. The measured current increase when the source was inserted in the test bench was (40 ± 5) pA, in agreement with the calculated value.

The effect which was not expected is that the bulk current step was followed by a continuous increase of the detector LC (Fig.4.2, left). After one week of irradiation, the LC was 165

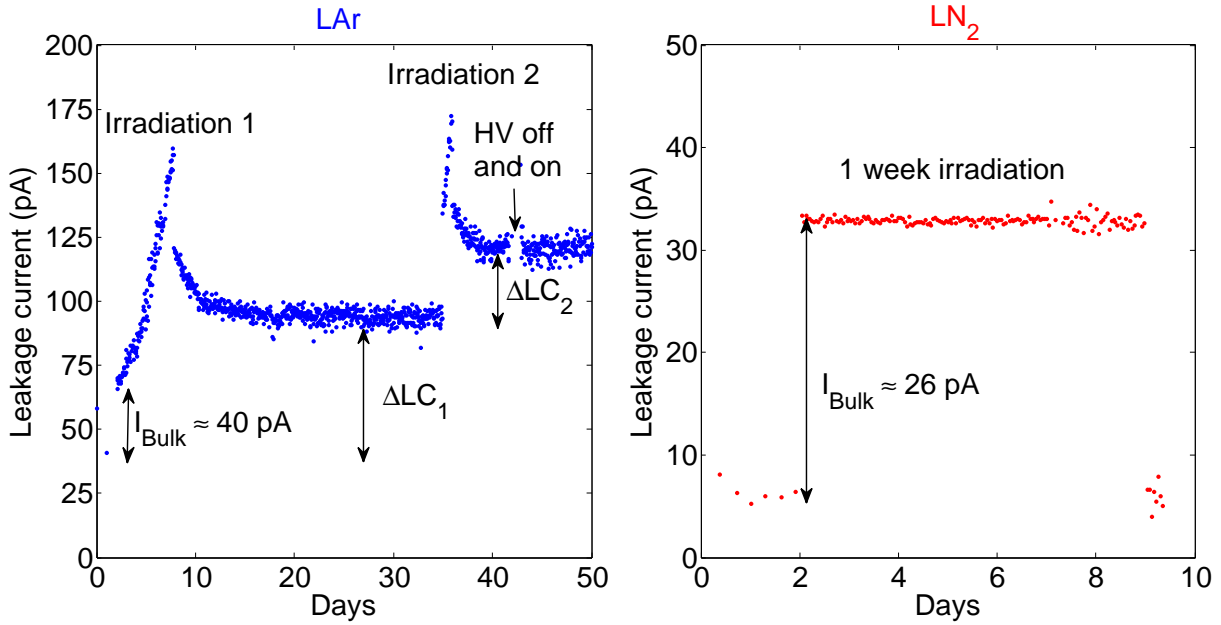


Figure 4.2: **Left:** Gamma-radiation induced LC of the first prototype operated in liquid argon. The first irradiation lasted 1 week and the second one day. The bulk current steps (~ 40 pA) as the source was inserted/removed in the setup are clearly seen. After the irradiations, the LC stabilized at a higher value ($\Delta LC_1 \approx 50$ pA and $\Delta LC_2 \approx 30$ pA). It is also visible that without the source inserted in the setup, removing and increasing back the high voltage had no effect on the LC. The LC was measured with the TPV of the preamplifier (accuracy ~ 7 pA). **Right:** No increase of the LC was observed with the same detector assembly in liquid nitrogen after one week of irradiation. The LC was measured with a high precision amperemeter (accuracy ~ 0.5 pA).

pA. When the source was removed, the bulk current I_{Bulk} step was observed as expected. It was followed by a further gradual decrease of the LC until it stabilized at a higher value than before the irradiation (LC \approx 95 pA). To verify the reproducibility of the result, a 24 hours irradiation with the ^{60}Co source in Position 1 was performed. Once more, the LC increased continuously. The LC increase rate was not linear in time, but showed rather an exponential-like behavior.

Subsequently, the effect on the LC of removing the high voltage (HV) and increasing it back was investigated. The HV was first switched off for one hour (Fig.4.2, left) and then, for 25 hours. The γ -source was not inserted in the setup during these tests. In both cases, after increasing the HV back the LC returned to the same value as before switching it off.

To investigate whereas the γ -radiation induced LC is specific to LAr, Prototype 1 was operated in liquid nitrogen (LN_2) under the same irradiation condition (Fig.4.2 right). Two observations can be made. First, the steady LC was lower in LN_2 than in LAr (in LN_2 , the LC was \sim 10 pA, the same as measured at the detector manufacturer). Second, the bulk current I_{Bulk} step as the source was inserted was observed, but no additional increase of the LC was measured even after one week of γ irradiation.

The γ -rays from the source cause ionization in both the germanium and the cryogenic liquid. It is known that charges can be drifted over long distances in LAr. The observation that γ -radiation induced LC happens in LAr but not in LN_2 led to the hypothesis that charges produced in LAr are responsible for the LC increase. The charges can be collected only on the detector passivation layer as on the conductive surfaces they are immediately compensated.

4.2.2 Reversibility of the γ -radiation induced leakage current

Then, we discovered that the γ -radiation induced LC is a reversible process. The LC can be totally restored to its initial value by doing a temperature cycle. The fact that the γ -radiation induced LC is reversible indicates that this effect causes no damage to the detector. Once more, it points towards charge collection on the passivated detector surface. Charges can be neutralized or removed which explains the reversibility of the effect.

Moreover, γ irradiations without applying HV to the detector also resulted in a decrease of the LC (Fig.4.3). After 24 hours of irradiation without HV, the ^{60}Co source was removed, the HV increased back to 4000 V and a decrease of the LC was measured ($\Delta\text{LC} \approx -30$ pA). This process was repeated with another 24 hour, 48 hour and 72 hour irradiation. After each irradiation, a decrease of the LC was observed. However, two days after the last irradiation without HV, the LC increased by 10 pA and stabilized at 90 pA. Thus, γ irradiation without HV could reduce the detector LC only down to a certain limit.

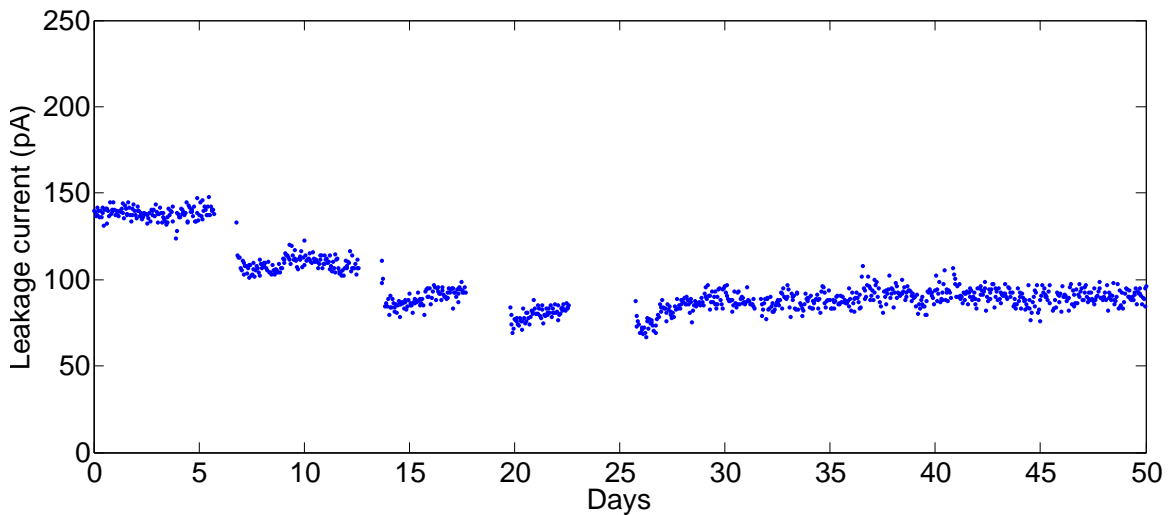


Figure 4.3: Decrease of the LC after four consecutive irradiations without applying high voltage. The high voltage was applied in between the irradiations to measure the LC. The accuracy on the LC is ~ 7 pA.

The scintillation properties of liquid argon are well established [55]. Ionization of LAr produces the argon excimer Ar_2^* which decays under emission of a photon with a wavelength of $\lambda = 128$ nm. It is hypothesized that the ultraviolet (UV) scintillation photons from LAr, breaking the bonds between the charges and the passivation layer, are responsible for the decrease of the LC when no HV is applied to the detector.

4.2.3 Role of the passivation layer in the γ -radiation induced leakage current

To investigate the origin of the γ -radiation induced LC, an irradiation was performed with the source in Position 2 (Fig.3.4). The two source positions are symmetric with respect to the center of the detector. The source in Position 1 irradiates mainly the LAr volume facing the passivation layer and the source in Position 2 irradiates mainly the LAr volume on top of the detector assembly (HV contact side). Figure 4.4 compares the γ -radiation induced LC with the source in Position 1 and in Position 2. Both irradiations lasted 24 hours. For the same distance source-detector, the LC increase was stronger with the source in Position 1 ($\Delta LC_{in} \approx 45$ pA) as compared to the source in Position 2 ($\Delta LC_{in} \approx 15$ pA). It reinforced the hypothesis that the origin of the γ -radiation induced LC is related to the passivation layer.

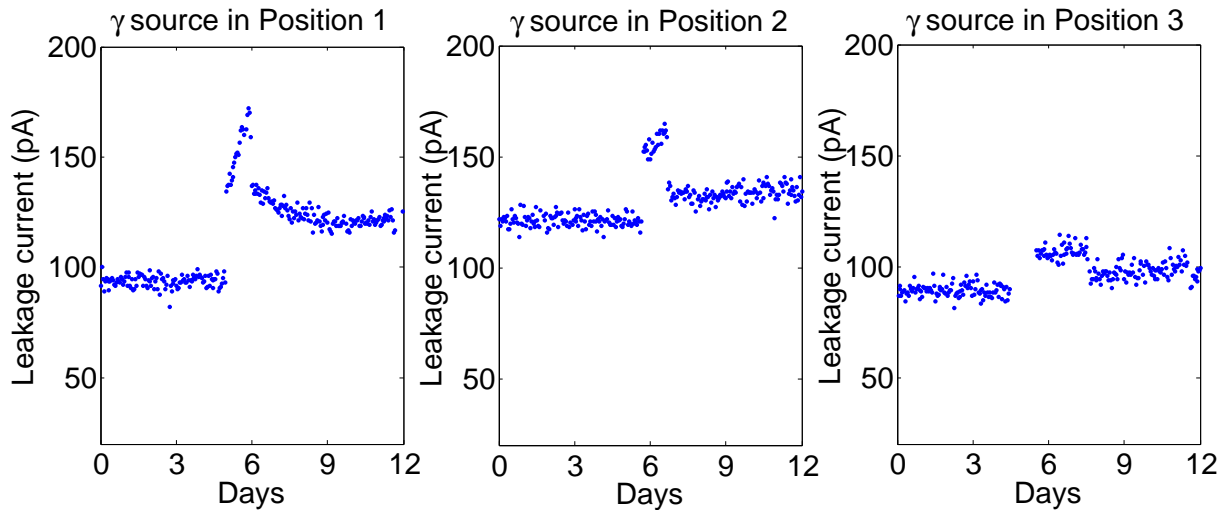


Figure 4.4: Comparison between γ -radiation induced LC in liquid argon with the source in Positions 1, 2 and 3. The accuracy on the LC measurement was ~ 7 pA.

Another measurement was performed with the source located higher (in Position 3), where the total counting rate was a factor ~ 2 smaller than with the source in Position 1 and 2. The LC increase per day of irradiation with the source in Position 3 was approximately a factor 2 smaller than with the source in Position 2 (Fig.4.4).

To test the assumption that charges produced by LAr ionization close to the passivation layer are collected on the surface, another measurement was performed. The idea was

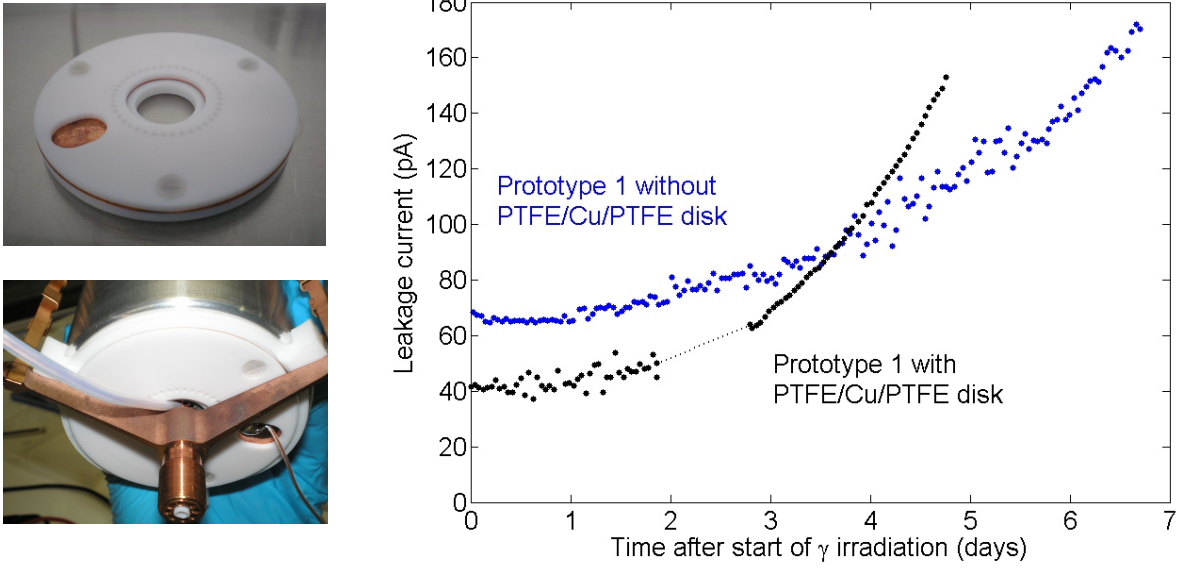


Figure 4.5: **Left:** PTFE/Cu/PTFE disk mounted on the bore hole side of the diode to protect the passivation layer. **Right:** Gamma-radiation induced LC with Prototype 1 mounted with and without the PTFE/Cu/PTFE disk. The data without the disk refer to the first irradiation. For the data taken with the protective disk, three distinct irradiations are presented as continuous. For the second irradiation with the disk (day 2-3), the LC was monitored only at the beginning and at the end of the irradiation. The LC without the disk, and with the disk at the first and second irradiations was measured with the TPV (accuracy ~ 7 pA). For the third irradiation with the disk, the LC uncertainty was ~ 0.5 pA.

to mitigate the γ -radiation induced LC by preventing the collection of charges on the passivation layer. This was performed with a grounded copper disk covering the passivation layer, insulated from the diode and the holder with the two PTFE disks (Fig.4.5). The new assembly was cooled down and HV applied to the detector. After the temperature cycle, the LC was 10 pA. Several γ irradiations were carried out with HV applied to the detector. Figure 4.5 compares the γ -radiation induced LC of Prototype 1 mounted with and without the PTFE/Cu/PTFE disk. For both configurations, no increase of the LC was observed during the first day of irradiation. Then, the LC started to increase. Surprisingly, the LC increasing rate was stronger for the detector assembly with the protective disk even though the initial LC was lower.

Gamma irradiations with the PTFE/Cu/PTFE disk were also performed without applying HV to test the hypothesis of the curing effect of the UV scintillation photons. No γ -radiation induced decrease of the LC when no HV was applied was observed with the PTFE/Cu/PTFE disk. As opposed to the γ -rays emitted from the ^{60}Co source, the scintillation photons cannot travel through the copper disk and reach the passivation layer.

This indicates that the direct interaction of the γ -rays from the source with the passivation layer is not responsible for the LC decrease, which was observed without the protective disk when no HV was applied. This supports the assumption that the curing agent is the UV scintillation photons of LAr.

4.3 Leakage current studies with prototype detectors with modified groove passivation procedures

The role of the passivation layer in the γ -radiation induced LC in LAr was further studied with two other prototype detectors using different groove passivation procedures. Prototype 2 had a reduced passivation layer limited to the groove area and Prototype 3 had no passivation layer evaporated (Fig.2.3). The operational voltage for Prototype 2 and Prototype 3 is 3000 V and 3500 V, respectively (Chapter 6). For the measurements presented here, the detectors were biased above their operational voltage, at the same value as Prototype 1 (4000 V). Figure 4.6 compares the γ -radiation induced LC of the three detectors in LAr. The γ -radiation induced LC of Prototype 2 was suppressed compared to the first prototype (10 pA/week vs. 80 pA/week). The third prototype showed no increase of the LC even after one week of irradiation. It showed that the charge collection on the passivation layer is at the origin of the γ -radiation induced LC.

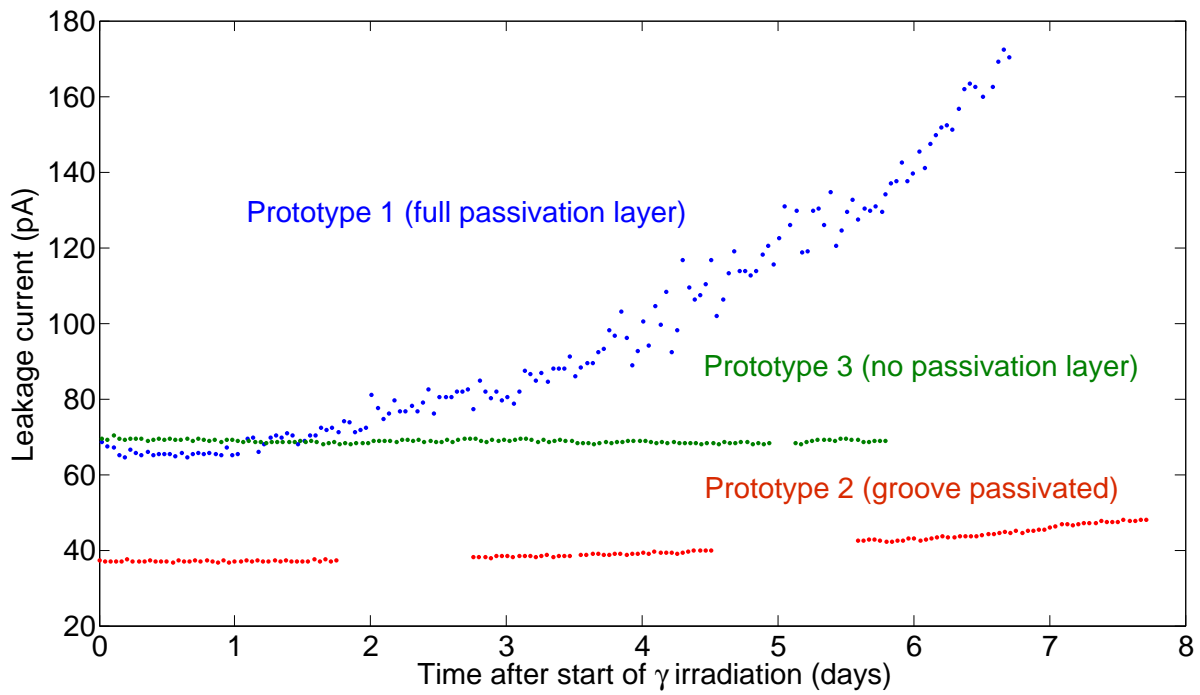


Figure 4.6: Leakage current in function of days of γ irradiation in liquid argon for three prototype detectors using different groove passivation procedures. The leakage current of Prototype 1 was measured with the TPV of the preamplifier (accuracy ~ 7 pA) and the LC of Prototype 2 and 3 with an amperemeter (accuracy ~ 0.5 pA).

4.4 Dependence of the γ -radiation induced leakage current on high voltage polarity

To investigate the effect of the electric field, present in the LAr volume surrounding the detector, on the γ -radiation induced LC, measurements were performed with inverse HV polarity: $-$ HV was applied to the p+ contact and the n+ contact was grounded. Inverting the polarity did not change the electric field inside the detector, neither inside the LAr volume contained in the groove. However, it did change the field in the surrounding of the assembly because the detector holder and the infrared shield were kept grounded.

Figure 4.7 compares the LC increase of the first prototype detector with $+ HV$ and $- HV$. The LC was higher and it increased faster with $- HV$. The increase of the LC per day

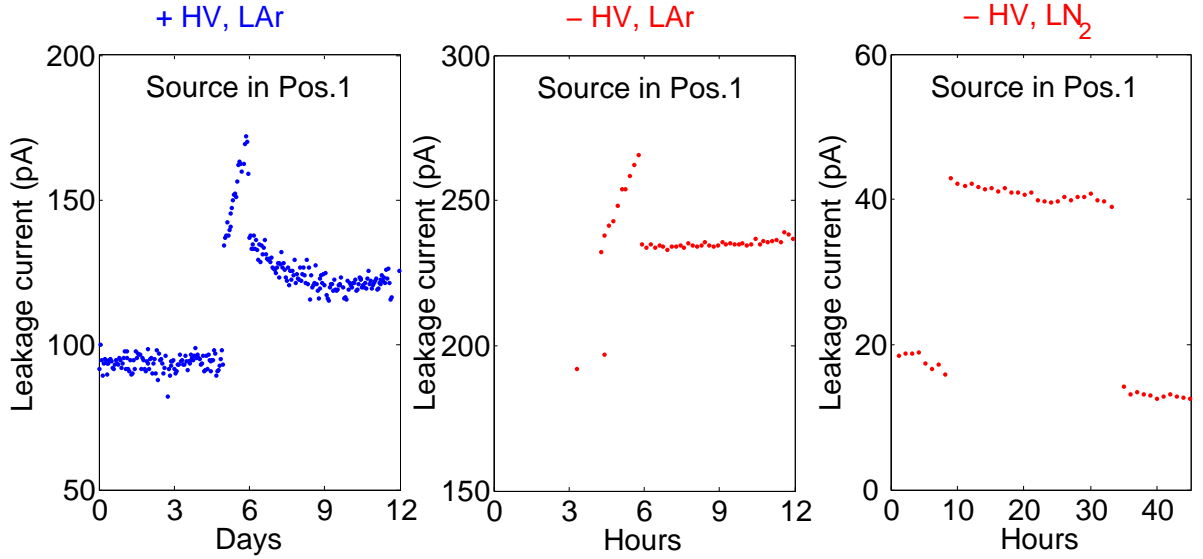


Figure 4.7: Comparison of the γ -radiation induced LC with $+ HV$ and $- HV$ for Prototype 1. In LAr, the same LC increase was measured after one day of irradiation with $+ HV$ as after one hour of irradiation with $- HV$. No increase of the LC was observed after more than one day of irradiation with $- HV$ in LN₂. For the $+ HV$ configuration, the LC was measured with the TPV of the preamplifier (accuracy ~ 7 pA). For the $- HV$ configuration, the LC was measured with an amperemeter (accuracy ~ 0.5 pA). The LC steps (I_{Bulk}) as the source is inserted or removed are clearly seen.

of irradiation with $+ HV$ was similar to the increase per hour of irradiation with $- HV$. Various irradiations with Prototype 1 biased at -4000 V were performed in LAr and in LN₂. For all measurements carried out in LAr, a steep increase of the LC was observed. On the contrary, no increase of the LC was measured after one day of irradiation in LN₂

(Fig.4.7). These results indicated that charge collection on the whole passivated surface, and not only on the passivation layer in the groove, is responsible for the γ -radiation induced LC. This is because the field in the groove does not change with the HV polarity, as was already noted.

Gamma irradiations with inverse HV polarity were also performed with Prototype 2 and 3. Figure 4.8 compares the γ -radiation induced LC measured with these detectors for the two HV configurations. A similar result as with Prototype 1 was obtained with Prototype 2: the LC increase per day with + HV was similar to the LC increase per hour with - HV. Prototype 3, which showed no LC increase after 1 week of irradiation with + HV, showed an increase of 8 pA after 25 hours of irradiation with - HV. These results were surprising. As Prototype 2 had a passivation layer limited to the groove area and inverting the HV does not change the electric field inside the groove, no difference between the + HV and - HV configuration was expected. Obviously, no LC increase was expected with Prototype 3 as it has no passivation layer. The stronger LC increase with Prototype 2 at - HV could be explained if the passivation layer extended slightly outside the groove. Prototype 3 had no passivation layer evaporated but it could have a naturally oxidated germanium layer. The small LC increase observed can possibly be due to charge collection on the germanium oxide layer.

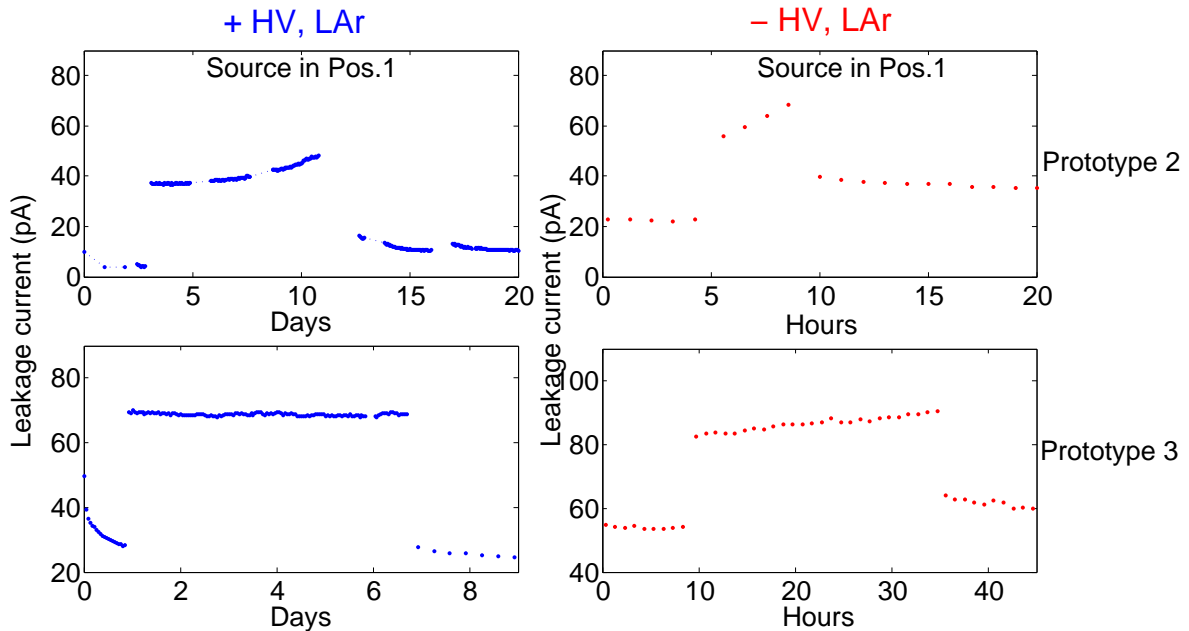


Figure 4.8: Comparison of the γ -radiation induced LC in liquid argon, for Prototype 2 and 3, with + HV and - HV. The uncertainty on the LC is ~ 0.5 pA. The LC steps (I_{Bulk}) as the source is inserted or removed are clearly seen.

A difference in the steady LC between the + HV and – HV configuration was observed with Prototype 1 and 2. Table 4.1 gives the LC measured with + HV and the corresponding LC measured with – HV for Prototype 1 in LAr and in LN₂ as well as for Prototype 2 and 3 in LAr. The LC difference between + HV and – HV is not significant for Prototype 3. All given LC were measured on the ground side of the detectors with an amperemeter. The total current flowing to ground was simultaneously measured on the HV side for both HV configurations and the values agreed within 10 pA with the LC measurements.

HV Scheme	Prototype 1 in LAr (pA)	Prototype 1 in LN ₂ (pA)	Prototype 2 in LAr (pA)	Prototype 3 in LAr (pA)
+ HV	100±1	5±2	8±2	50±5
– HV	200±10	12±3	22±2	55±5

Table 4.1: Steady leakage current with + HV and the corresponding leakage current with – HV for the three prototype detectors.

The LC difference between + HV and – HV depends on the LC level (Fig.4.9). At higher LC, the difference was larger.

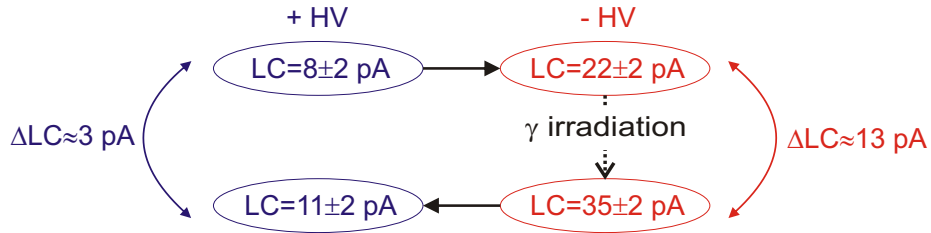


Figure 4.9: Difference of the steady leakage current between the + HV and – HV configuration, before and after a γ irradiation, measured with Prototype 2. The black arrows indicate the time sequence of the measurements.

4.5 Irradiation measurement summary

Tables 4.2 and 4.3 summarize the γ irradiation measurements with Prototype 1, 2 and 3. A total of 29 irradiations were performed with Prototype 1, 8 with Prototype 2 and 3 with Prototype 3. Some of the measurements were presented in the previous sections, further ones are explained here.

An irradiation with Prototype 1 biased at 2000 V was performed to study the influence of the bias HV value on the γ -radiation induced LC. No increase of the LC was observed after 65 hours of irradiation. The source was removed and the HV was increased to 4000 V. Only at this bias voltage an increase of the LC was observed ($\Delta LC \approx 60$ pA), thus showing a non-ohmic behavior of the γ -radiation induced LC. Irradiations were also performed using a ^{226}Ra source. Figure 4.10 shows a ^{60}Co and a ^{226}Ra spectrum measured with the first prototype detector in Test Bench 1. The γ -radiation induced LC increases observed with the ^{226}Ra and the ^{60}Co source were similar.

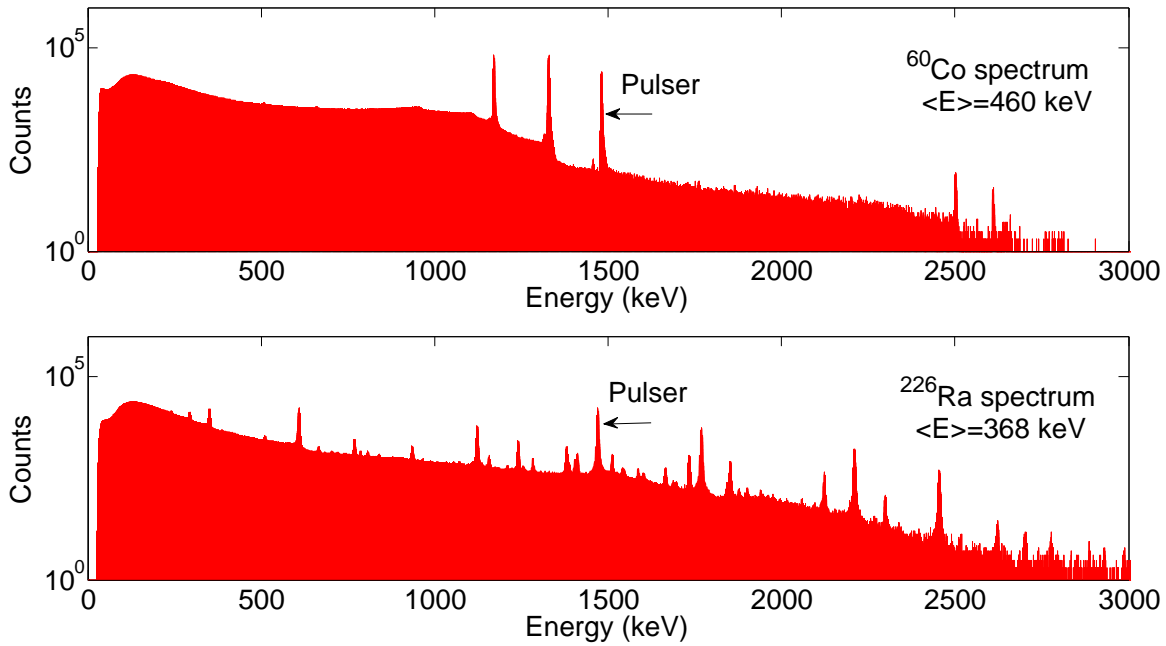


Figure 4.10: ^{60}Co (top) and ^{226}Ra (bottom) spectrum measured with the first prototype detector in Test Bench 1. The average energy deposited ($\langle E \rangle$) was determined by integrating the spectrum, correcting for the data acquisition threshold and the generator pulses.

To test if the ultraviolet (UV) scintillation photons from LAr were responsible for the decrease of the LC when no HV was applied, a UV-LED was mounted on a steel bar attached to the infrared shield lid of Test Bench 2. It allowed to irradiate the passivation layer side of the detector assembly (Fig.4.11). The LED emits UV light at an energy of ~ 3 eV (compared to 10 eV for LAr scintillation light). The number of photons reaching the bottom surface of the detector was calculated with the specified optical power output (1 mW in 2π solid angle) for the LED mounted ~ 4 cm below the detector. Assuming no absorption in LAr, the number of photons reaching the passivation layer in one second of LED irradiation ($\sim 10^{14}$ γ/s) was three orders of magnitude larger than in 24 hours of ^{60}Co

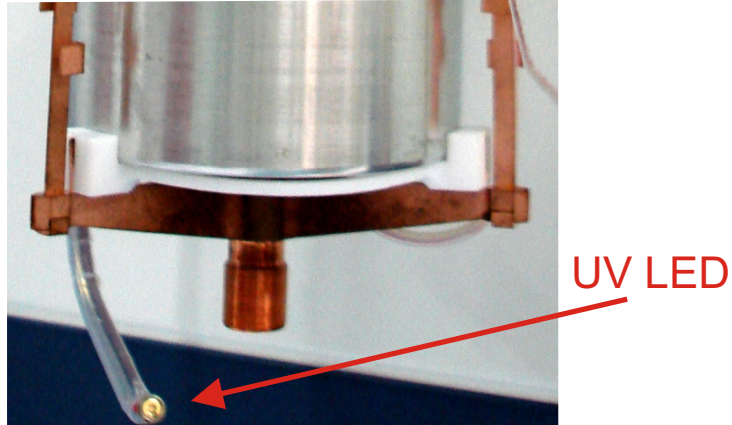


Figure 4.11: Ultraviolet-LED mounted at the bottom of the detector assembly. Irradiations were performed with the second prototype in Test Bench 2.

irradiation (see Section 3.7.5). Several LED irradiations were performed with Prototype 2 without applying HV. Right after irradiating the detector assembly with the LED the LC was higher, and then it decreased. It took several days before the LC stabilized and no LC decrease as compared to before the irradiation was observed. However, the tests were done at low LC (~ 20 pA) and the effect of the irradiation without HV with the ^{60}Co source was noticed at higher LC (~ 100 pA). Therefore, these results are not conclusive.

In summary, the γ radiation-induced LC in LAr has been investigated with different HV nominal values, source-detector configurations and HV polarities using three prototype detectors. The main observations are the following:

- The LC increases continuously when detectors with a passivation layer biased with HV and operated in LAr are exposed to γ -radiation.
- No γ -radiation induced LC is observed in LN_2 .
- Gamma-radiation induced LC is a reversible process.
- The LC increase rate depends on the distance between the γ -source and the passivation layer, the surface of the detector passivation layer inside and outside the groove, and on the electric field in the surrounding LAr volume.

Irr.	Date	Source	Pos.	HV	$\langle E \rangle$	Exp.	C.rate	ΔLC					
								Bulk	B-in	in	B-out	out	total
LAr													
1	9-16/02/07	^{60}Co	1	+4	445	6.9 d	1615	39	+41	+80	-40	-30	+51
2	15-16/03/07	^{60}Co	1	+4	445	1.0 d	1525	37	+40	+45	-40	-18	+28
3	2-3/04/07	^{60}Co	2	+4	440	1.0 d	1310	31	+35	+13	-33	-5	+10
4	20-21/04/07	^{60}Co	1	0	-	0.9 d	-	-	-	-	-	-	-30
5	27-28/04/07	^{60}Co	1	0	-	0.9 d	-	-	-	-	-	-	-15
6	2-4/05/07	^{60}Co	1	0	-	1.9 d	-	-	-	-	-	-	-10
7	7-10/05/07	^{60}Co	1	0	-	3.0 d	-	-	-	-	-	-	+5
8	15-17/06/07	^{60}Co	3	+4	405	2.1 d	620	14	+14	+10	-17	+3	+10
9	22-25/06/07	^{60}Co	1	+2	445	2.7 d	1470	35	+36	0	-36	0	+59
10	26-28/06/07	^{60}Co	1	0	-	1.7 d	-	-	-	-	-	-	-55
11	4-5/07/07	^{60}Co	1	0	-	1.1 d	-	-	-	-	-	-	0
12	6/07/07	^{60}Co	1	-4	-	1.7 h	-	-	+33	+37	-35	+10	+45
13	7/07/07	^{60}Co	1	-4	-	1.5 h	-	-	+31	+37	-33	+5	+40
14	8-9/07/07	^{60}Co	1	0	-	1.0 d	-	-	-	-	-	-	-85
15	10/07/07	^{60}Co	1	0	-	12 h	-	-	-	-	-	-	-10
16	11/07/07	^{226}Ra	1	-4	-	1.8 h	-	-	+22	+38	-25	0	+35
17	11-12/07/07	^{60}Co	1	0	445	0.7 d	-	-	-	-	-	-	-10
18	13-14/07/07	^{226}Ra	1	+4	370	1.0 d	1155	23	+23	+30	-25	-3	+25
19	15-17/07/07	^{60}Co	1	0	-	1.9 d	-	-	-	-	-	-	-53
With PTFE/Cu/PTFE Disk													
20	24-26/07/07	^{60}Co	1	+4	460	2 d	1440	36	+35	+8	-	-	+8
21	26-28/07/07	^{60}Co	1	0	-	2.0 d	-	-	-	-	-	-	0
22	13-14/08/07	^{60}Co	1	+4	460	0.9 d	1440	36	+34	+14	-34	-4	+10
23	17-20/08/07	^{60}Co	1	0	-	3.0 d	-	-	-	-	-	-	-1
24	29-31/01/08	^{60}Co	1	+4	460	2.0 d	1440	36	+29	100	-30	-	+99

Irr.	Date	Source	Pos.	HV	$\langle E \rangle$	Exp.	C.rate	ΔLC				
								Bulk	B-in	in	B-out	out
LAr												
25	01-03/02/08	^{60}Co	1	+4	-	1.9 d	-	+25	+75	-25	-20	+55
26	04-05/02/08	^{60}Co	1	0	-	0.9 d	-	-	-	-	-	-15
27	06-07/02/08	^{60}Co	1	+4	-	0.8 d	-	+23	+48	-21	-1	+49
LN₂												
28	17-24/02/08	^{60}Co	1	+4	-	7 d	-	+26	+3	-30	0	-1
29	25-26/02/08	^{60}Co	1	-4	-	1.1 d	-	+26	-2	-27	-3	-6

Table 4.2: Irradiation test summary for Prototype 1: Irradiation, date, source, position of the source, high voltage (kV), average energy deposited in the detector (keV), exposure time (days), counting rate (Hz), bulk current variation calculated using Eq.4.1 (ΔLC_{Bulk}) and measured when the source is inserted (ΔLC_{B-in}), LC variation with the source inserted (ΔLC_{in}), bulk current variation measured when the source is removed (ΔLC_{B-out}), LC variation after the source is removed (ΔLC_{out}) and finally, difference of LC before and after irradiation (ΔLC_{total}) at 4000 V. The average energy deposited ($\langle E \rangle$) was determined by integrating the measured spectra. The LC variations are given in pA. The errors on the ΔI and ΔLC are ≤ 5 pA. The data acquisition threshold was set to ~ 30 keV. The counting rates and the given average deposited energies were corrected for the threshold, assuming a flat distribution at low energies.

Irr.	Date	Source	Pos.	HV	$\langle E \rangle$	Exp.	C.rate	ΔLC					
								Bulk	B-in	in	B-out	out	total
LAr Prototype 2													
1	11-19/12/07	^{60}Co	1	+4	450	7.7 d	1372	33	+32	+11	-32	-2	+9
2	19-20/12/07	^{60}Co	1	0	-	0.9 d	-	-	-	-	-	-	-1
3	21/12/07	LED	-	0	-	10 s	-	-	-	-	-	-	-5
4	24/12/07	LED	-	0	-	2 min	-	-	-	-	-	-	0
5	29/01/08	LED	-	0	-	5 min	-	-	-	-	-	-	+2
6	07/02/08	^{60}Co	1	-4	-	4.5 h	-	33	+33	+16	-31	-5	+13
7	10/02/08	LED	-	0	-	10 min	-	-	-	-	-	-	0
8	11-12/02/08	^{226}Ra	1	0	-	0.8 d	-	-	-	-	-	-	+2
LAr Prototype 3													
1	11-17/02/08	^{60}Co	1	+4	450	5.8 d	1372	33	+40	+1	-40	-1	0
2	24-25/02/08	^{60}Co	1	-4	-	1.1 d	-	-	+29	+6	-26	+2	+11
3	26-27/02/08	^{60}Co	1	0	-	0.8 d	-	-	-	-	-	-	0

Table 4.3: Irradiation test summary for Prototype 2 and Prototype 3 (see Table 4.2 for explanation). No spectrum was collected with Prototype 3 as an amperemeter connected to the signal contact was always used to monitor the LC. Prototype 2 and 3 have very similar dimensions and were operated in the same source-detector configuration. Thus, ΔLC_{Bulk} for Prototype 3 was calculated using the counting rate and the average energy deposited from Prototype 2.

4.6 Explanation of the γ -radiation induced leakage current

The most likely explanation of the γ -radiation induced LC is the collection and trapping of charges on the surface of the detector passivation layer. This results in a decrease of the resistivity of the layer and an increase of the LC. The charges are produced by the ionization of LAr and are drifted towards the detector surface by the electric field.

4.6.1 Electric field calculation

The HV bias of the detector produces a strong electric field in the surrounding LAr which can transport charges towards the electrodes. The electric field was numerically calculated by Assunta DiVacri using the Maxwell 2D code [56]. The resulting direction and magnitude of the electrostatic field for + HV configuration is shown in Figure 4.12. The setup geometry used in the calculation is a longitudinal section of the detector (including the intrinsic germanium bulk, and the n+ and p+ contact) and the holder, placed in the infrared shield filled with LAr. Both the holder and the infrared shield are grounded. The LAr volume surrounding the detector experiences electric field strength of up to ~ 10 kV/cm. A comparison of the electrostatic field for the + HV and – HV configuration, focused on the passivation layer side, is shown in Figure 4.13. The field lines indicate that positive and negative charges are collected respectively on the inner and outer part of the passivation layer in both HV configurations. The direction of the electric field is orthogonal to the detector surface, except in the groove where it is parallel to the surface. The volume of LAr from where the charges are transported towards the detector passivation layer is principally the volume below the detector bottom surface.

4.6.2 Charge production in LAr

The energy required to ionize argon and produce an e^-Ar^+ couple is 23.6 eV. The average charge production rate in LAr is then

$$\langle A \rangle_{LAr} = \frac{C \cdot \langle E \rangle}{23.6 \text{ eV}/e}, \quad (4.2)$$

where C is the rate of ^{60}Co interactions in LAr and $\langle E \rangle$ is the mean energy deposited in LAr. The spectrum of the deposited energy and the ionization rate in LAr were determined with a Geant4 [57] based Monte Carlo simulation [58]. The software description of the

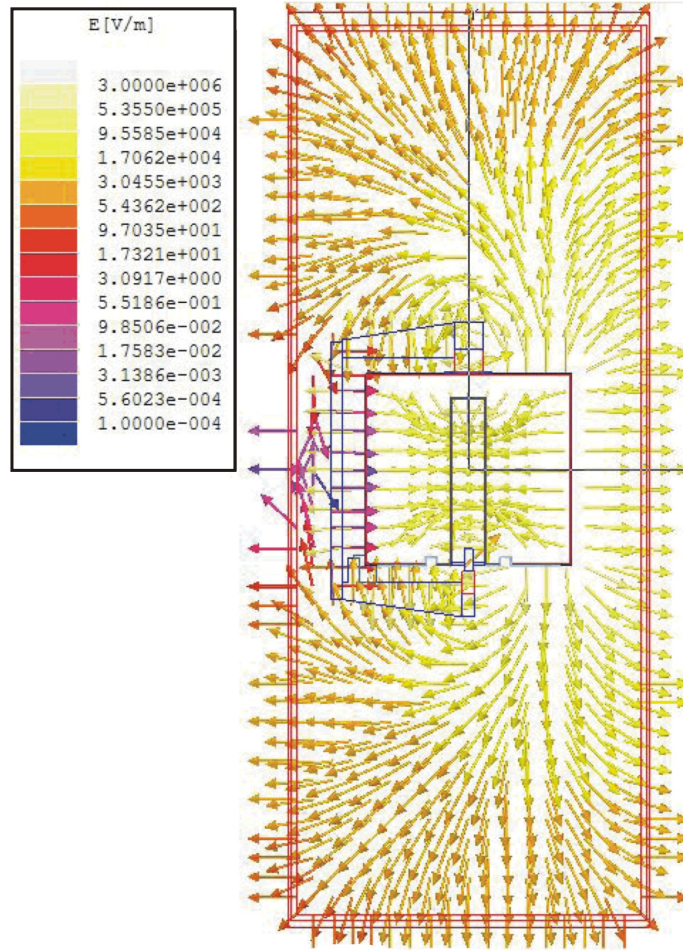


Figure 4.12: Direction and magnitude of the electric field for the + HV configuration.

setup included the detector, the dewar inner vessel and the infrared shield. Both the inner vessel and the infrared shield were filled with LAr. The position of the source was set to reproduce the experimental count rate of the detector. The LAr volume considered for the LAr ionization rate was a cylinder contained in the infrared shield, just below the passivation layer, with a height of 4 cm ($V \approx 0.5$ l). For this volume, the mean energy released is ~ 300 keV and the ionization rate is $C \approx 1.7$ kHz. Inserting these numbers into Eq.4.4 gives $\langle A \rangle_{LAr} \approx 3$ pC/s.

4.6.3 Charge collection on the passivation layer

In the presence of an electric field, the electrons and Ar-ions produced by the ionization of LAr are separated and travel towards the respective electrodes. The charges can reach

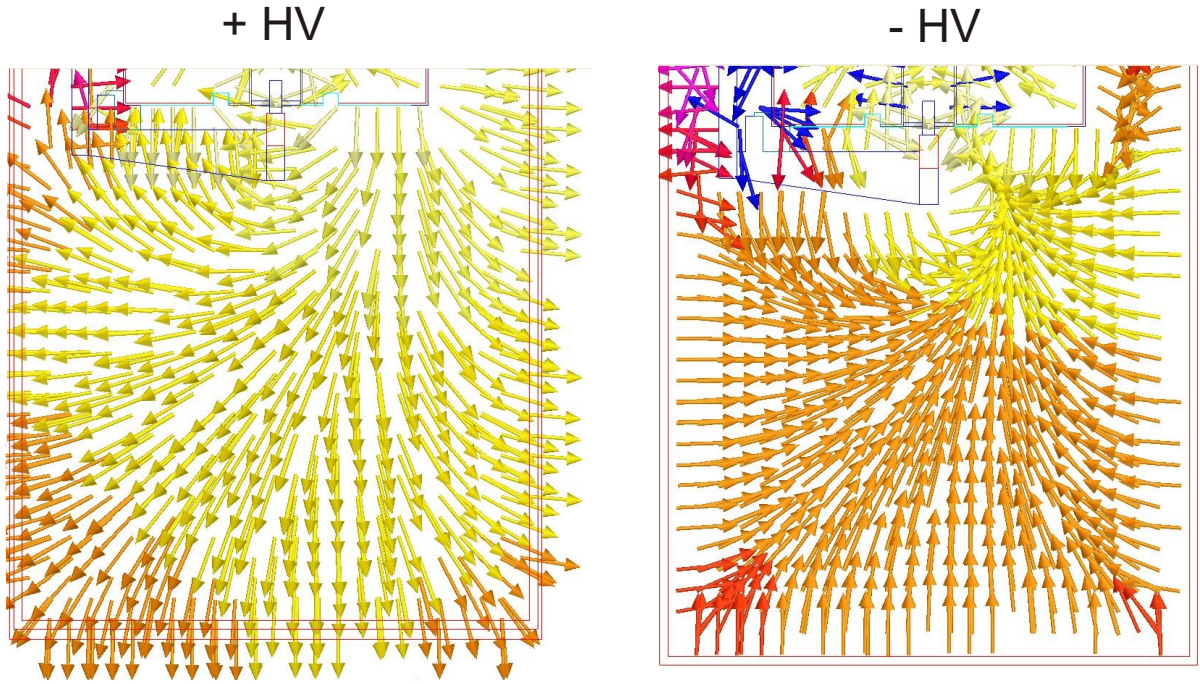


Figure 4.13: Electric field calculations for the + HV and - HV configuration (zoom on the passivation layer and the liquid argon volume below it). The color-coded field strength scale is on the same order as in Fig.4.12.

the electrodes if no recombination takes place. The charge survival probability increases with the strength of the electric field [59]. If the electric field is below 200 V/cm, this probability is < 20%. If the electric field is ~ 1 kV/cm, the charge survival probability is above 80%. Accordingly, an effective LAr volume, from which all charges are assumed to be collected on the passivation layer, was defined where the electric field strength is ≥ 200 V/cm. The effective volume depends on the HV and the charge polarity. The ionization rate determined by Monte Carlo simulation is assumed to be homogeneous and is linearly scaled with the different effective volumes.

The amount of charge collected on the detector passivation layer was estimated under the assumption that all charges produced by the ionization of LAr in the effective volume are collected, and there is no charge recombination at the passivation layer. The results are reported in Table 4.4 in terms of charge density and ion density per day of irradiation with Prototype 1 and the source in Position 1 [60]. The difference of two orders of magnitude in the positive charge density between the two HV configurations allows to hypothesize that mainly positive charges are responsible for the LC increase.

HV configuration	Positive charge (pC·cm ⁻²)	Positive ion density (ion·cm ⁻²)	Negative charge (pC·cm ⁻²)	Negative ion density (ion·cm ⁻²)
+ HV	2.4 · 10 ²	1.5 · 10 ⁹	2.0 · 10 ³	1.1 · 10 ¹⁰
- HV	1.8 · 10 ⁴	1.1 · 10 ¹¹	6.5 · 10 ²	4.0 · 10 ⁹

Table 4.4: Estimated density of charge and ions collected on the passivation layer per day of irradiation for Prototype 1 and the source in Position 1 [60].

4.6.4 Conductivity of the passivation layer

The charge collected on the passivation layer results in a decrease of its resistivity (for the observed $\Delta I = 40$ pA with HV = 4 kV, the required change is $\Delta R = 10^{14}$ Ω). The passivation material is silicon oxide (most probably SiO₂). The rate of the LC increase depends on the charge collection rate, the density of trapped charge, and the starting value of the passivation layer resistivity. Applying the Gauss theorem to an infinite charged sheet gives the induced electric field inside the passivation layer:

$$E = \frac{\sigma}{2\epsilon}, \quad (4.3)$$

where σ is the charge density and ϵ the dielectric constant of the passivation layer material ($\epsilon \approx 4\epsilon_0$ for SiO₂). Using the values from Table 4.4, the electric field induced by the collected charges is $\sim 10^2 - 10^4$ V/cm. Assuming a passivation layer thickness of ~ 0.2 μm gives a potential difference across the layer on the order of 1-100 mV.

Silicon dioxide is widely studied in the field of microelectronics and various studies of LC effects in this material are reported by many authors (e.g. [61]). The current conduction mechanisms include direct tunneling, Fowler-Nordheim tunneling, trap-assisted tunneling and Poole-Frenkel conduction [62]. Charging of SiO₂ by corona discharge is a known technique to perform contactless surface charge for semiconductor characterization. As the charge is deposited on the oxide, the surface voltage increases until the charge density leaks through by Fowler-Nordheim tunneling or direct tunneling. Silicon dioxide breaks down at electric fields of 10-14 MV/cm [63]. This is much higher than the electric field created by the collection of charge in LAr. Thus, in our case, no breakdown occurs. The Poole-Frenkel emission is observed in deposited insulators which contain a high density of structural defects. It involves field-enhanced thermal emission of electrons from trap states into the conduction band of the insulator. This is unlikely to happen because in our case, the layer is at LAr temperature.

The phenomenon reported here is different from what can be found in the literature for

several reasons. The oxide layer is much thicker (hundreds of nm) as compared to semiconductor devices where typical thicknesses are on the order of nm. Furthermore, it is at LAr temperature and it is deposited on highly doped germanium (apart in the groove where the interface semiconductor/SiO₂ is present). Most probable, the observed effect is a surface conductivity caused by the potential difference between the opposite sides of the groove.

4.6.5 Ultraviolet curing effect

The γ -radiation induced decrease of the LC when no HV is applied to the detector can be explained by the effect of UV scintillation photons from LAr. Ultraviolet annealing of SiO₂ is a known process. The effect of the UV scintillation light is to break the bonds between the ions and the passivated surface, i.e. to free the trapped charges. The photon rate at the detector passivation layer is:

$$\langle IR \rangle_{\gamma} = C \cdot \langle E \rangle \cdot LY \cdot \Omega / 4\pi, \quad (4.4)$$

where LY is the LAr light yield ($\sim 4 \cdot 10^4$ photon/MeV [59]) and Ω is the solid angle subtended by the passivation layer. Using the ionization rate (C) and the average energy deposited $\langle E \rangle$ for the volume considered in the Monte Carlo simulation gives $\langle IR \rangle_{\gamma} \approx 10^6$ photons/s.

4.7 Discussion

The model presented in the previous section is empirical and qualitative, but allows to explain most of the experimental results of the extensive study on the γ -radiation induced LC. In contrary to LN₂, charges can be drifted over long distances in LAr. The model explains the different results measured with the source in Position 1 and 2, and with + HV and - HV for Prototype 1. It also explains that a reduced LC increase and no increase was observed with Prototype 2 and Prototype 3, respectively, biased with + HV. However, some observations stay without explanation: the LC increasing rate with Prototype 1 mounted with the PTFE/Cu/PTFE disk, the difference between the steady LC with + HV and - HV, and the stronger γ -radiation induced LC with - HV compared to + HV for Prototype 2 and 3.

How and where exactly does the current flow? How can charges on the passivation layer outside the groove affect the conductivity inside the groove? Is it really a surface phenomenon or could some trap assisted tunnelings take place? These questions are still not

answered. To understand further the γ -radiation induced LC, an experiment capable of measuring quantitatively the charge collected on the passivation layer and its corresponding change of conductivity should be carried out. This would be beyond the scope of this work.

The increases of the LC reported here were at a very small scale and occurred after a relatively long exposure to γ -radiation. No long-term γ irradiation of the detectors is planned within the GERDA experiment. Calibrations with γ -sources will be performed approximately once per week for several minutes. Starting at low LC, even considering the same increase rate as observed with Prototype 1, the γ radiation-induced LC expected during the lifetime of GERDA is on the order of few pA and gives a negligible contribution to the energy resolution. However, the discovery and the awareness of this effect are very valuable for operation of bare germanium detectors in LAr.

4.8 Conclusions

Gamma-radiation induced LC was observed for the first time in the scope of this thesis. A one year study of the LC of bare HPGe detectors operated in LAr and LN₂ under varying γ irradiation conditions has been performed. Gamma irradiation of the first prototype detector in LAr resulted in a continuous increase of the LC. No increase was observed in LN₂. The process is reversible as the LC was partly restored by irradiation without applying HV, and it was completely restored to its initial value by a warming/cooling cycle. The γ -radiation induced LC was measured for different HV bias values, source-detector configurations and HV polarities. Measurements with three prototype detectors using different groove passivation procedures were performed. Reducing the size of the passivation layer strongly suppresses the γ -radiation induced LC. The LC increase rate depends on the passivated surface inside and outside the groove, the distance between the source and the passivation layer, and on the electric field in the surrounding LAr volume. The most plausible explanation is that the LC increase is induced by the collection and trapping of charges produced by the ionization of LAr on the detector passivated surface. No γ -radiation induced LC increase was observed with Prototype 3 with + HV, as the detectors will be operated in GERDA. This detector had no passivation layer. Consequently, the enriched diodes were reprocessed without the evaporation of a passivation layer. The results presented here do not explain those reported from the GENIUS-TF experiment, concerning the increase of the LC after long running of bare detectors in LN₂ [35]. We showed that no γ -radiation induced LC is observed in LN₂. Also, no indication of LC caused by surface impurities was observed, as both LN₂ and LAr used for the tests had the same purity level.

Chapter 5

Long-term stability tests with bare detectors in liquid argon

The success of GERDA depends strongly on the long-term stability of germanium detectors operated in liquid argon. Long-term measurements were performed with three prototype detectors using different groove passivation procedures. First, the stability of the detector assembly was investigated with Prototype 1 over a two month period. As a side benefit, the first limit on the neutrinoless double electron capture process of ^{36}Ar was derived. Then, the same detector, mounted with a PTFE/Cu/PTFE disk to protect its passivation layer, was operated continuously during six months. Finally, long-term measurements were carried out with Prototype 2 and Prototype 3 for four and three months, respectively. The results of the long-term stability tests are presented here.

5.1 First stability measurement with Prototype 1

The first long-term stability test of the detector parameters has been carried out in 2006 (Day 240 to 300 in Fig.4.1). The first prototype, with a full passivation layer, was operated in Test Bench 1 filled with liquid argon (LAr). The detector was biased above its operational voltage, at 4000 V. No infrared shield was implemented in the dewar at this time and only a thin copper sheet was mounted on top of the assembly. The detector was operated in the center of the inner vessel with 80 cm long signal cable (Fig.3.2). For this measurement, the cold resistance between the signal and the high voltage (HV) contact (Fig.2.6) was $R_{cold} \approx 8 \text{ k}\Omega$. This is significantly higher than the typical value of $R_{cold} \approx 1 - 2 \text{ k}\Omega$, which indicated that the quality of the contacts was not optimized. The reason was that the HV contact star was bent. It was decided not to warm up and remount the diode. Therefore, the long-term measurement was performed in this configuration, limiting the energy resolution of the detector assembly.

The leakage current (LC) of the detector was monitored once per day with the test point voltage (TPV) of the warm FET preamplifier. As seen in Fig.4.1, the LC was more or less stable at 800 pA. Continuously, spectroscopic measurements with a ^{60}Co source inserted in the test bench and a generator at 1.4 MeV were performed. Spectra were collected in four hour periods. The measurements were interrupted for several hours every five days for the LAr refillings. A ten days long background measurement (without a γ -source) was carried out. Then, the source was reinserted in the set-up. Figure 5.1 shows the energy resolution at the 1.332 MeV ^{60}Co peak and at the 1.4 MeV pulser peak (daily averaged) monitored over the long-term measurement. For the background measurements, the energy

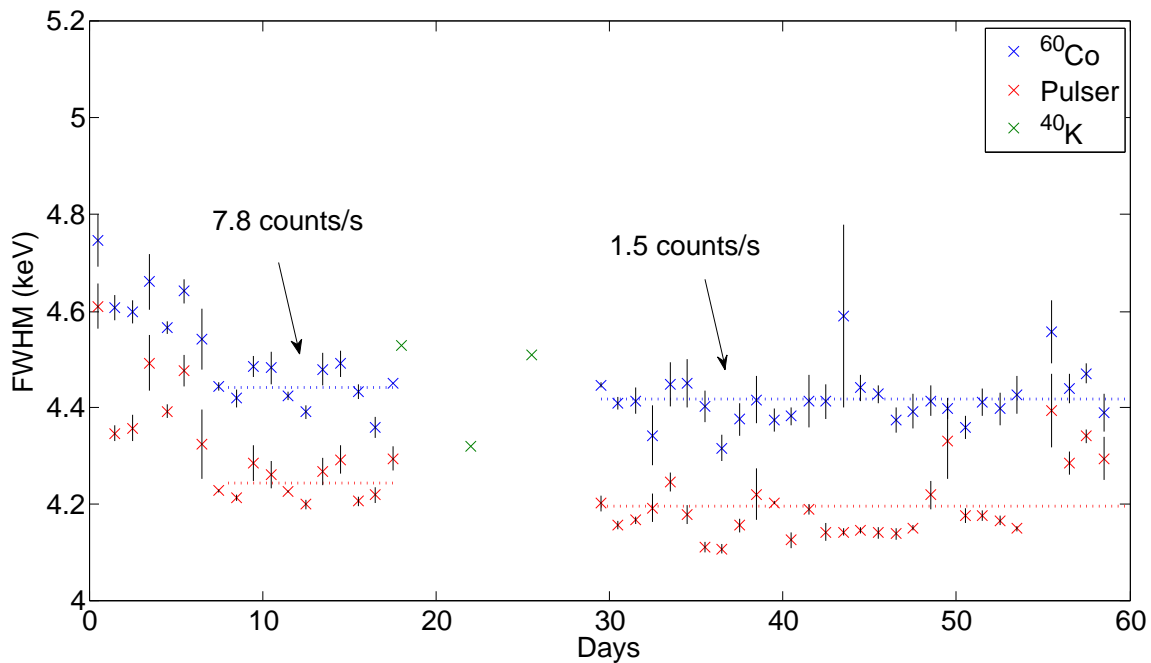


Figure 5.1: Energy resolution (FWHM) of the 1.332 MeV ^{60}Co peak and the 1.4 MeV pulser peak measured during the first long-term stability test with Prototype 1. Four hour spectra were continuously collected and the energy resolutions are averaged per day. The error bars refer to the standard deviation of the mean. For the 10 days background measurement, the resolution of the 1461 keV ^{40}K peak is given. The counting rates under the 1.332 MeV ^{60}Co peak for the first and the second series of measurement are indicated. The horizontal lines show the mean energy resolution, for the first and the second series of measurements, of the ^{60}Co and the pulser peak.

resolution of the ^{40}K peak at 1.461 MeV is given. At the start of the stability test, the energy resolution was worse because the settings of the spectroscopy amplifier (baseline restorer, pole-zero cancellation) were not optimized. The counting rate under the 1.332 MeV ^{60}Co peak during the first series of measurements was 7.8 counts/s. For the second

series of measurements (after the background measurement), the source was not located at the same position. The count rate under the peak became 1.5 counts/s. The energy resolution was slightly improved by reducing the count rate. The count rates were low compared to the count rate with the source in Position 1 or 2 in Fig.3.4 (~ 50 counts/s under the 1.332 MeV ^{60}Co peak). The low count rate and the relatively high LC (~ 800 pA) explain why no γ -radiation induced LC (see Chapter 4) was observed during this stability test. The difference between the resolution of the ^{60}Co and the pulser peak was constant (~ 0.2 keV). One can see that the detector parameters (LC and energy resolution) were stable over this two months period of continuous operation in LAr.

5.1.1 Search for neutrinoless double electron capture of ^{36}Ar

Beyond the original purpose of the long-term stability test, the ten days long background measurement was used to estimate the sensitivity of the present setup to the neutrinoless double electron capture ($0\nu\text{ECEC}$) process of ^{36}Ar . Natural argon contains the isotope ^{36}Ar with an abundance of 0.336%, which is expected to be unstable, undergoing double electron capture (ECEC) [64]. In this process, two atomic electrons are absorbed by the nucleus:



No measurement of the half-life limit is reported. For the $0\nu\text{ECEC}$ process, the momentum-energy conservation requires the released energy Q to be emitted through some additional particle(s). We consider the neutrinoless process in which the released energy ($Q=433.5$ keV) is carried away by three photons: two X-rays with energies of their corresponding holes in the electron shells of the daughter atom produced by the ECEC capture, and one internal bremsstrahlung γ taking the rest of the available energy. The bremsstrahlung γ can be detected by a high resolution germanium detector. The experimental signature is a sharp peak in the area of the Q value of the ECEC reaction, more precisely at 430.8 keV ($E_\gamma = Q - E_K - E_L$ where $E_K=2.47$ keV and $E_L=0.23$ keV are the ^{36}S binding energy for the K and L shells [65]). Figure 5.2 displays the background spectrum and the region of interest around 430 keV measured with Prototype 1. The spectrum around the region of interest is essentially featureless. The lower half-life limit obtained for the $0\nu\text{ECEC}$ process of ^{36}Ar with the emission of a single bremsstrahlung γ is $T_{1/2}(0^+ \rightarrow 0^+ \text{ with three photons}) \geq 1.85 \cdot 10^{18}$ years (68% C.L.). Details of the measurement and the half-life limit calculation are given in [13].

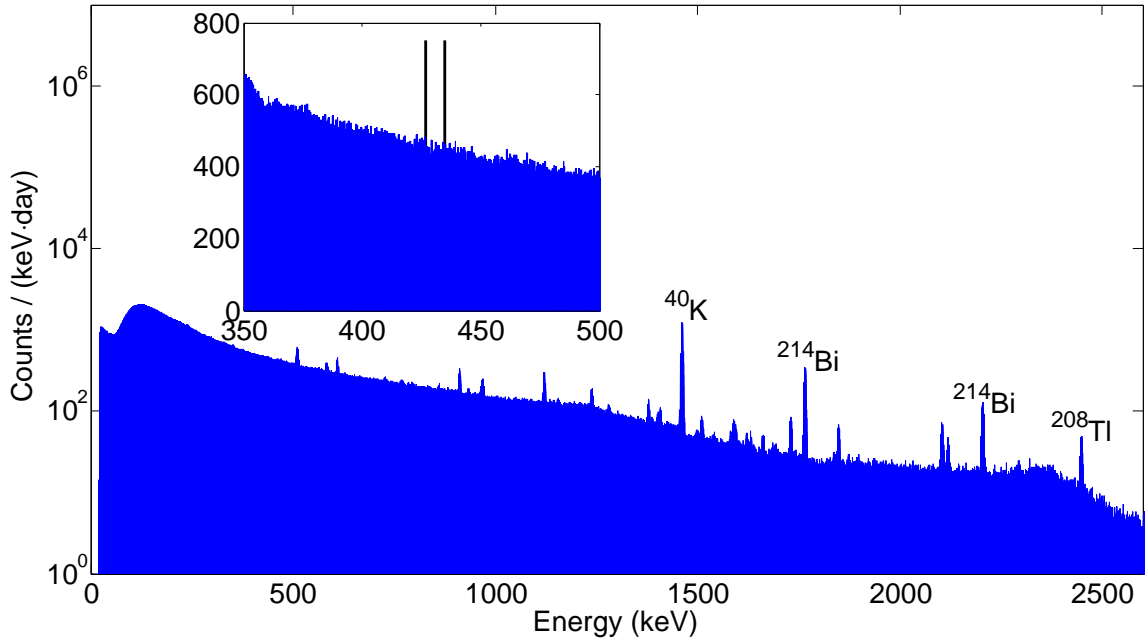


Figure 5.2: The measured background spectrum of a bare HPGe detector operated in liquid argon. A zoom on the region of interest around Q-value of the neutrinoless double electron capture of ^{36}Ar is shown.

5.2 Six month stability measurement with the first prototype in liquid argon

The only detector parameter which can be subjected to change during long-term operation is the LC. The capacitance of a fully depleted detector depends upon its shape and its size, thus it is constant with time. As exposed in Chapter 2, the energy resolution is governed by the variation in the charge carrier production, the variation in the charge carrier collection and the contribution of the electronic noise. The first two contributions are related to the intrinsic properties of the detectors and will not evolve with time assuming constant average energy deposited and bias voltage, and no exposure to strong radiation which can produce trapping centers in the germanium. One component of the electronic parallel noise is due to the detector LC (Eq.3.2). A LC of 1 nA with 6 μs shaping time gives 1.8 keV (FWHM) contribution to the energy resolution, which is clearly measurable. On the contrary, small fluctuations of the LC (~ 10 pA) cannot be detected by monitoring the energy resolution. Therefore, the most sensitive way to monitor the stability of the detector is to measure the LC with high accuracy.

During more than six months, the first prototype detector was continuously operated in LAr in Test Bench 1 (Fig.5.3). The detector was mounted with a PTFE/Cu/PTFE disk covering the passivation layer as an attempt to mitigate the γ -radiation induced LC (Fig.4.5). As usual, the detector was biased at 4000 V. The energy resolution at the beginning of the measurement was 3.5 keV (FWHM) for the 1.332 MeV ^{60}Co peak and 3.0 keV (FWHM) for the pulser peak at 1.4 MeV. Then, the warm preamplifier was disconnected to measure the LC with a high accuracy amperemeter. The LC was monitored every minute and averaged over one hour periods.

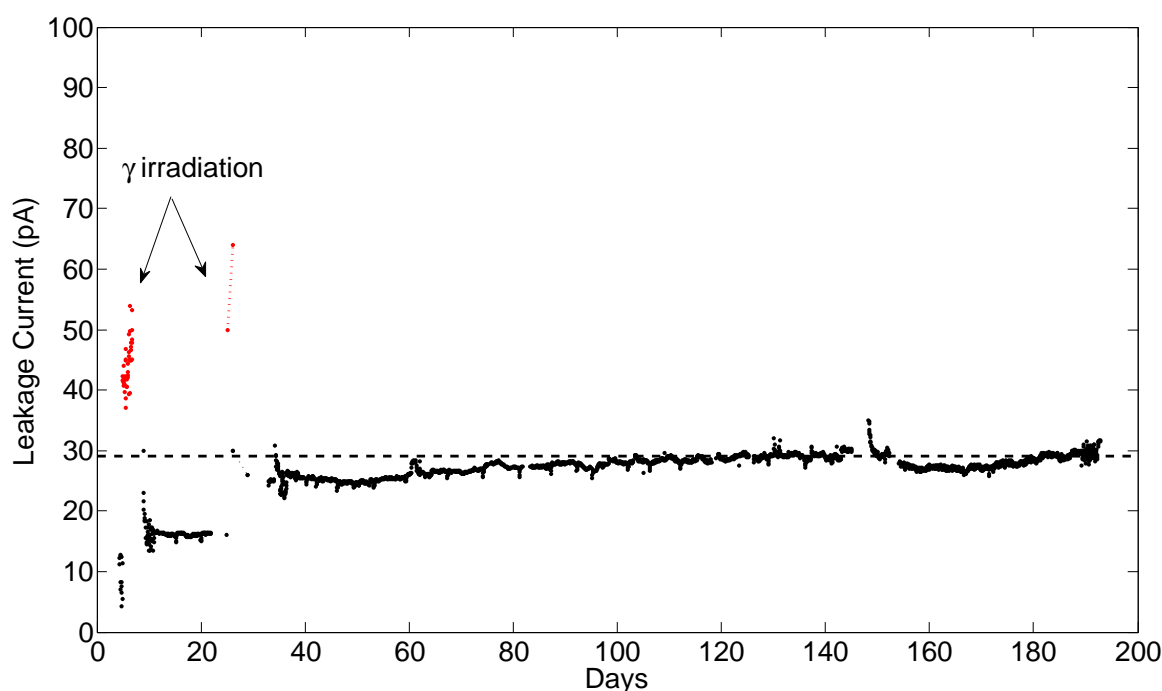


Figure 5.3: Six months of stability test in liquid argon with the first prototype detector mounted with a PTFE/Cu/PTFE disk covering the passivation layer. Within the first month, two γ irradiations were performed. The leakage current uncertainty is ~ 0.5 pA.

Two γ irradiations were performed before the start of the stability test. A small increase of the LC (~ 4 pA) was observed at the beginning of the measurement but, for the following four months, the LC was stable at 30 pA. The small fluctuations of the LC approximately once a week are attributed to the LAr refillings. The PTFE/Cu/PTFE disk is not needed for the Phase-I assembly and was removed after the long-term stability measurement.

5.3 Long-term stability measurements with Prototype 2 and Prototype 3

Long-term stability tests in LAr were also performed with the detector with a reduced passivation layer (Prototype 2) and the detector without passivation layer (Prototype 3). Both detectors were introduced in Chapter 2. The spectroscopic performance of the detector assemblies was not investigated and both detectors were connected to an amperemeter to monitor the LC with high accuracy from the start of the measurements. Figure 5.4 presents the results of the long-term stability tests for the two detectors. Prototype 2 was operated during 4.5 months in Test Bench 1, Prototype 3 during 3 months in Test Bench 2. Both detectors were biased above their operational voltage, at 4000 V. The LC at the start of the measurements were 8 pA and 6 pA for Prototype 2 and 3, respectively. The LAr refillings of the dewars were done once per week. During the refilling process, the LC measurements were stopped as a lot of noise was induced.

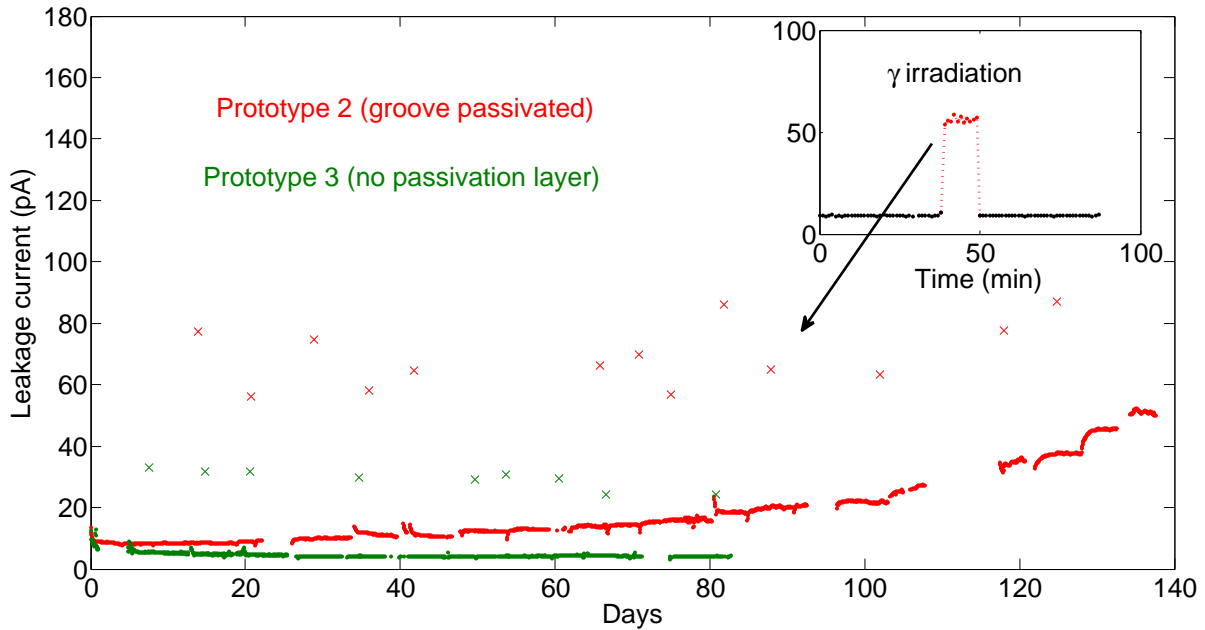


Figure 5.4: Long-term stability measurements in LAr with Prototype 2 and Prototype 3 for 4.5 and 3 months, respectively. The detectors were exposed to a ^{60}Co source once a week during 10 minutes. The increases of the bulk currents when the source was inserted in the test stands are shown (as the points marked "x"). A zoom on one γ irradiation interval is also shown. The LC was monitored every minute and averaged per hour (the uncertainty is ~ 0.5 pA).

To mimic the energy calibrations in GERDA, Prototypes 2 and 3 were exposed to γ -rays once a week during 10 minutes. A ^{60}Co source with an activity of ~ 35 kBq was placed approximately in Position 1 (Fig.3.4), ~ 20 cm away from the detectors (the count rate under the 1.332 MeV peak was ~ 50 counts/s).

During the first month of measurement, the LC of Prototype 2 was stable (< 10 pA). Subsequently, an increase of the LC was measured. At the end of the measurement, the LC was ~ 50 pA. Smaller or no increase of the LC is expected if the detector would have been operated at a lower bias voltage, for example at 3000 V which is its operational voltage.

At the end of the long-term test with Prototype 3, the LC was ~ 4 pA. The detector was perfectly stable during the three months of measurement. This demonstrates that bare detectors can be operated in LAr with excellent long-term stability. The detector manufacturers usually evaporate a passivation layer to prevent surface LC at the edge of the p-n junction. The handling of germanium diodes which have a passivation layer is less delicate. Diodes with a passivation layer are thought to be more resistant to warming/cooling cycles. To investigate the robustness of Prototype 3, extra temperature cycles were carried out after the long-term measurement. In total, five temperature cycles were performed and the detector still had negligible LC (< 10 pA).

5.4 Conclusion

The results presented are crucial for the GERDA experiment. Before our work, the feasibility of a long-term experiment with bare HPGe detectors was questioned. Long-term stability tests of the detector parameters were performed with three prototypes with different groove passivation procedures. For all measurements, the detectors were biased above their operational voltage. A first measurement was carried out with the first prototype detector during two months, with stable LC and energy resolution. From this measurement, the first limit on the 0ν ECEC process of ^{36}Ar was derived. Then, Prototype 1, 2 and 3 were operated in LAr for several months. Their LC, continuously monitored with high accuracy, were at a few tens of pA, similar as measured at the detector manufacturer. During the long-term measurement with Prototype 2, a LC increase of ~ 40 pA was measured, which is still negligible in terms of energy resolution. In the previous chapter, it was shown that γ -radiation induced LC in LAr was observed with bare detectors using a passivation layer. Prototype 3, which has no passivation layer, showed the best performance in LAr and was perfectly stable during the long-term measurement. Consequently, all GERDA Phase-I detectors were reprocessed without the evaporation of a passivation layer.

The results show good long-term stability of naked HPGe detectors and the Genius-TF result [35] is not confirmed. It is meaningful to stress here that Prototype 2 and Prototype 3 were previously operated in the Genius-TF experiment. There, after approximately one year of operation in LN_2 , the detectors could not be operated at their operational voltage because of a too high LC. Without knowing the details of the Genius-TF experiment, it is likely that the good performance of the bare detectors is achieved thanks to our optimized detector handling procedures, mainly the cooling and warming cycles.

Chapter 6

Preparation of the existing HPGe diodes for Phase-I of GERDA

The IGEX detectors were transported from Canfranc Underground Laboratory, Spain, to Laboratori Nazionali del Gran Sasso (LNGS) in November 2005. The Heidelberg-Moscow detectors stayed underground at LNGS since their installation in the experiment between 1990 and 1995. In preparation for GERDA, all detectors were moved to the GERDA underground Detector Laboratory. The first part of this chapter summarizes the operations and measurements which were carried out with the Phase-I enriched detectors prior to their reprocessing at the detector manufacturer. After the characterization of the detectors in their cryostats, the cryostats were opened, the diodes were dismantled from the detector holders, and their dimensions and masses were measured. In addition to the enriched diodes, six low-background natural germanium diodes, previously operated in the Genius-TF experiment, were reprocessed using the same technology. This chapter further presents the dimensions and masses of all diodes, as well as the detector performance parameters, measured after the reprocessing at the detector manufacturer. Finally, details of the total exposure above ground of the diodes and the background index for the cosmogenically produced ^{60}Co and ^{68}Ge are given.

6.1 Characterization of the Phase-I diodes prior to their modifications for GERDA

The Heidelberg-Moscow (HdM) diodes, named ANG 1-5, were produced by EG&G ORTEC, Tennessee, USA, and the IGEX diodes, RG 1-3, by Oxford Inc., Oak Ridge, USA. ANG 1 was reprocessed by Canberra Semiconductor NV, Olen, in 1991. In 2005, all Phase-I enriched detectors were transported to the GERDA Detector Laboratory (GDL) for maintenance and characterization (Fig.6.1).



Figure 6.1: Picture of the five Heidelberg-Moscow and three IGEX enriched detectors in the GERDA underground Detector Laboratory, LNGS.

The characterization of the enriched detectors in GDL before opening the cryostats was performed before the work presented here. Details of the operations and measurements are given in [13]. The detector parameters were restored close to their original values. The energy resolution measured in GDL ranged from 2.3 to 2.9 keV (FWHM) at the 1.332 MeV spectral line of ^{60}Co and the detector leakage current (LC) from 200 pA to 1 nA. Table 6.1 presents the original characteristics of the HdM and IGEX detectors given by the detector manufacturers as well as their performance parameters measured in GDL before the opening of the cryostats.

	ANG 1	ANG 2	ANG 3	ANG 4	ANG 5	RG 1	RG 2	RG 3
Serial number	b 89002	P40239A	P40270A	P40368A	P40496A	28005-S	28006-S	28007-S
Diameter (mm)	58	80	78.5	75	78.8	78	78.7	79.2
Length (mm)	68	108	93.5	100.5	105.7	84.3	84.7	82.5
Hole diam. (mm)	8	8	9	8	8	12.1	n.a.	n.a.
Hole length (mm)	43	94	81.5	88.9	93.5	72.1	n.a.	n.a.
Total mass (g)	980	2905	2447	2400	2781	2150	2194	2121
Dead layer (mm)	0.7	0.7	0.7	0.7	0.7	0.8	0.8	0.5
Enrichment ^{76}Ge (%)	86	87	88	86	86	86	86	86
Operating bias (V)	4000	4000	3500	3000	2500	5000	4000	3800
FWHM (keV)	2.55	1.99	1.99	1.99	2.29	2.16	2.37	2.13
FWHM, GDL (keV)	2.5	2.3	2.9	2.5	2.6	2.2	2.3	2.3
Leakage current, GDL	200 pA	350 pA	1 nA	200 pA	200 pA	200 pA	1 nA	200 pA
Cryostat opening	11.04.06	21.11.06	21.11.06	21.11.06	21.11.06	26.10.06	26.10.06	01.06.06

Table 6.1: Original characteristics of the enriched detectors from the HdM and IGEX experiment given by the detector manufacturers (top rows). The detector parameters (energy resolution and detector leakage current at the operational bias) measured in the GERDA Detector Laboratory before the opening of the cryostats are summarized (bottom rows) [13]. The energy resolution (FWHM) is given for the 1332 keV spectral line of ^{60}Co .

6.1.1 Dimensions and masses of the enriched diodes

All the enriched diodes were dismantled from their cryostats in 2006. Prior to the opening of the cryostats, the diodes were warmed up to room temperature by removing the LN₂ from the dewars and heating the cryostats. The warming up took on average one day and during this time the cryostats were kept under vacuum by continuous pumping. Then, they were brought to normal pressure with nitrogen gas. Afterwards, the cryostats were opened, the detector holders disassembled, and the diodes were taken out. Following the opening, the dimensions and masses of the diodes were measured. The time needed to perform this operation was about one hour. During this time the diodes were exposed to air, however all the operations were performed in the clean room environment of GDL, in a clean bench. At the end, the diodes were stored under vacuum in a transportation container. They were kept underground in GDL until they were transported to Belgium, for the reprocessing. Figure 6.2 presents the sequence of the described operation.



Figure 6.2: Sequence of a diode dismantling and measuring (from top left to bottom right): opening of the cryostat; disassembly of the detector holder; diode taken out from its holder; dimension measurement; mass measurement; storage under vacuum.

Figure 6.3 shows pictures of all Phase-I enriched diodes after their dismounting from the cryostats. ANG 1 was already a Canberra type diode, with a groove and a chinese hat signal contact. RG 2 had a cut out at the edge of the bore-hole side which is 37.1 mm wide and 6.0 mm high. RG 3 has a special shape because a part of the outer portion of the diode near the bore-hole side was removed due to crystallographic defects. ANG 2-5 have their bore-hole side edges chamfered (in their cryostats, the high voltage contacts were made at the chamfered edges). All these features are visible on Fig.6.3.

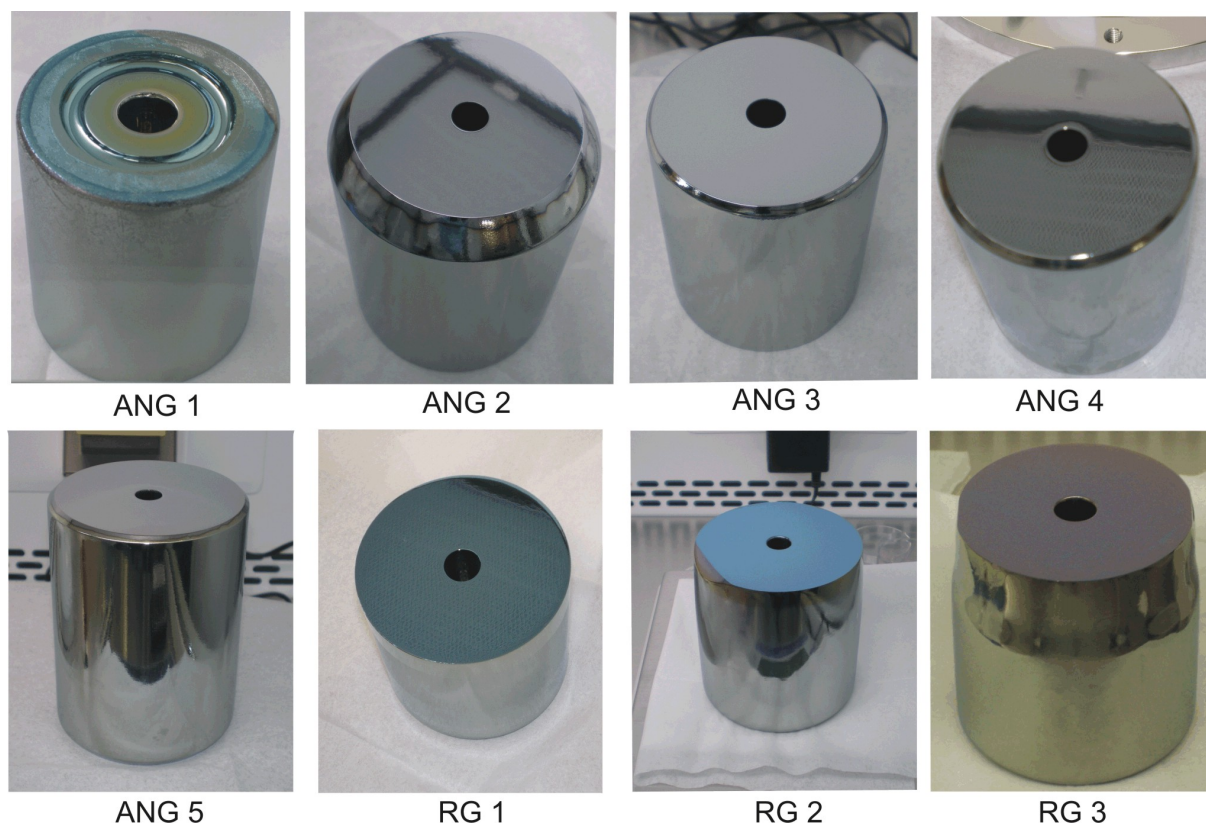


Figure 6.3: Photos of the enriched diodes from the HdM and IGEX experiments taken after their removal from their cryostats in GDL, before their reprocessing for GERDA.

Table 6.2 gives the dimensions and the masses of the diodes measured in GDL before their reprocessing for GERDA. The dimension variables are explained in the drawing in Fig.6.4. The combined mass of the Phase-I enriched diodes was (17944.2 ± 0.3) g. Except for ANG 1 and 2, the total masses measured in GDL are in good agreement with those stated by the detector manufacturers. The difference between the measured mass of ANG 1 in GDL and the mass reported by ORTEC is due to the additional machining of the diode at Canberra Semiconductor NV, Olen, in 1991. The reason for the difference between the ANG 2 mass measured in GDL and the one reported by ORTEC is unknown. Table 6.2 also gives the

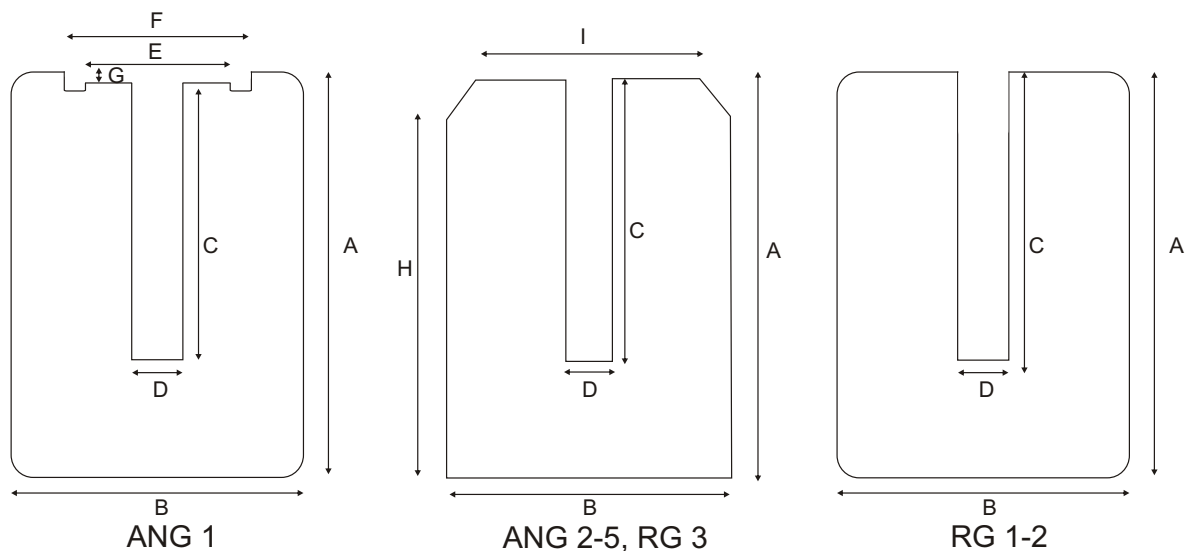


Figure 6.4: Different geometries of the enriched diodes from the experiments HdM and IGEX. The variable H describes the height of the diode until the chamfered edge (for ANG 2-5), alternatively the height until the removed section of the diode (for RG 3).

active masses calculated using the dead layer thicknesses given by the manufacturers and the diode parameters measured in GDL. The combined active mass of the enriched diodes before their reprocessing was (17.16 ± 0.08) kg ($\sim 96\%$ of the total mass). The active masses reported here agree with those in [13].

After dismounting the diodes, the dimensions of the cryostats were measured. The drawing of each cryostat is presented in the Appendix. The cryostats, detector holders and contacts are made of electroformed copper, archeological lead, old ship steel, gold, Teflon, Vespel and Lexan. After measuring their dimensions, the empty cryostats were closed and pumped down to $\sim 10^{-2}$ mbar to prevent their oxidation and deterioration, in order to preserve them for a possible future use. The cryostats and the detector holders are kept underground at LNGS to prevent cosmogenic activation of the materials.

Detector	A (mm)	B (mm)	C (mm)	D (mm)	E (mm)	F (mm)	G (mm)	H (mm)	I (mm)	Total mass (g)	Active mass (g)	Active mass (%)
ANG 1	68.0	58.3	51	12	39	30	3			968.7	914±9	94±1
ANG 2	107.4	79.3	93	10			96.7	64.5		2878.3	2765±18	96±1
ANG 3	93.3	78.1	81	11			91.1	72.6		2446.5	2344±20	96±1
ANG 4	100.3	75.0	88	11			98.5	69.9		2401.2	2296±17	95±1
ANG 5	105.5	78.3	93	10			102.1	73.3		2782.1	2666±20	96±1
RG 1	84.0	77.9	32	12						2152.3	2043±46	95±2
RG 2	84.5	78.5	74	10						2194.2	2083±41	95±2
RG 3	82.6	79.8	77	12			58.2	74.9		2120.9	2051±39	97 ±2

Table 6.2: Dimensions and masses of the HdM and IGEX enriched diodes measured in GDL after the opening of the cryostats. The dimension variables are explained in Fig.6.4. The accuracy of the diode diameter and length is ± 0.1 mm. The bore-hole dimensions of all diodes and the groove of ANG 1 were measured without touching the diode surface with an accuracy of ± 1 mm. The error in the masses measured in GDL is 0.1 gram. The active mass was calculated using the diode dimensions measured in GDL and the dead layer given by the detector manufacturer in grams and as a percentage of the total mass. The density of the enriched germanium is 5.54 g/cm^3 . The uncertainty on the dead layer is taken as 10% [13]. The difference between the measured mass and the mass calculated using the diode dimensions is taken as an additional systematic error for the active mass.

6.1.2 Natural germanium diodes from GENIUS-TF

In addition to the enriched diodes, six low-background natural HPGe diodes, previously operated in the Genius-TF experiment, will be redeployed for GERDA. The diodes were ORTEC type, originally from PerkinElmer instruments [39], produced in 1991. Table 6.3 gives the serial numbers of the detectors, their operational voltages and their energy resolutions given by the detector manufacturer. Two of them (GTF 42 and GTF 44) were introduced in earlier chapters, referred to as Prototype 2 and Prototype 3.

Detector	Serial number	HV (V)	FWHM (keV)
GTF 32	P41032A	3200	1.8
GTF 42	P41042A	2000	2.4
GTF 44	P41044A	2600	3.1
GTF 45	P41045A	3000	2.0
GTF 110	P41110A	3500	2.1
GTF 112	P41112A	2500	2.0

Table 6.3: Characteristics of the detectors from the Genius-TF experiment before their reprocessing: name, serial number, operational voltage and energy resolution given by the detector manufacturer. The energy resolution (FWHM) is given for the 1.332 MeV ^{60}Co spectral line.

6.2 Reprocessing of the Phase-I diodes at the detector manufacturer

In preparation for GERDA, the enriched diodes were reprocessed at Canberra Semiconductor, Olen [38], in the period from 2006 to 2008. Following the tests with the bare prototype detectors in liquid argon (LAr) which showed γ -radiation induced LC increase for detectors with a passivation layer (see Chapter 4), the diodes were reprocessed without the evaporation of a passivation layer. Apart from that, the reprocessing was performed according to the standard manufacturer technology. The detector manufacturer first proceeded to the machining of the groove, the bore hole and the diode outer surface (few μm from the old lithium layer were removed from the surface opposite to the bore hole and the edges of the top and the bottom surface were rounded off). Then, the n+ conductive layer was remade by lithium drifting. Next, a new boron implantation was done at the p+ contact. At the end, the groove was chemically etched.

ANG 1 and RG 3 were first reprocessed in 2006, when the testing with prototype detectors was ongoing. At this time, the effect of γ -radiation on the LC of bare detectors with a passivation layer operated in LAr was unknown. Therefore, their reprocessing included the evaporation of a passivation layer. Their passivation layer covered the groove and extended to the inner and the outer surface on the bore-hole side (same geometry as with Prototype 1). In the first round of their tests during Phase-I detector performance characterization in LAr (described in the next chapter), they were operated in this configuration. Both diodes were then returned to the detector manufacturer and their passivation layers were removed. Now all Phase-I detectors (except of GTF 42 which has a reduced passivation layer covering only the groove) have no passivation layer. ANG 3 was also reprocessed twice because it showed a high LC in the LAr test bench of GDL.

Inbetween the various reprocessing operations, the diodes were stored under vacuum in their transportation containers in the HADES (High Activity Disposal Experimental Site) facility, Mol, Belgium. HADES is located at a depth of 223 m (500 meters water equivalent), 15 km away from the detector manufacturer.

6.2.1 Dimensions and masses of the diodes after reprocessing

Figure 6.5 shows the geometries of the Phase-I diodes after their reprocessing. Only RG 3 has a geometry different than the other diodes (smaller diameter near the bore hole side) and RG 2 still has the cut out at the edge of the bore hole side. Table 6.4 gives the dimensions and the masses of the enriched and non-enriched diodes, measured at the detector manufacturer after their reprocessing. The combined mass of the Phase-I enriched and non-enriched diodes is 17663 g and 15596 g, respectively. In average, the difference between the detector mass before and after the reprocessing is ~ 40 g.

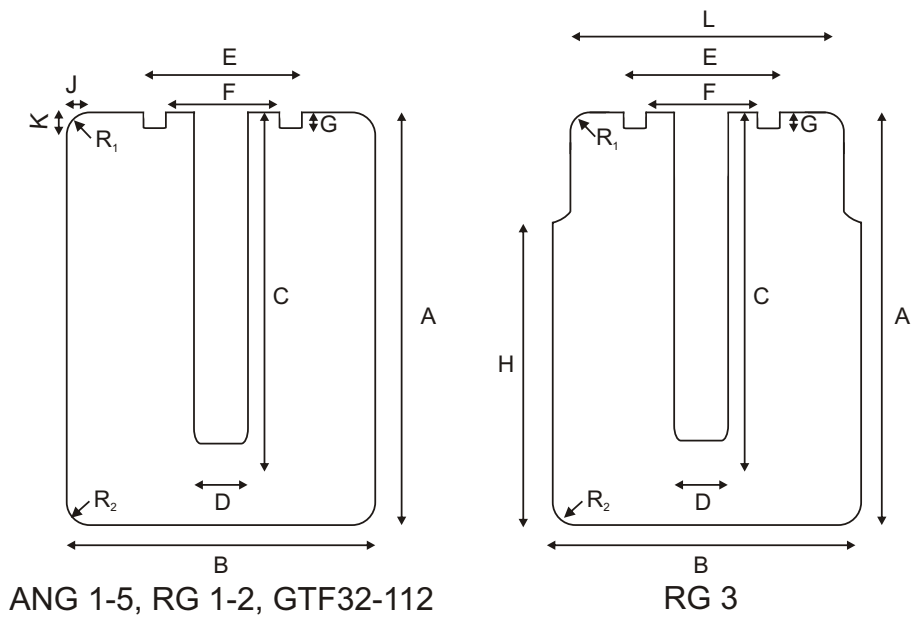


Figure 6.5: Geometries of the Phase-I diodes after their reprocessing.

Detector	Serial number	A	B	C	D	E	F	G	H	J	K	L	R ₁	R ₂	Mass (g) before	Mass (g) after	Δ Mass (g)
ANG 1	b 89002	68	58.5	51	13.5	39	26	4					2	1	969	958	11
ANG 2	00472	107	80	94	14	36	30	2	8	11				1-2	2878	2833	45
ANG 3	00474	93	78	83	15	40	34	2					3	1-2	2446	2391	55
ANG 4	00471	100	75	89	14	36	30	2					3	3	2401	2372	29
ANG 5	00473	105	78.5	94	12.5	36	30	2					3	5	2782	2746	36
RG 1	00468	84	77.5	73	13.5	40	34	2					1-2	5	2152	2110	42
RG 2	00467	84	77.5	72	13	40	34	2					1-2	5	2194	2166	28
RG 3	00457	81	79	71	13	32	26	2.5	61			74.9	2	5	2121	2087	34
GTF 32	00460	71	89	41.5	12	40	30	2					1-2	1-2		2321	
GTF 42	00461	82.5	85	42.5	11.5	40	30	2					1-2	1-2		2467	
GTF 44	00469	84	84	46	12	40	34	2					1-2	1-2		2465	
GTF 45	00463	75	87	43	11.5	40	30	2					1-2	1-2		2332	
GTF 110	00470	105	84	69	11.5	40	34	2					1-2	1-2		3046	
GTF 112	00462	100	85	63	11.5	40	34	2					1-2	1-2		2965	

Table 6.4: Physical characteristics of the Phase-I diodes measured at the detector manufacturer after their reprocessing for GERDA: Canberra serial number, dimensions (mm), total mass (g) before and after the reprocessing. The dimension variables are explained in Fig.6.5. The masses of the GTF detectors before the reprocessing are not available.

6.2.2 Characterization of the detectors at the manufacturer site after the reprocessing

After their reprocessing, the performance parameters of the detectors were measured at the manufacturer site. They were mounted in a test support and submerged in LN₂. The LC and the capacitance of the detectors were measured as the high voltage (HV) was applied. The LC was measured with an amperemeter (accuracy ~ 10 pA) and the capacitance with a capacitance meter connected in parallel with the detector (accuracy ~ 2 pF). No spectroscopic measurement was performed with the Phase-I detectors at the manufacturer. Figures 6.6, 6.7 and 6.8 present the LC and the capacitance in function of HV for ANG, RG and GTF detectors, respectively.

The full depletion voltage (voltage above which the capacitance is constant) of the detectors can be identified from these curves. The capacitance of the detectors, at their full depletion, ranged between 20 and 50 pF. At their operational voltages given by the original manufacturers, all detectors have $LC < 100$ pA (except RG 3 which has $LC \approx 500$ pA at 4000 V). For ANG 1 and RG 3, both I-V curves before and after the removal of the passivation layer are shown, and no significant difference can be observed.

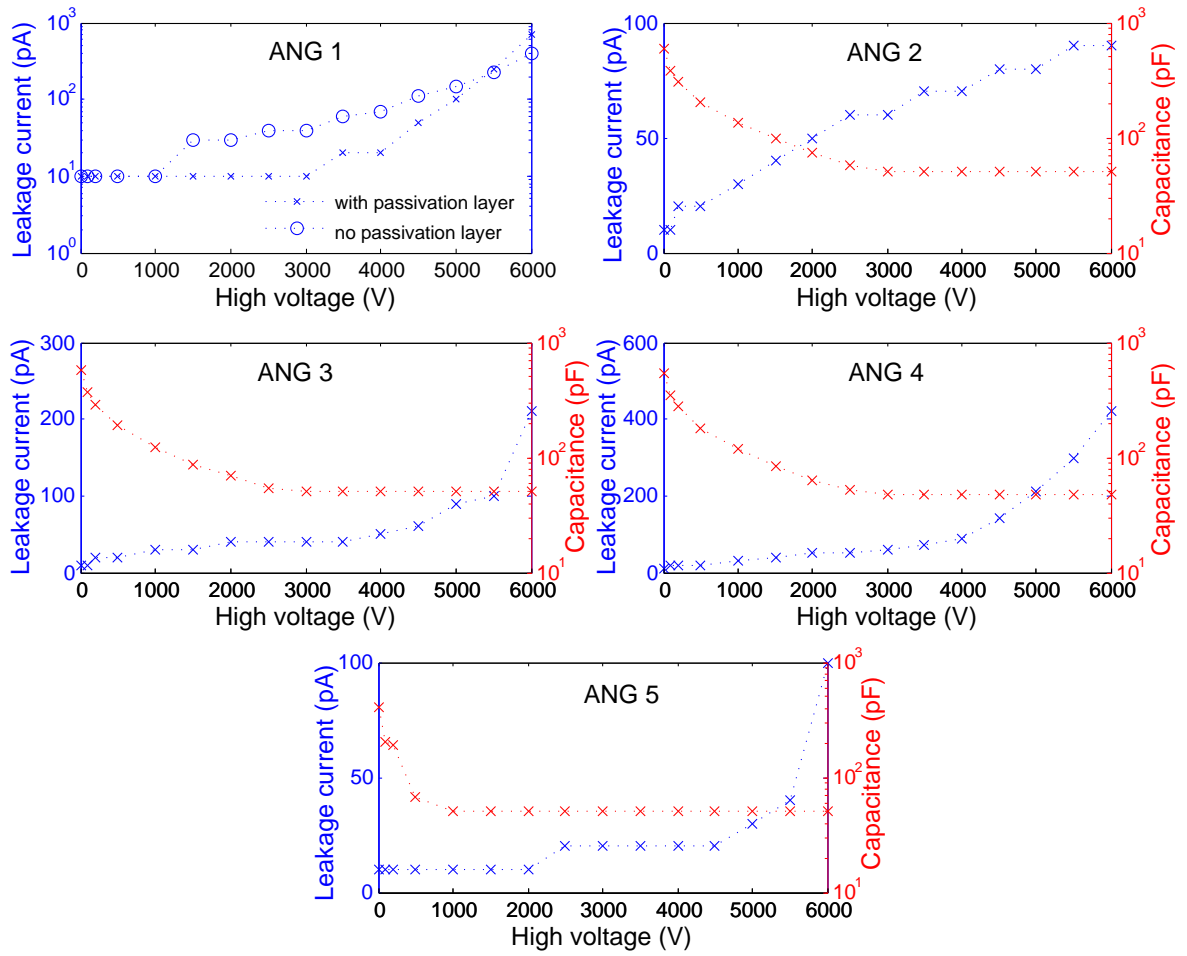


Figure 6.6: Characterization (leakage current and capacitance) of ANG detectors measured at the manufacturer site after their reprocessing. The uncertainty on the leakage current is ~ 10 pA and on the capacitance is ~ 2 pF. The capacitance measurement of ANG 1 was not performed.

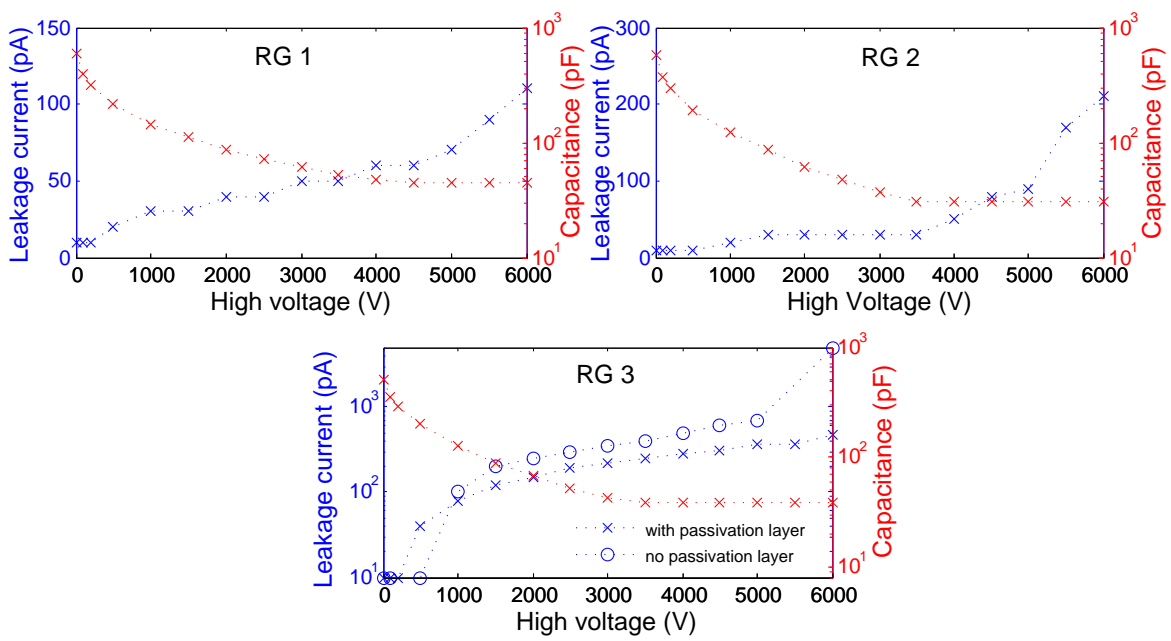


Figure 6.7: Characterization (leakage current and capacitance) of RG detectors measured at the manufacturer site after their reprocessing. The uncertainty on the leakage current is ~ 10 pA and on the capacitance is ~ 2 pF.

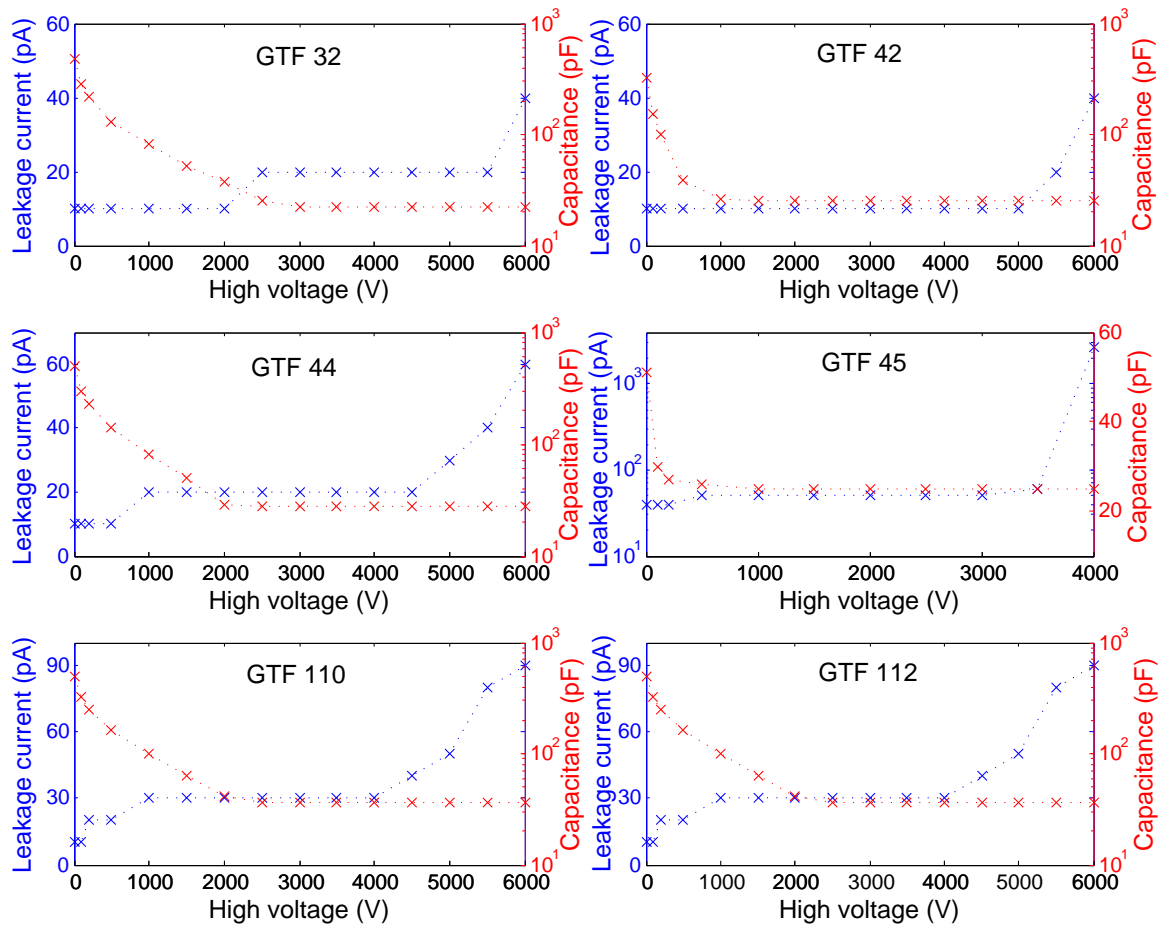


Figure 6.8: Characterization (leakage current and capacitance) of GTF detectors measured at the manufacturer site after their reprocessing. The uncertainty on the leakage current is ~ 10 pA and on the capacitance is ~ 2 pF.

6.3 Internal background of the enriched diodes from cosmogenic ^{60}Co and ^{68}Ge production

As mentioned in Chapter 2, if the diodes are above ground the germanium is exposed to radiation from cosmic rays. One of the most important cosmogenic processes is the spallation of nuclei by high energy neutrons. It causes the production of numerous radionuclides. The most dangerous for the $0\nu\beta\beta$ decay are ^{68}Ge and ^{60}Co since Q values above $Q_{\beta\beta} = 2039$ keV occur in their decay chains, and their lifetimes are in the range of years. The β -decay of ^{60}Co can produce background at the $Q_{\beta\beta}$ via the summation of its two γ -rays ($Q = 2.5$ MeV). The ^{68}Ge decays via electron capture into ^{68}Ga , which can deposit energy around the $Q_{\beta\beta}$ through β^+ decay with $Q = 2.9$ MeV.

The amount of ^{60}Co nuclei produced in germanium is determined by the time spent above ground after the zone refinement process. For the production of ^{68}Ge , the relevant time is between the isotope separation (enrichment) and the storage underground. The cosmogenic production rate of ^{60}Co and ^{68}Ge , in germanium isotopically enriched to 86% in ^{76}Ge , at sea level is about 4 atoms/(kg·d) and 1 atom/(kg·d), respectively [21]. The half-life of ^{60}Co is 5.3 years and the half-life of ^{68}Ge is 271 days. The activity A (decay/(kg·y)) at a time t after the exposure above ground is

$$A = N \cdot \lambda \cdot e^{-\lambda t}, \quad (6.1)$$

where N is the number of isotopes produced per kg and λ the decay constant. The energy deposited in the detector from ^{60}Co and ^{68}Ge decays located inside the diode was simulated and reported in [21]. For ^{60}Co , one out of 6000 decays deposits energy within a 1 keV bin at $Q_{\beta\beta}$, thus the background index is $B = A/(6000 \cdot \text{keV})$. Similarly, in about one out of 5000 decays of ^{68}Ge the energy deposited is at $Q_{\beta\beta}$ within a 1 keV bin ($B = A/(5000 \cdot \text{keV})$).

The production of ^{60}Co and ^{68}Ge nuclei in the enriched diodes when exposed above ground was calculated for the periods before and after the reprocessing. The corresponding activities and background contribution in the region of interest at $Q_{\beta\beta}$ were determined for the reference date of July 2009. Tables 6.5 and 6.6 summarize the exposure above ground of the Phase-I enriched diodes. The total background index from ^{60}Co and ^{68}Ge production above ground in the Phase-I diodes is in the range of $(0.9 - 2.9) \cdot 10^{-3}$ cts/(keV·kg·y).

	Date	Exp. days	A ($\mu\text{Bq/kg}$)		B (cts/keV \cdot kg \cdot y)	
			^{60}Co	^{68}Ge	^{60}Co	^{68}Ge
ANG 1			($\times 10^{-3}$)			
Crystal grown/installed LNGS	04.90/01.91	233 *	0.34	10^{-7} **	1.79	10^{-6}
Transport LNGS-HADES (1 st)	22.08.06	1.1	0.01	0.002	0.06	0.01
— " — (2 nd)	05.09.08	0.8	0.01	0.011	0.07	0.07
Reprocessing (1 st)	25.08.06	2.0	0.02	0.004	0.12	0.03
— " — (2 nd)	22.10.08	0.3	0.01	0.005	0.03	0.03
Transport HADES-LNGS (1 st)	26.08.06	1.0	0.01	0.002	0.06	0.01
— " — (2 nd)	27.10.08	0.9	0.01	0.015	0.06	0.09
Total					2.2	0.2
ANG 2			($\times 10^{-3}$)			
Crystal grown/installed LNGS	02.91/09.91	105	0.17	10^{-6} **	0.88	10^{-6}
Transport LNGS-HADES	30.11.06	1.1	0.01	0.003	0.06	0.02
Reprocessing	26.06.08	2.5	0.03	0.028	0.19	0.18
Transport HADES-LNGS	11.07.08	0.9	0.01	0.011	0.07	0.07
Total					1.2	0.3
ANG 3			($\times 10^{-3}$)			
Crystal grown/installed LNGS	03.91/08.92	30	0.01	10^{-6} **	0.28	10^{-5}
Transport LNGS-HADES (1 st)	30.11.06	1.1	0.01	0.003	0.06	0.02
— " — (2 nd)	05.09.08	0.8	0.01	0.011	0.06	0.07
Reprocessing (1 st)	26.06.08	2.2	0.03	0.025	0.11	0.16
— " — (2 nd)	22.10.08	0.3	0.01	0.005	0.03	0.03
Transport HADES-LNGS (1 st)	11.10.08	0.9	0.01	0.011	0.07	0.09
— " — (2 nd)	27.10.08	0.9	0.01	0.015	0.07	0.09
Total					1.9	0.5
ANG 4			($\times 10^{-3}$)			
Crystal grown/installed LNGS	11.93/01.95	56	0.14	10^{-5} **	0.73	10^{-4}
Transport LNGS-HADES	23.11.06	1.0	0.01	0.003	0.06	0.02
Reprocessing	25.06.08	2.2	0.03	0.025	0.17	0.15
Transport HADES-LNGS	06.08.08	0.9	0.01	0.012	0.07	0.08
Total					1.0	0.3
ANG 5			($\times 10^{-3}$)			
Crystal grown/installed LNGS	10.93/12.94	49	0.12	10^{-5} **	0.65	10^{-4}
Transport LNGS-HADES	30.11.06	1.0	0.01	0.003	0.06	0.02
Reprocessing	19.06.08	2.2	0.03	0.024	0.17	0.15
Transport HADES-LNGS	06.08.08	0.9	0.01	0.012	0.07	0.08
Total					1.0	0.3

Table 6.5: Exposure above ground of the ANG diodes. For the reprocessing, the given dates refer to the last day of work, and the days above ground are the cumulative time for the whole process. ANG 1 and ANG 3 were reprocessed twice. The activities A and the background index B are calculated for the reference date of July 2009. The data before the reprocessing come from [66, 67, 68, 69, 70, 71]. * ANG 1 was transported by plane from USA to Germany. A one day flight, corresponding to approximately 100 days exposure on earth surface [72], is assumed. ** The saturation concentration is assumed when the detector was brought underground.

	Date	Exp. days	A ($\mu\text{Bq/kg}$)		B (cts/keV \cdot kg \cdot y)	
			^{60}Co	^{68}Ge	^{60}Co	^{68}Ge
RG 1			($\times 10^{-3}$)			
Crystal grown/installed Homestake	09.93/11.93	45	0.10	10^{-5} *	0.50	10^{-5}
From Homestake/to Canfranc	06.97/07.97	30	0.10	10^{-5}	0.55	10^{-4}
Transport Canfranc-LNGS	18.11.05	0.8	0.01	0.001	0.04	0.01
Transport LNGS-HADES	23.11.06	1.0	0.01	0.003	0.06	0.02
Reprocessing	26.06.08	1.6	0.02	0.019	0.13	0.12
Transport HADES-LNGS	11.07.08	0.9	0.01	0.011	0.07	0.07
Total					1.4	0.2
RG 2			($\times 10^{-3}$)			
Crystal grown/installed Homestake	02.94/05.94	95	0.22	10^{-5} *	1.14	10^{-4}
From Homestake/to Canfranc	12.96/01.97	29	0.09	10^{-5}	0.50	10^{-5}
Transport Canfranc-LNGS	18.11.05	0.8	0.01	0.001	0.04	0.01
Transport LNGS-HADES	23.11.06	1.0	0.01	0.003	0.06	0.02
Reprocessing	25.06.08	1.4	0.02	0.016	0.11	0.10
Transport HADES-LNGS	06.08.08	0.9	0.01	0.012	0.07	0.08
Total					1.9	0.2
RG 3			($\times 10^{-3}$)			
Crystal grown/installed Canfranc	12.94/05.95	160	0.42	10^{-5} *	2.18	10^{-4}
Transport Canfranc-LNGS	18.11.05	0.8	0.01	0.001	0.04	0.01
Transport LNGS-HADES (1 st)	22.08.06	1.1	0.01	0.002	0.07	0.01
— " — (2 nd)	05.09.08	1.0	0.01	0.012	0.07	0.07
Reprocessing (1 st)	12.09.06	0.7	0.01	0.001	0.04	0.01
— " — (2 nd)	23.10.08	0.8	0.01	0.010	0.05	0.06
Transport HADES-LNGS (1 st)	21.11.06	1.0	0.01	0.003	0.06	0.02
— " — (2 nd)	27.10.08	0.9	0.01	0.015	0.07	0.09
Total					2.6	0.3

Table 6.6: Exposure above ground of the RG diodes. For the reprocessing, the given dates refer to the last day of work, and the days above ground are the cumulative time for the whole process. RG 3 was reprocessed twice. The activities A and the background index B are calculated for the reference date of July 2009. The data before the reprocessing come from [73]. * The saturation concentration is assumed when the detector was brought underground.

The main contribution to the background index comes from the ^{60}Co produced before the installation of the enriched detectors underground, for the HdM and the IGEX experiment. For the production of ^{68}Ge before the start of the HdM and IGEX experiment, the saturation concentration (400 atoms/kg) is assumed at the time when the detectors were brought underground for the experiments. This background is negligible in July 2009 ($B < 10^{-6}$ cts/(keV·kg·y)).

For the reprocessing, the exposure of the detectors to cosmic rays was minimized by storing the diodes in HADES inbetween the various reprocessing operations. The typical exposure during the reprocessing of the Phase-I diodes, including the transportation from LNGS to HADES and back, was ~ 5 days, which gives a relatively small contribution to the background index: $B = (0.4 - 0.6) \cdot 10^{-3}$ cts/(keV·kg·y). Both the ^{60}Co and ^{68}Ge production during the reprocessing contribute approximately equally to the background index calculated for the reference date of July 2009.

6.4 Conclusion

In preparation for GERDA, the Phase-I enriched and non-enriched diodes were reprocessed at Canberra SemiConductor NV, Olen. Before their reprocessing, the enriched diodes were dismantled from their cryostats in the clean room environment of GDL, their dimensions and masses were measured and the diodes were stored under vacuum in a transportation container. Then, the diodes were transported to the detector manufacturer. In between the various reprocessing steps, the diodes were stored underground in HADES. The diodes were reprocessed according to the standard p-type HPGe technology from the manufacturer. However, the evaporation of a passivation layer was omitted. After the reprocessing, the detector parameters (leakage current and capacitance) were measured in LN_2 . All detectors showed good performance. The combined mass of the Phase-I enriched diodes is 17.7 kg, which is ~ 300 g less than before the reprocessing. A summary of the enriched diode exposure above ground was presented for the period before and after their installation underground for the HdM or IGEX experiment. For the reprocessing, the exposure above ground was minimized. The typical exposure, including the transportation from LNGS to HADES and back, is ~ 5 days. The cosmogenic production of ^{60}Co and ^{68}Ge and their corresponding background index in July 2009 were calculated ($B \approx 2 \cdot 10^{-3}$ cts/(keV·kg·y)). The main contribution comes from the production of ^{60}Co before the installation of the detectors underground for HdM and IGEX. After their characterization at the detector manufacturer site, the diodes were transported back to GDL, where their testing resumed. The following tests are summarized in the next chapter.

Chapter 7

Characterization of the Phase-I detectors in liquid argon

After their reprocessing and before their operation in GERDA, the enriched and non-enriched Phase-I detectors were operated in the liquid argon test bench of the GERDA Detector Laboratory. In total, 12 detectors (8 enriched, 4 natural germanium) were tested in the period from July to November 2008. The goal was to mount the diodes in their final low-mass holders and to measure their performance parameters in liquid argon. The leakage current, counting characteristics and energy resolution of the detectors were measured in function of the applied voltage. In addition, detection efficiency measurements were performed and the results compared to Monte Carlo simulations to determine the active masses of the detectors. This chapter summarizes the operations and measurements performed with the Phase-I detectors in the GERDA Detector Laboratory after their reprocessing.

7.1 Mounting of the diodes in their low-mass holders

A low-mass holder was constructed at Max-Planck-Institut für Kernphysik for each of the Phase-I diodes according to its dimensions. The technical drawings of the detector holders are presented in the Appendix. The diodes were mounted in their low-mass holders under nitrogen atmosphere, in the radon-reduced bench, following the procedure described in Chapter 3. None of the enriched diodes was exposed to the normal air of the laboratory. The enriched diodes were mounted with a silicon spring for the signal contact, and with a copper screw for the high voltage (HV) contact (by opposition to the prototypes mounted with stainless steel springs and stainless steel screws). The problem sometimes encountered with the copper screws was the damage of the threads, when applying a torque of ~ 60 N·cm, due to the softness of copper. However, all enriched detectors, except ANG 1 and

RG 3 which use a stainless steel screw, were mounted with a copper screw. New screws made out of a low-background copper-silicon-nickel alloy are prepared to exchange the stainless steel screws.

The surface of the diodes was polished at the HV contact point with diamond abrasive paper to remove the germanium oxide (Fig.7.1). The abrasive paper, from 3M Deutschland GmbH [74], had a granularity of $9\ \mu\text{m}$ and its measured radon emanation was $<18.2\ \mu\text{Bq/g}$ in saturation. The quality of the HV and the signal contact was measured right after the mounting with a multimeter when the assembly was warm and remeasured after the cooling down with a mA current source¹ (Fig.2.6). The warm electrical resistances measured ranged between 30 and 70 Ω and the cold resistances between 1.2 and 3.7 k Ω (Table 7.2, section 7.2.3).

Figure 7.2 shows a mock-up assembly attached to the top of the infrared shield. Copper stripes connect the signal and the HV contact to a cable just below the infrared shield lid. The signal and the HV stripe is inserted in a PTFE isolating tube. Apart from replacing the stainless steel screws, the Phase-I diodes will not be dismantled from their support before their operation in GERDA. At the time of the measurements, the exact lengths of

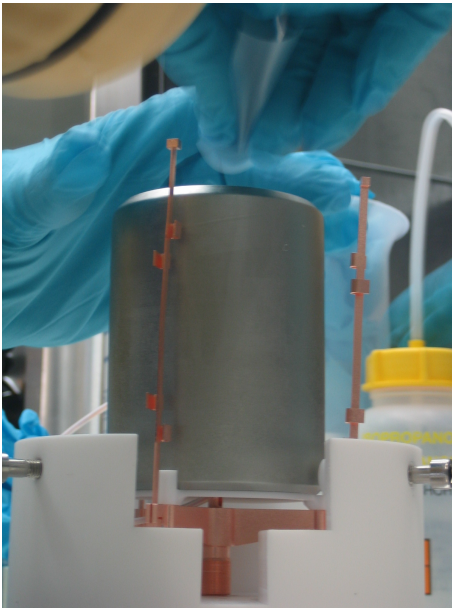


Figure 7.1: Polishing of the diode surface in the radon-reduced bench before mounting the high voltage contact.

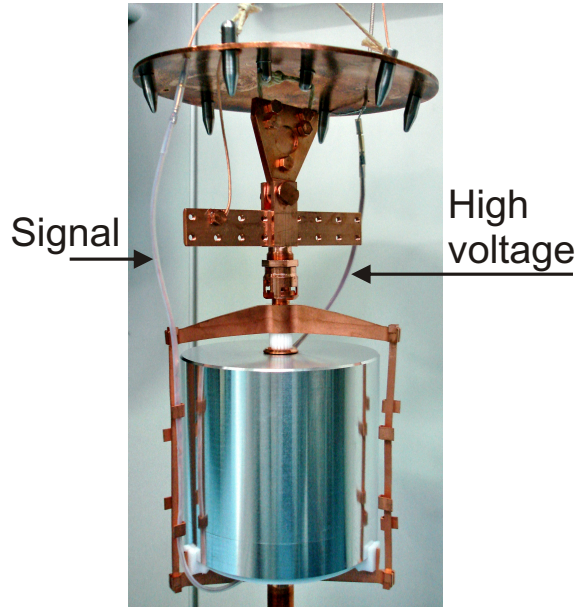


Figure 7.2: Mock-up assembly attached to the top of the infrared shield. The signal and high voltage copper stripe is indicated.

¹The cold resistance measurement includes the protective diode resistance of the first stage preamplifier mounted in the neck of the dewar

the necessary copper stripes in the final experiment were unknown. Therefore, the contact pins between the stripes and the cables were soldered as far as possible from the detectors, below the infrared shield. To reach the aimed background in GERDA, the pins and the cables will be located further away from the assembly (the copper stripes are much more radiopure than the cable). In that case, the copper stripes will be cut before the contact pins and elongated by clamping with longer copper stripes, avoiding to dismount and remount again the diodes.

7.2 Investigation of the detector performance

The Phase-I detectors were operated in the liquid argon (LAr) test bench which is connected to the radon-reduced clean bench (Test Bench 1). To prevent contamination of the diodes, the dewar was emptied, flushed for several days with N₂ and refilled with LAr before operating the enriched detectors. As described in Chapter 3, the characterization of the Phase-I detectors was performed using a first stage preamplifier mounted in the neck of the inner vessel and operated in Ar gas (Fig.3.11). The signal cable length connecting the detector to the first stage preamplifier was ~ 60 cm (including the copper stripe).

Prototype 1 was first operated in this configuration and an energy resolution of 2.6 keV (FWHM) at 1.332 MeV was obtained. Then, all enriched detectors and three of the GTF detectors (GTF 32, 42 and 44) were tested. Prototype 1, GTF 42 (Prototype 2) and GTF 44 (Prototype 3) were introduced in Chapter 2. The enriched detectors were operated only for one or two days in the test bench to prevent their contamination as the setup was not designed for ultra low-background measurements and the radon content in the inner vessel was unknown. The performance parameters of the detectors (leakage current, counting characteristics and energy resolution) were measured as a function of HV. After first tests, ANG 1 and RG 3, which had a full passivation layer, were transported to the detector manufacturer. After the removal of their passivation layer, their testing in GDL was resumed.

7.2.1 Current-Voltage curve measurements

The leakage current (LC) was measured with the test point voltage (TPV) of the preamplifier. For some detectors (ANG 3-5, RG 3), the operational voltage could not be reached at the first cooling down because of a high LC. In these cases, additional warming/cooling cycles were performed to reduce the LC. Tests with the prototype detectors showed that a temperature cycle was very efficient to restore the LC of the detectors. The reason is

unclear, however it is thought that the methanol chemically reacts with the germanium resulting in some form of surface passivation. Figure 7.3, 7.4 and 7.5 present the current-voltage (I-V) curves measured in the LAr test bench with the ANG detectors, the RG detectors and the non-enriched detectors (GTF and Prototype 1), respectively.

The I-V curves of ANG 1 were similar before and after the removal of its passivation layer. Its LC was satisfying (300 pA at 4000 V) even though it was higher than the LC measured at the detector manufacturer (20 pA). The operational voltage of RG 3 was not reached, because of high LC, when the detector had a passivation layer. Previous tests showed that high LC (on the order of nA) of detectors with a passivation layer cannot be totally restored by warming cycle. Therefore, no additional temperature cycle was performed with ANG 1 and RG 3 with a full passivation layer.

On the contrary, additional warming/cooling cycles were performed with ANG 3, 4 and 5, which also initially showed a high LC. The LC of ANG 4 and ANG 5 was restored to the value measured at the detector manufacturer. After two additional temperature cycles with ANG 3, the operational voltage (3500 V) was reached. However, the LC was still higher (~ 600 pA) than measured at the detector manufacturer (40 pA). The diode was once again transported to the detector manufacturer. No I-V curve was measured in GDL after its second reprocessing. The LC of RG 3 was too high to reach the operational bias (3800 V) at the first cooling after the removal of its passivation layer. Three more temperature cycles were carried out and the operational voltage was reached. However, the LC was ~ 2 nA, as compared to $LC \approx 500$ pA at the detector manufacturer.

Finally, the LC of the majority of the detectors was at the level as measured at the detector manufacturer after their reprocessing (Fig.6.6, 6.7 and 6.8). For most of the enriched detectors, smaller LC was measured in the LAr test bench after their reprocessing than in their cryostats before the reprocessing.

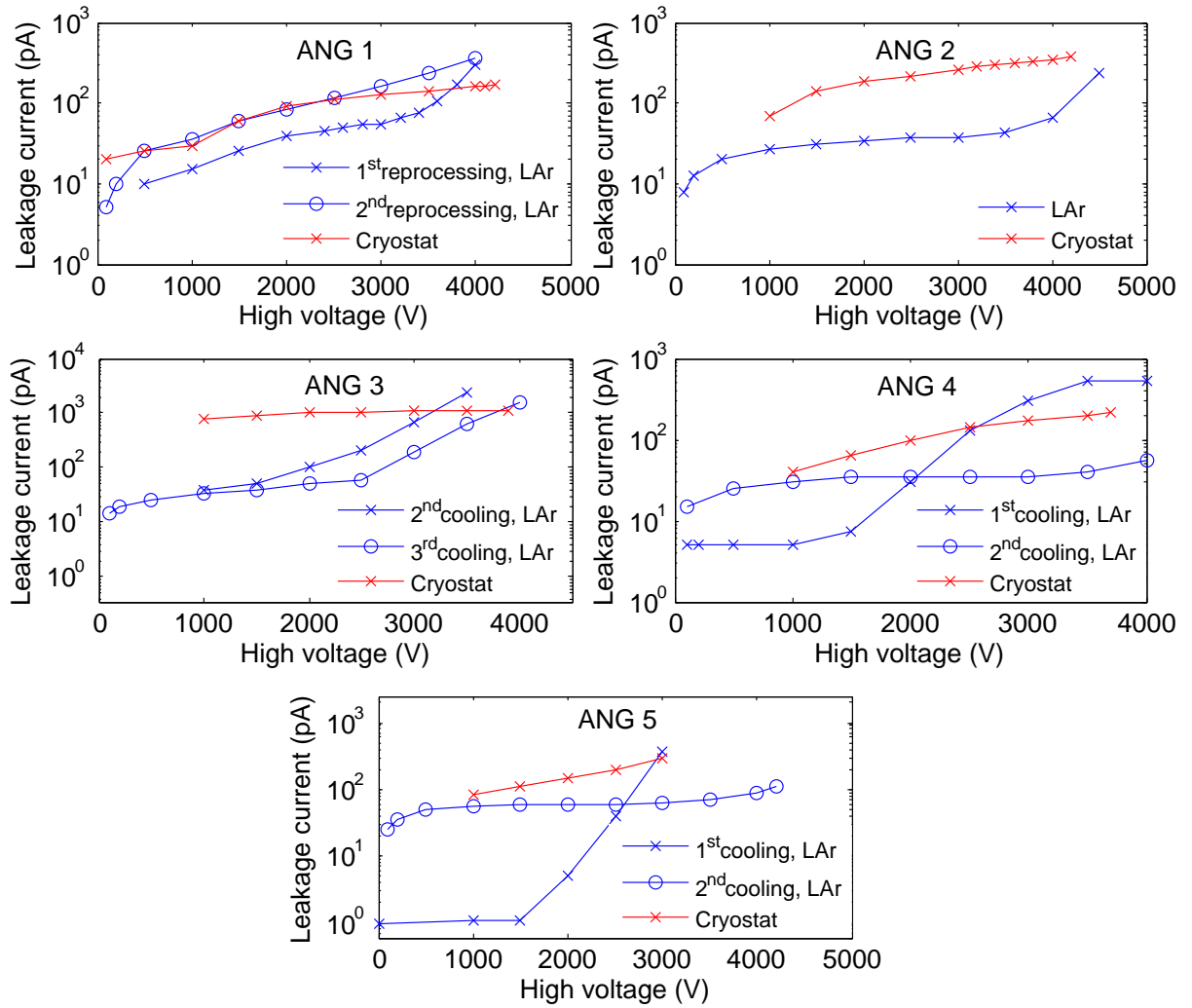


Figure 7.3: Current-voltage curves of ANG detectors, after their reprocessing, measured in the liquid argon test bench of GDL. The accuracy of the leakage current is ± 10 pA. The curves are compared to those measured with the detectors in their cryostats [13]. For ANG 1, the curves measured after its first and second reprocessings are shown. Additional temperature cycles were performed with ANG 3, ANG 4 and ANG 5 to reduce their leakage current.

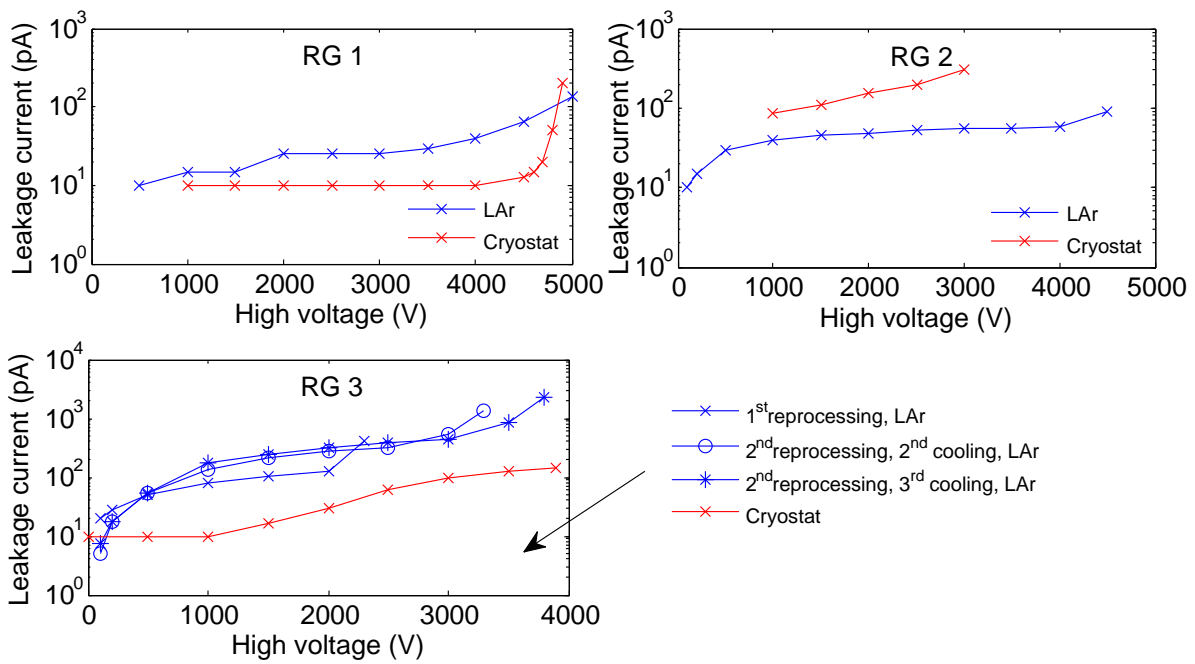


Figure 7.4: Current-voltage curves of RG detectors, after their reprocessing, measured in the liquid argon test bench of GDL. The accuracy of the leakage current is ± 10 pA. The curves are compared to those measured with the detectors in their cryostats [13]. For RG 3, the curves measured after its first and second reprocessings are shown. After the removal of its passivation layer, additional temperature cycles were performed to reduce its leakage current.

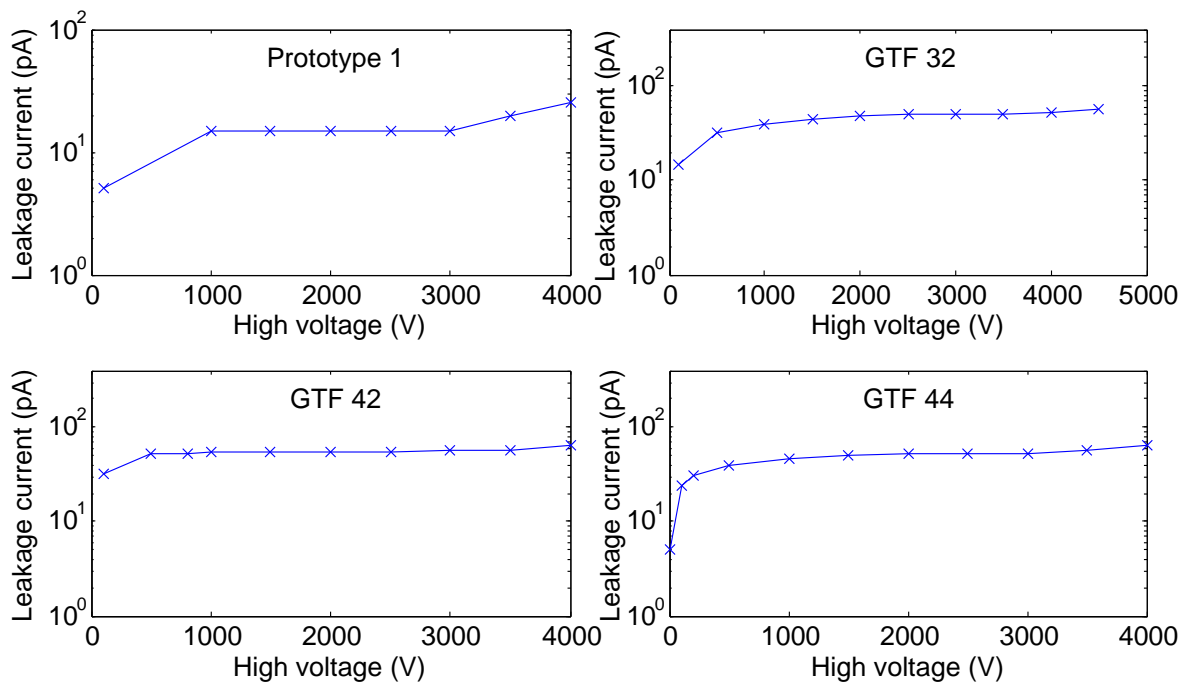


Figure 7.5: Current-voltage curves of Prototype 1, GTF 32, 42 and 44 after their reprocessing, measured in the liquid argon test bench of GDL. The accuracy of the leakage current is ± 10 pA.

7.2.2 Operational voltage measurement

The operational voltage is the voltage at which the detector performance is optimal. This is determined by the best achieved energy resolution after reaching full depletion. When the depletion voltage is reached, the peak position and the detector capacitance become stable as a function of HV, and the peak count rate is saturated. The operation voltage is typically a few hundreds Volts above the full depleted voltage depending on the LC and the resolution curves. To establish the operational voltage of the detectors, the count rate under the peak, the position of the peak and the resolution (FWHM) were measured in function of the HV. The measurements were performed with a ^{60}Co source. The resolution of the pulser peak at 1.4 MeV were also recorded. Figure 7.6, 7.7 and 7.8 present the counting characteristics and the energy resolution measured in the LAr test bench with the ANG detectors, the RG detectors and the non-enriched detectors, respectively.

From these curves, the full depletion voltage and the operational voltage of the detectors were determined (Table 7.1). For all detectors, the full depletion voltage established in the LAr test bench corresponds to the one determined by the capacitance measurement at the detector manufacturer, after the reprocessing (Fig.6.6, 6.7 and 6.8). The operational voltage of the enriched detectors measured in GDL is in good agreement with the value given by the detector manufacturer at the time of their production (Table 6.1). On the contrary, the operational voltage of the GTF detectors determined in the GDL test bench exceeds the value given by their original manufacturer (Table 6.3). For RG-3, the depletion voltage was reached at 3300 V. At the manufacturer specified operational voltage (3800 V), the resolution worsened significantly due to a high LC. Therefore, the optimal voltage is at the full depletion. With an improvement of the LC, better spectroscopic performance is expected at higher voltages.

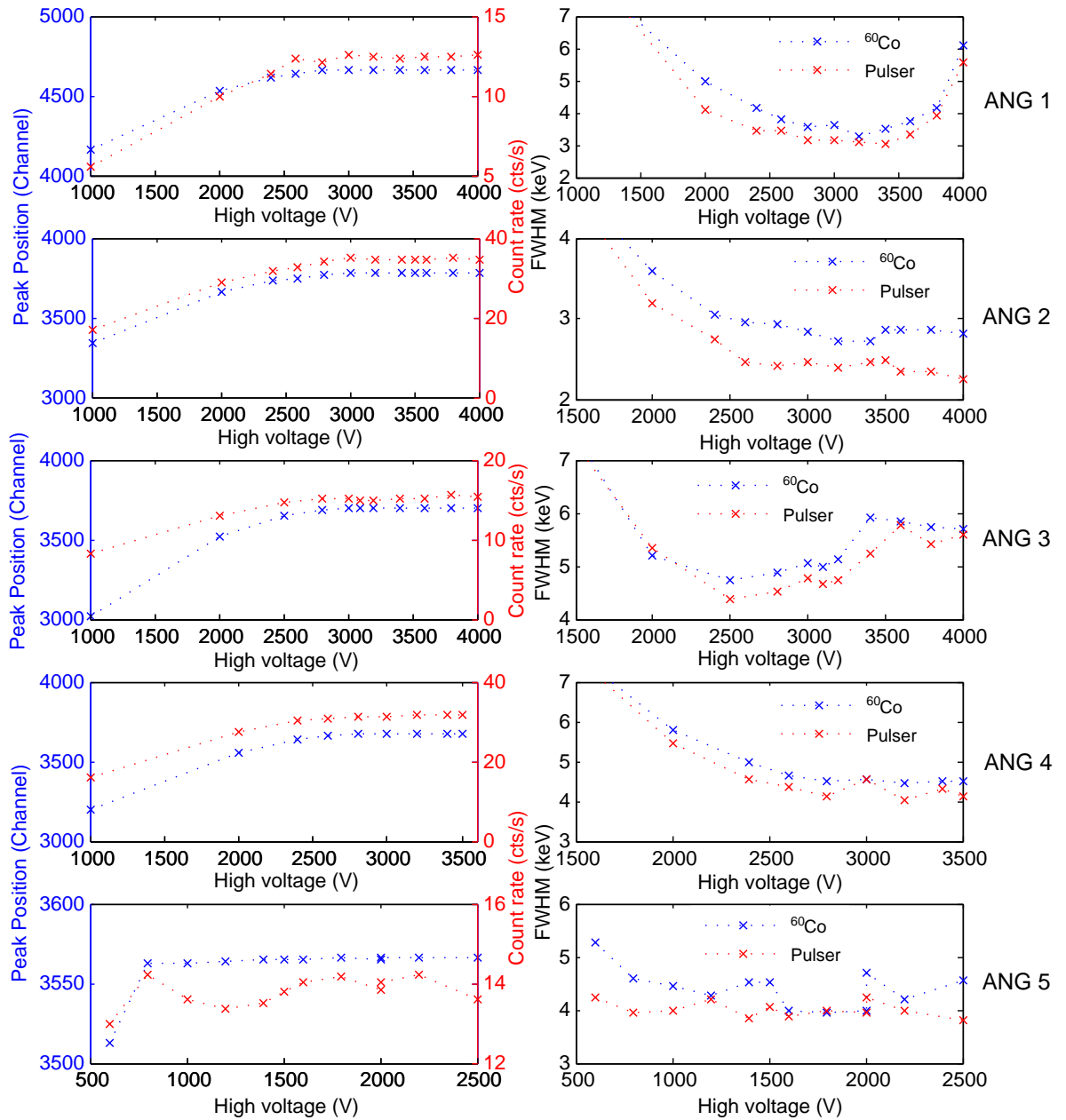


Figure 7.6: Counting characteristics and energy resolution (FWHM) of the ANG detectors, after their reprocessing, measured in the liquid argon test bench of GDL. The energy resolution is given for the 1.332 MeV peak of ^{60}Co and the 1.4 MeV pulser peak. The relative statistical fluctuation of the count rate was below 3%. The reason for the instability of ANG 5 count rate at low HV is unclear but could be caused by e.g. charge trapping effects.

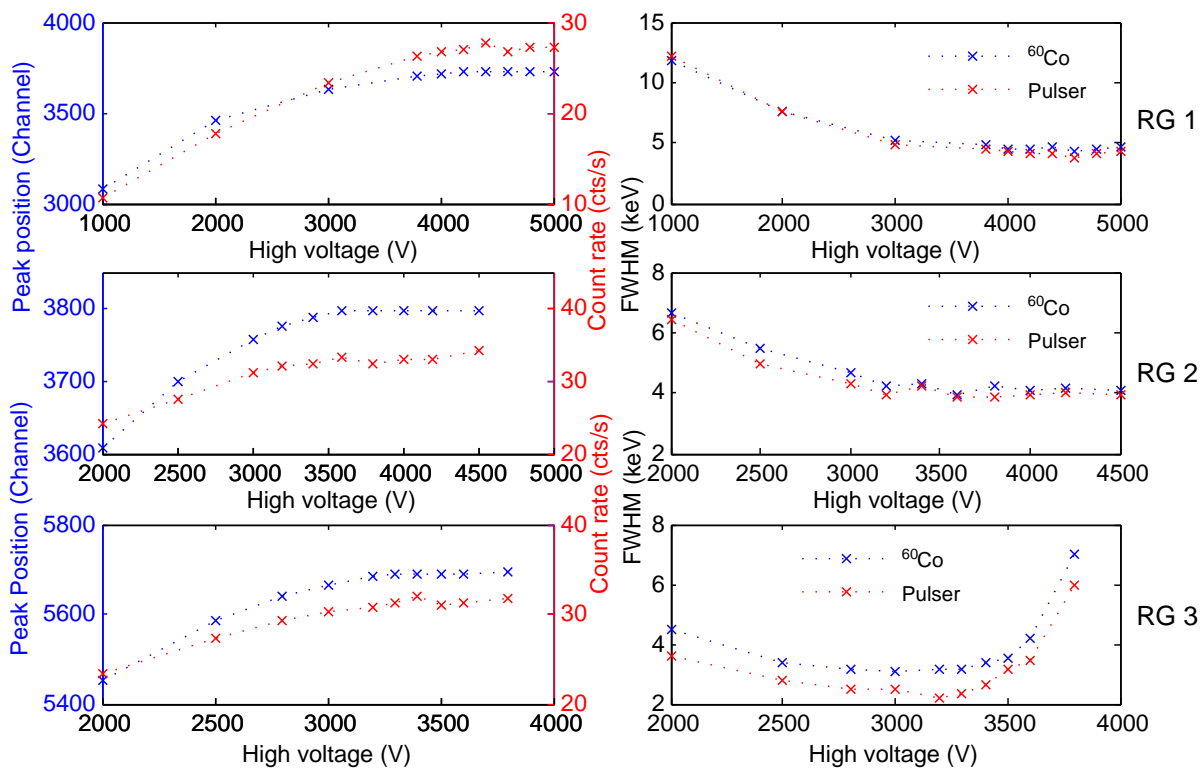


Figure 7.7: Counting characteristics and energy resolution (FWHM) of the RG detectors, after their reprocessing, measured in the liquid argon test bench of GDL. The energy resolution is given for the 1.332 MeV peak of ^{60}Co and the 1.4 MeV pulser peak. The relative statistical fluctuation of the count rate was below 3%.

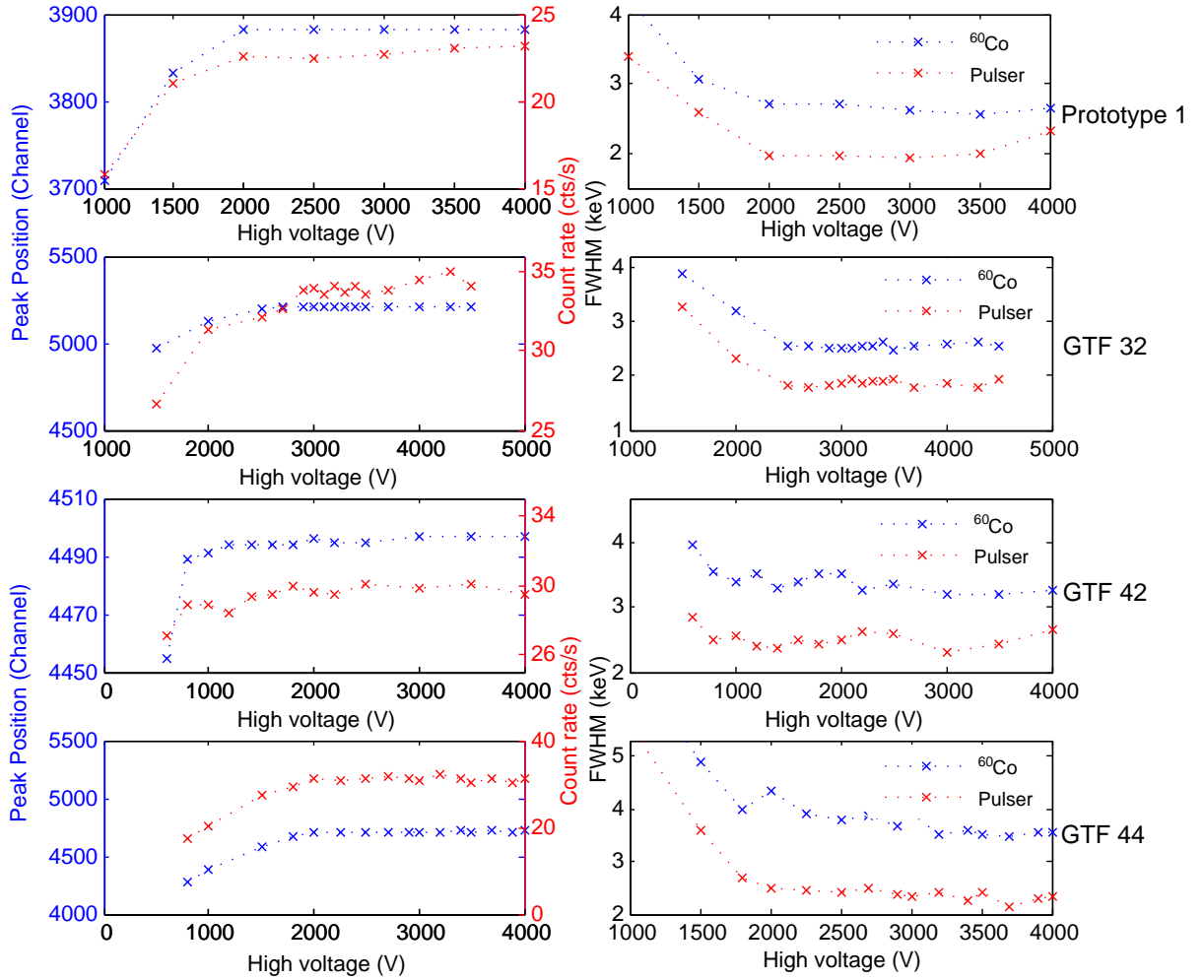


Figure 7.8: Counting characteristics and energy resolution (FWHM) of Prototype 1, GTF 32, 42 and 44 after their reprocessing, measured in the liquid argon test bench of GDL. The energy resolution is given for the 1.332 MeV peak of ^{60}Co and the 1.4 MeV pulser peak. The relative statistical fluctuation of the count rate was below 3%.

Detector	Depletion voltage (V)	Operational voltage (V)
ANG 1	3000	3200
ANG 2	3000	3500
ANG 3	3000	3200
ANG 4	2800	3200
ANG 5	1000	1800
RG 1	4200	4600
RG 2	3800	4500
RG 3	3300	3300
GTF 32	3000	3500
GTF 42	1500	3000
GTF 44	2000	3500
Prototype 1	2000	3000

Table 7.1: Full depletion and operational voltages of the Phase-I detectors determined in the liquid argon test bench of GDL, after their reprocessing for GERDA.

7.2.3 Study of the spectroscopic performance

The energy resolution measured with the Phase-I detectors in the GDL test bench ranges between 2.5 and 5.1 keV (FWHM) at the 1.332 MeV spectral line of ^{60}Co . Table 7.2 presents a summary of the Phase-I detector tests in LAr.

The energy resolution measured with ANG 1, ANG 2, GTF 32 and Prototype 1 was ~ 2.5 keV (FWHM) for the 1.332 MeV γ -ray line of ^{60}Co . The FWHM measured with GTF 44 was 3.0 keV, which is better than the value stated by the detector manufacturer (3.1 keV). The energy resolution of RG 3 was limited by the LC (from equation 3.2, the LC contribution to the noise was ~ 1.6 keV). With ANG 4, 5 and RG 1, 2, inferior energy resolution was measured despite of their low LC.

Tests performed with GTF 32 showed that better energy resolution can be achieved by improving the HV contact via further polishing of the diode surface to remove completely the germanium oxide. With the habitual polishing, the warm and the cold electrical resistance was $R_{warm} \approx 90 \Omega$ and $R_{cold} \approx 2 \text{ k}\Omega$. Energy resolutions of 4 keV (FWHM) for the 1.332 MeV ^{60}Co line and 3.7 keV (FWHM) for the pulser line at 1.4 MeV were measured. With further polishing of the diode surface and by polishing also the copper

Detector	Date	R_{warm} (Ω)	R_{cold} ($k\Omega$)	HV (V)	LC (pA)	Shaping time (μs)	FWHM (keV) Pulser	^{60}Co
ANG 1	04-06/11	40	3.1	3500	235	6	2.1	2.6
ANG 2	25-26/08	30	1.2	4000	65	10	2.1	2.5
ANG 3	27-28/08	50	1.9	3000	200	3	4.8	5.1
ANG 4	16-18/08	70	2.2	3000	40	10	4.1	4.4
ANG 5	21-22/08	40	2.3	1500	60	6	3.9	4.0
RG 1	18-20/08	50	2.3	4500	65	10	3.8	4.4
RG 2	22-25/08	50	2.0	4000	60	10	3.9	4.1
RG 3	11-12/11	26	2.7	3500	800	6	3.1	3.5
GTF 32	30-31/10	50	3.5	3200	50	10	2.1	2.5
GTF 42	04-07/08	60	3.5	3000	55	6	2.3	3.2
GTF 44	08-10/08	60	2.1	3500	55	10	2.0	3.0
Prototype 1	29-31/07	70	3.7	3000	10	10	2.0	2.6

Table 7.2: Measurement summary with the Phase-I detectors mounted in their low-mass holders and operated in the liquid argon test bench of GDL: date, warm and cold electrical resistance between the signal and the high voltage contact, leakage current at the given high voltage, and spectroscopic performance (FWHM) for the pulser at 1.4 MeV and for the 1.332 MeV ^{60}Co line measured at the given high voltage and shaping time. The errors on R_{warm} , R_{cold} and LC are 5 Ω , 0.2 k Ω and 10 pA, respectively. The relative error on FWHM is $\sim 2\%$.

contact under nitrogen atmosphere to prevent oxidation, the warm and the cold resistance became $R_{warm} \approx 50 \Omega$ and $R_{cold} \approx 1.4 k\Omega$. The spectroscopy performance was improved to 2.5 keV (FWHM) for the ^{60}Co peak and to 2.1 keV (FWHM) for the pulser peak. Afterwards, the same polishing procedure was applied to ANG 1, RG 3 and GTF 44. Using the same procedure with ANG 4, 5 and RG 1, 2, is expected to improve their resolution as well. This will be done before operating the detectors in GERDA.

As presented in Chapter 3 for Prototype 1, analysis of the baseline noise were performed to investigate the spectroscopic performance of some enriched detectors. Baseline pulses were acquired with ANG 2, ANG 3 and ANG 5 with a 100 MHz 14 bit FADC and a sampling time of 1 ms. The fast Fourier transform (FFT) analysis are displayed in Fig.7.9. The FFT of the baseline pulses collected with Prototype 1 (already presented in Fig.3.13) is also shown for comparison. Different amplitudes of FFT were obtained at low frequencies for the different detectors. The results are consistent with the spectroscopy measurements (lower amplitude corresponds to better energy resolution). The most likely explanation for the worse resolution obtained with ANG 3 and 5 is an imperfect HV contact. A bad contact

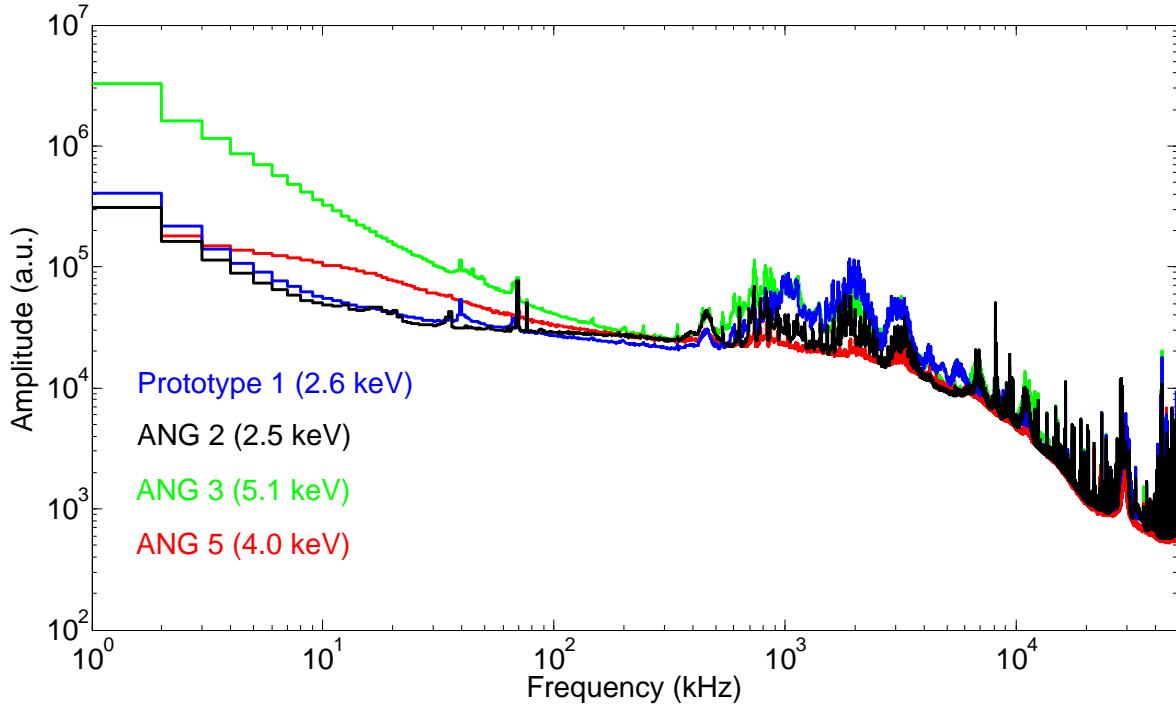


Figure 7.9: Fast Fourier transform analysis of baseline pulses collected with some of the Phase-I detectors operated in the liquid argon test bench of GDL. The detectors were connected to a first stage preamplifier mounted in the neck of the dewar, in argon gas. The frequency resolution is 1 kHz.

is equivalent to an extra resistance. However, it is difficult to express this quantitatively.

7.3 Measurement of the active masses

The detection efficiency measurements were performed with the detectors biased at or above their operational voltage, to be sure that the active volume was at its maximal value. The efficiency was measured with a ^{60}Co source with an activity of $35 \pm 3\%$ kBq. A hole in the lead shield of Test Bench 1 (~ 2 mm diameter) allowed to place the source at a fixed position, approximately 30 cm from the detector assembly, outside the dewar. With the source in this position, the counting rate under the full-energy-peak at 1.332 MeV was on the order of 5 cts/s. High statistic measurements were performed with each detector, typically overnight. Spectra with a minimum of 25 000 counts under the peak were collected. After subtracting the background, the spectra were analysed calculating the full-energy-peak efficiency, using the activity of the source (Fig.7.10).

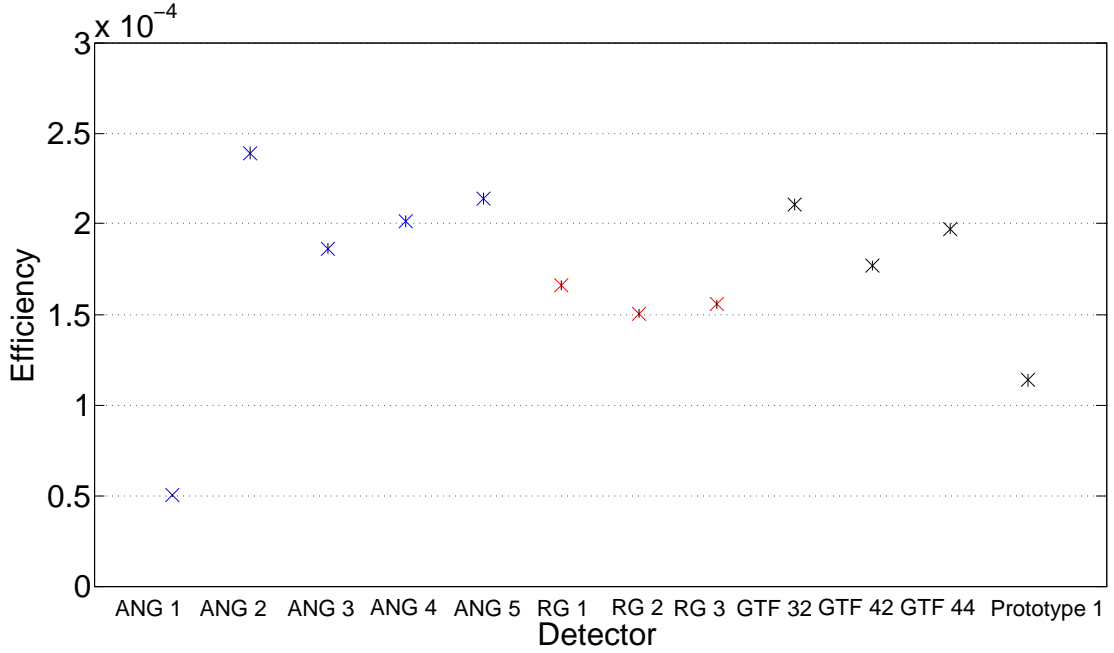


Figure 7.10: Full-energy-peak detection efficiency measured in the GDL test bench, for the 1.332 MeV ^{60}Co line, for ANG (x), RG (x), and GTF and Prototype 1 (x) detectors. The uncertainties on the efficiencies are indicated by the vertical bars.

To determine the active masses of the detectors, the measured detection efficiencies were compared to Monte Carlo simulations. The code used was MaGe [75, 76], developed for the Majorana and GERDA experiments, based on Geant4 [57]. The software description of the setup includes the outer and the inner vessel of the dewar, the infrared shield and the detector. The inner vessel and the infrared shield were filled with LAr. The detector description included the bore hole, the groove and the dead layer. The detector dimensions measured after the reprocessing (Table 6.4) were used. Simulations with and without the detector holder showed a difference of $\sim 1\%$ on the full-energy-peak efficiency. Therefore, for the simulations presented here, the detector holder was not included. The rounding of the diode edges was included for some simulations but no effect on the detection efficiency was found at our level of accuracy. Only the missing part of the outer portion of RG 3 near the bore hole side was taken into account for the results presented here. A schematic drawing of the test bench dewar and the Monte Carlo software model are shown in Fig.7.11.

The Geant4 default G4ParticleGun generator was used to produce photons from ^{60}Co decays. For each simulation, $1.5 \cdot 10^8$ decays were created. The simulated energy spectra were generated with 1 keV bin width. The spectra were then analyzed the same way as the measured spectra.

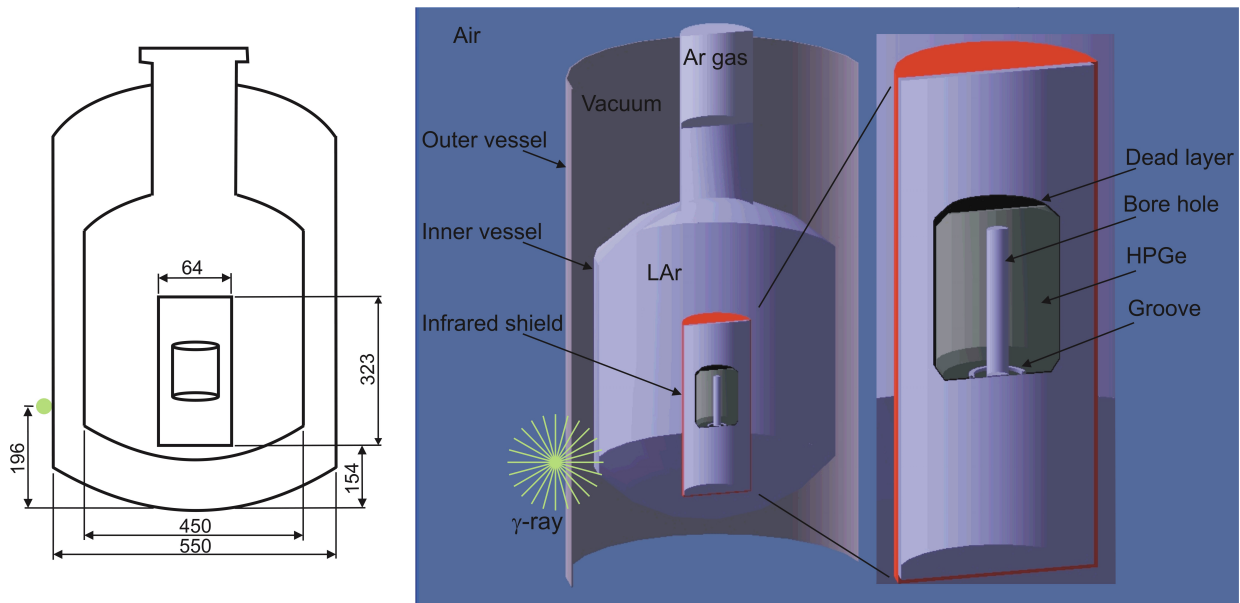


Figure 7.11: **Left:** Schematic drawing of the test bench dewar in which the bare detectors were operated. A ^{60}Co point like source was placed on the external wall of the outer vessel, approximately 4 cm higher than the bottom of the infrared shield. **Right:** Monte Carlo software representation of the setup. The detector description included the bore hole, the groove and the dead layer. The dimension subjected to the optimization for the active volume determination is the dead layer thickness.

As the exact positions of the detectors inside the infrared shield, relative to the source position, were difficult to determine due to uncertainties in the positions of the setup components. Therefore, the following procedure was used. Simulations were performed with Prototype 1 using the dead layer thickness previously measured at the detector manufacturer ($0.85 \text{ mm} \pm 5\%$). Tuning of the detector position in the z direction in the software model was performed. The detector position was determined by matching the simulated and the measured full-energy-peak efficiency. The detection efficiency was measured twice with Prototype 1. In between, the detector was warmed-up and the source was removed. The two efficiency measurements were compared to the simulations and used to determine the uncertainty of the detector position ($\pm 1 \text{ cm}$).

Figure 7.12 shows a comparison of a measured and a simulated spectrum for Prototype 1. The results of the simulations show rather good agreement with the results of the measurement. In the Monte Carlo simulation, the full-energy is deposited within 1 keV bin, in contrast to the measured spectrum where the energy is deposited in a wider area due to the finite energy resolution of the detector (for the measured spectrum presented here, the energy resolution was 2.8 keV (FWHM)). This explains the difference between

the full-energy peak efficiencies measured and simulated.

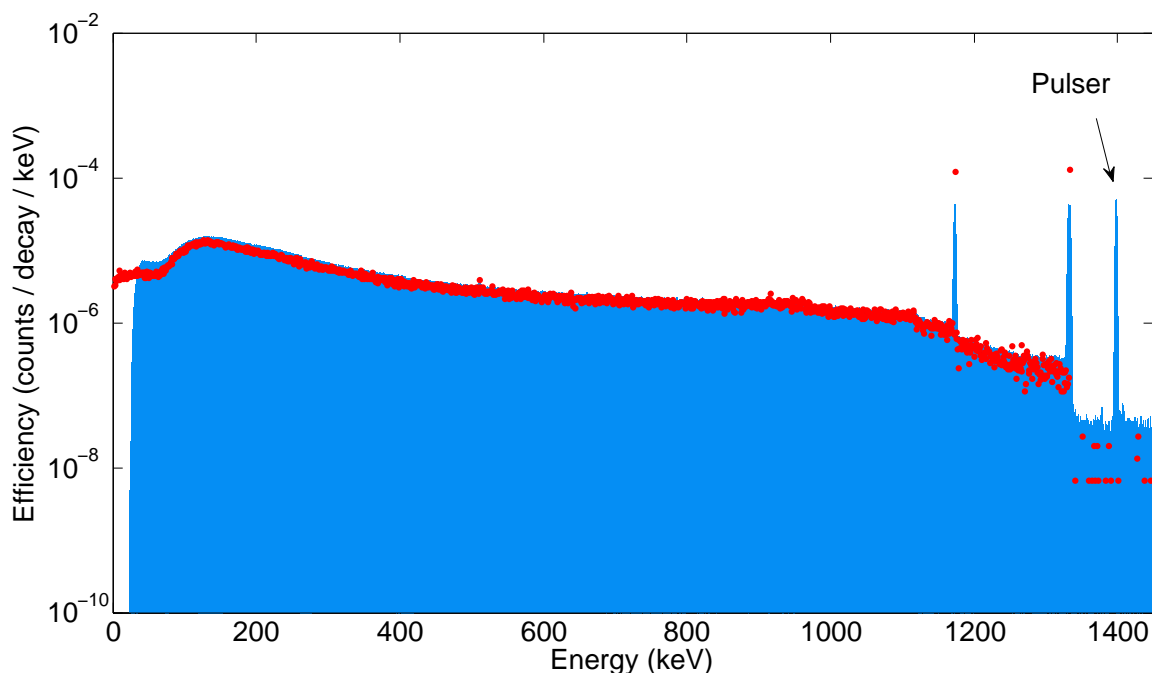


Figure 7.12: A comparison of a measured and a simulated ^{60}Co spectrum for Prototype 1. The measured spectrum is indicated by the filled area and the Monte Carlo simulated spectrum by the red points. For the measured spectrum, the energy resolution of a pulser at 1.4 MeV was monitored and the data acquisition threshold was ~ 30 keV.

The position of the other detectors was determined assuming the top of the assemblies at the same level as Prototype 1. The active volumes of the detectors were adjusted by changing the thickness of the dead-layer (by 0.1 mm step homogeneously at the whole dead layer surface). The optimized dead layer does not necessarily reflect the real dead layer of the detector, but rather a parameter of the Monte Carlo software representation for the detector geometry. The effective dead layer was refined by matching the simulations to the γ -ray source measurement. The count rate variation corresponding to the position uncertainties was also computed using Monte Carlo simulations, and taken into account in the uncertainty of the effective dead layer thickness. Figure 7.13 presents the Monte Carlo results for the tuning of the detector position and of the effective dead layer thickness. The effective dead layer thicknesses were determined with a large uncertainty ($\sim 50\%$) due to the uncertainty in the detector positioning.

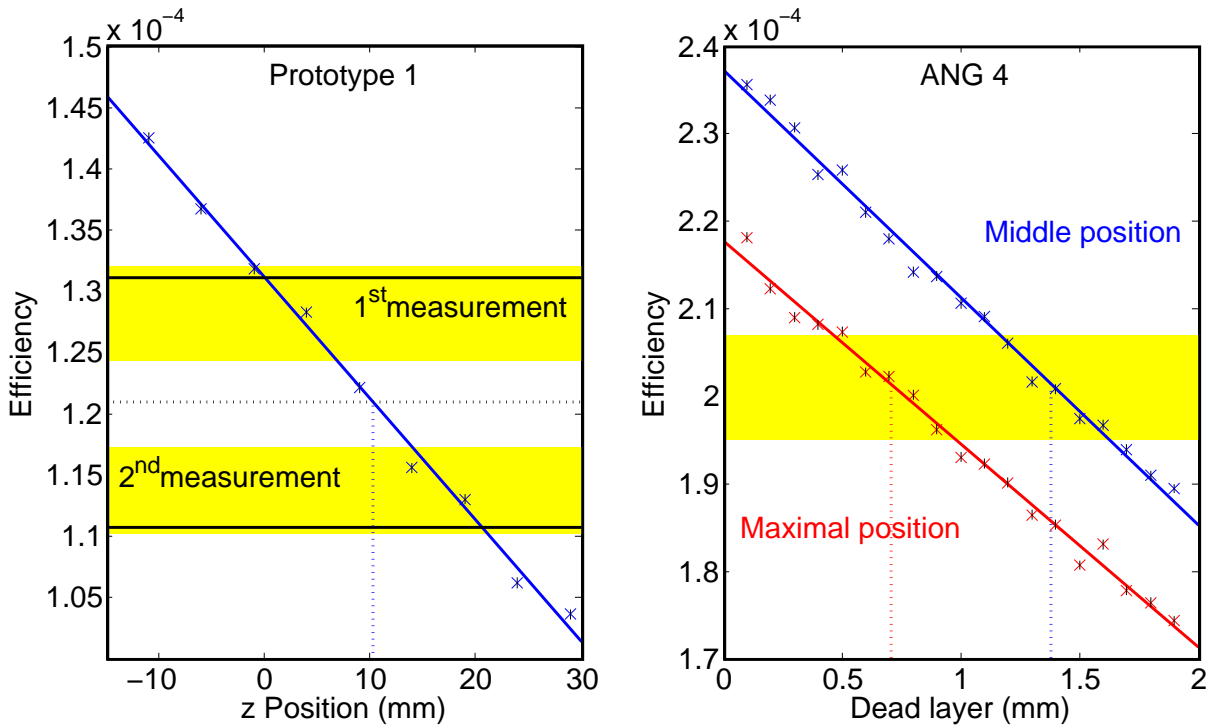


Figure 7.13: Monte Carlo results for the full-energy-peak efficiency of the 1.332 MeV γ -line of ^{60}Co . The horizontal bars refer to the measured detection efficiencies and include the uncertainty of the source activity. The vertical uncertainty bars of the Monte Carlo data points represent statistical uncertainties. **Left:** Tuning of the vertical position of Prototype 1 using the dead layer thickness measured at the detector manufacturer (0.85 mm). The position refers to the middle of the infrared shield. Two separate measurements were performed and the combined data used to determine the position and its uncertainty. **Right:** An example of the effective dead layer interpolation, with ANG 4 detector. Two set of simulations were performed, with the detector in the middle position and in the maximal position, given by the results with Prototype 1.

Finally, using the dimensions of the diodes measured at the detector manufacturer after the reprocessing (Table 6.4) and the determined effective dead layer thicknesses, the active masses were calculated (Table 7.3). The combined active mass for the Phase-I enriched detectors was evaluated to 15.3 ± 0.4 kg, which corresponds to $87 \pm 3\%$ of the total mass. The error on the combined mass was calculated as follows. The individual errors due to the positioning uncertainty were added quadratically (these errors are random as each detector can be located in a different position). In addition, the source activity uncertainty which results in a relative error of $\sim 2\%$ on the active mass was calculated for the combined mass. The total error is then the quadratic sum of both errors.

Detector	Effective Dead layer (mm)	Active mass (g)	Active mass (%)
ANG 1	1.8 ± 0.5	795 ± 43	83 ± 4
ANG 2	2.3 ± 0.7	2468 ± 121	87 ± 4
ANG 3	1.9 ± 0.7	2070 ± 117	87 ± 5
ANG 4	1.4 ± 0.7	2136 ± 116	90 ± 5
ANG 5	2.6 ± 0.6	2281 ± 109	83 ± 4
RG 1	1.9 ± 0.7	1851 ± 107	88 ± 5
RG 2	1.9 ± 0.7	1856 ± 101	86 ± 5
RG 3	1.4 ± 0.7	1868 ± 95	90 ± 5
GTF 32	0.4 ± 0.8	2251 ± 122	97 ± 5
GTF 42	2.8 ± 0.6	2018 ± 84	82 ± 3
GTF 44	2.0 ± 0.7	2124 ± 110	86 ± 4
Prototype 1	$0.85 \pm 0.04^*$	1453 ± 5	93 ± 1

Table 7.3: Active mass summary for the Phase-I detectors after their reprocessing. The effective dead layer thicknesses were obtained by comparing the detection efficiency measurements to Monte Carlo simulations. The error on the dead layer includes the uncertainties on the detector position and on the measured detection efficiency (mainly due to the uncertainty of the source activity). The active masses, in gram and as percentage of the total mass, were calculated with the effective dead layer thicknesses, and the diode dimensions and total mass given by the detector manufacturer. *The dead layer thickness of Prototype 1 was measured at the detector manufacturer.

The determination of the active mass was a side objective of the detector characterization in the LAr test bench. The result obtained is different from the active mass determined before the reprocessing (17.16 ± 0.08 kg which corresponded to $\sim 96\%$ of the total mass). The measurements presented here were affected by high systematic uncertainties in the detector positioning. Our measurements showed that a small shift in the detector position,

even if located relatively far from the γ -ray source, has a big impact on the detector efficiency. This uncertainty is included in the results, however, it is difficult to take into account all sources of systematic errors. A test setup with better defined geometry would be needed to determine the active mass with higher accuracy, e.g. operating the detectors in a standard vacuum cryostat.

7.4 Conclusion

All Phase-I enriched detectors and four natural germanium detectors were operated in the LAr test bench of GDL after their reprocessing for GERDA. The diodes were mounted in their low-mass holders and their parameters (LC, counting characteristics, energy resolution and detection efficiency) measured. After their delivery, some of the detectors had a higher LC than measured at the detector manufacturer. A simple additional temperature cycle was found to be effective at restoring the LC of detectors without passivation layer. Finally, the measured LC of most of the detectors was at the same level as measured at the manufacturer. The detector full depletion and operational voltage determined is in good agreement with the one specified by the manufacturers. With optimized HV contact, the energy resolution achieved with the Phase-I detectors in the GDL test bench was 2.5 keV (FWHM) for the 1.332 MeV γ -line of ^{60}Co , using a signal cable of ~ 60 cm connecting the detector assembly to the first stage preamplifier. For the detectors which had inferior energy resolution, the HV contact can be improved by extra polishing of the diode surface, without dismounting completely the detector assembly. By comparing the detection efficiency to Monte Carlo simulations, the active masses of the detectors were determined. The total active mass of the Phase-I enriched detectors was evaluated at 15.3 ± 0.4 kg. However, this measurement included large systematic error. In the limited time available, the detectors GTF 45, 110 and 112 were not tested. Their low-mass holders were constructed and the detectors will be characterized in the near future. After their operation, the Phase-I detectors were stored, mounted in their low-mass holder, under vacuum ($\sim 10^{-6}$ mbar) in their transportation container. The detectors are ready for their operation in GERDA.

Chapter 8

Summary and outlook

This dissertation comprises work with germanium detectors necessary for Phase-I of GERDA. GERDA will search for the neutrinoless double beta decay ($0\nu\beta\beta$) of ^{76}Ge at the Laboratori Nazionali del Gran Sasso (LNGS). Bare high purity germanium (HPGe) detectors enriched in ^{76}Ge will be submerged in liquid argon (LAr) serving simultaneously as a shield against external radioactivity and as a cooling medium. By operating bare detectors, the amount of material in the detector support structure, which was the dominant background in past ^{76}Ge $0\nu\beta\beta$ experiments, is minimized. GERDA aims at an extremely low-background (10^{-3} cts/(keV·kg·y)) and at an excellent energy resolution (3-4 keV) in the region of interest (2039 keV). In GERDA Phase-I, reprocessed enriched detectors, which were previously operated by the Heidelberg-Moscow and IGEX collaborations, will be redeployed.

The novel method of bare detector operation in LAr over more than three years has been extensively studied. In addition, a lot of experience regarding the handling of the HPGe diodes was gained. Feasibility of bare detector operation in cryogenic liquids, LAr and liquid nitrogen (LN_2), was tested with non-enriched prototype detectors, first at the manufacturer site, and then in the GERDA underground Detector Laboratory (GDL). New unpredicted effects were discovered and taken into account in the reprocessing of the Phase-I detectors. The characteristics of the reprocessed detectors were subsequently measured. The main results are summarized below:

- The standard p-type HPGe detector technology from Canberra Semiconductor NV, Olen, was chosen for Phase-I. The detectors have a 'wrap around' n+ conductive lithium layer which is separated from the p+ contact by a groove.
- The low-mass detector holder with the electrical contacts was designed and tested with a prototype detector. The detector assembly fulfills the requirements for GERDA in terms of ultra-low background, simple mounting procedure and mechanical stability. The energy resolution of the prototype detector mounted in the low-mass holder, mea-

sured at the detector manufacturer site, was 2.2 keV (FWHM) at 1.332 MeV with a ~ 40 cm long signal cable connecting the detector to the first stage preamplifier. The resolution was the same as measured in a standard vacuum cryostat.

- The GDL was constructed in a close neighborhood to the main GERDA site at LNGS. It offers all facilities to handle the HPGe diodes and to test the bare detectors in LAr before their operation in GERDA. The diodes are manipulated in an ultra-clean environment under nitrogen atmosphere. There are two LAr/LN₂ test benches operational in GDL. The test benches were optimized for cleanliness, low leakage current (LC) measurements (< 10 pA) and good energy resolution. The energy resolution achieved in the GDL test benches was 2.5 keV (FWHM) at 1.332 MeV, using ~ 60 cm long signal cable.
- The detector response to γ -radiation in LAr and LN₂ was investigated. Gamma irradiation of a bare prototype with a standard groove passivation procedure, operated in LAr and biased with high voltage (HV), results in a continuous increase of the LC (on the order of 10^{-2} nA per day of irradiation using a ⁶⁰Co source with an activity of ~ 40 kBq located approximately 20 cm away from the detector). The γ -radiation induced LC is a reversible process. The LC is partly restored to its initial value by γ irradiation without applying HV and totally restored by a warming/cooling cycle. The γ -radiation induced LC is caused by charge produced by the ionization of LAr atoms which subsequently are collected on the detector passivation layer. Reducing the size of the passivation layer strongly reduces the LC increase. Stable LC values under γ irradiation were observed with a detector without a passivation layer. No γ -radiation induced LC is observed in LN₂. Even though no long-term γ irradiation of the detectors will be performed in GERDA, the discovery of this effect is valuable for the operation of bare germanium detectors and it led to the final design of the Phase-I detectors (without passivation layer).
- The long-term stability in LAr was investigated with three prototype detectors using different groove passivation procedures. The results show that a good long-term stability can be achieved with bare germanium detectors in LAr. For a prototype with a full passivation layer and a protective disk, the LC was stable at ~ 30 pA during a six month long operation in LAr. For a prototype with a reduced passivation layer, a LC increase (~ 40 pA) was measured after four months of operation. Such an increase is negligible in terms of energy resolution. A prototype detector without passivation layer was operated for three months and the LC was perfectly stable at ~ 5 pA.
- The Phase-I diodes were reprocessed without a passivation layer. The total mass reduction was calculated to be ~ 300 g out of 17.9 kg. The exposure of the diodes above

ground for the reprocessing was ~ 5 days. The resulting background from the cosmogenically produced ^{60}Co and ^{68}Ge was estimated to $(0.4 - 0.6) \cdot 10^{-3}$ cts/(keV·kg·y).

- The Phase-I diodes were mounted in their final low-mass holders and the detector characterization in the LAr test bench of GDL was performed. Detector parameters comparable to those measured in standard vacuum cryostats were measured. Apart from improving the HV contacts of some detector assemblies, the diodes will not be dismantled before their operation in GERDA.

Before the start of GERDA, the next step is to test a Phase-I string with three detectors. This will be performed with a dewar of ~ 1 m height attached to a glove-box. This test is presently under preparation. Furthermore, the detectors will be integrated with the final Phase-I front-end electronics operated in LAr. Afterwards, the Phase-I detectors will be submerged into the GERDA cryostat and the search of $0\nu\beta\beta$ will start.

Acknowledgements

I would like to thank my supervisors, my colleagues, my family and my friends. They knew how to support and to orientate me throughout my PhD studies. I am also grateful to the Natural Sciences and Engineering Research Council of Canada (NSERC) for the financial support during my PhD.

I express my thanks to an excellent physicist and an extraordinary person, Stefan Schönert, who gave me the opportunity to participate to the GERDA experiment. He offered me a very interesting topic and supervised me during my studies. Because of him, I learned and accomplished a lot. I also give my gratitude to Prof. Wolfgang Hampel for being my PhD adviser. I have appreciated his help and constructive comments for my dissertation. Special thanks to Anatoly Smolnikov who followed my work and advised me during my PhD studies. His careful reading of my dissertation, his comments and suggestions had significant impacts.

Then, I owe thousand thanks to Oleg Chkvorets and Konstantin Gusev for showing and teaching me everything concerning germanium detectors. This thesis presents our team work. I really appreciated our complicity inside and outside the tunnel. It was not always (I should say rarely) easy but finally we achieved very good results.

Special thank to Carla Cattadori. Several results presented in this thesis, mainly for the γ -radiation induced leakage current effect, derived from her ideas. Her help and support were very valuable and I also appreciated her friendliness. Assunta Di Vacri also contributed significantly to the results presented in this thesis. I would also like to thank several people for their help and assistance with the test setup at LNGS: Andrey Chernogorov, Alessio D'andragora, Stefano Gazzana, Matthias Junker, Mark Shirchenko and Andrey Vasenko.

Un gros MERCI to Dušan Budjáš. Without him, this thesis would not have been comprehensible (assuming that it is now). Besides all his help for my thesis, thanks for just being there. A particular thank you to Grzegorz Zuzel who helped me through my whole thesis on several aspects (e.g. radon and vacuum measurements, multitude of heavy works, thesis correction). I am grateful also to the expertise of Herbert Strecker, Ute Schwan, Bernhard Schwingenheuer, Stefan Flicker, Massimiliano De Deo and the team at Canberra Semiconductor NV, Olen.

Thanks to my colleagues from MPIK: Mark Heisel, Alexander Kartavtsev, Sebastian Lindemann, Werner Maneschg, Peter Peiffer, Hardy Simgen. Thanks also to Brigitte Villaumie and Anja Berneiser for their precious help.

I am grateful to my sister Fanie, who welcomed me in Stockholm and helped me to startup

the writing. Thanks also to Marie Di Marco, first for encouraging me to come to Heidelberg, and then for her suggestions and comments during my studies. Finally, thanks to my precious family and friends, one has to forget about the work and to get distracted sometimes.

Finally, I really appreciated to be part of the GERDA collaboration and I wish enormous success to the experiment.

Bibliography

- [1] Griffiths, D J, **Introduction to Elementary Particles**, Wiley, John & Sons, Inc., ISBN 0-471-61544-7, 1987.
- [2] Ashie Y et al., **Measurement of atmospheric neutrino oscillation parameters by Super-Kamiokande I**, Phys. Rev. D, Vol.71, No.11, 112005 (35 pages), 2005.
- [3] Cleveland B T et al., **Measurement of the solar electron neutrino flux with the Homestake chlorine detector**, Astrophysics Journal, Vol.496, pp.505-526, 1998; Hosaka J et al., **Solar neutrino measurements in Super-Kamiokande-I**, Phys. Rev. D, Vol.73, 112001 (33 pages), 2006; Hampel W et al., **GALLEX solar neutrino observations: results for GALLEX IV**, Phys. Lett. B, Vol.447, pp.127-133, 1999; Altmann M, et al., **Complete results for five years of GNO solar neutrino observations**, Phys. Lett. B, Vol.616, pp.174-190, 2005; Aharmim B et al., **Measurement of the ν_e and Total ^8B Solar Neutrino Fluxes with the Sudbury Neutrino Observatory Phase I Data Set**, Phys. Rev. C, Vol.75, No.4, 045502 (69 pages), 2007; Arpesella C et al., **First real time detection of ^7Be solar neutrinos by Borexino**, Phys. Lett. B, Vol.658, pp.101-108, 2008.
- [4] Abe S et al., **Precision Measurement of Neutrino Oscillation Parameters with KamLAND**, Phys. Rev. Lett., Vol.100, 221803 (5 pages) 2008.
- [5] Ahn M H et al., **Measurement of Neutrino Oscillation by the K2K Experiment**, Phys. Rev. D, Vol.74, 072003 (39 pages), 2006; Adamson P et al., **Study of**

muon neutrino disappearance using the Fermilab Main Injector neutrino beam, Phys. Rev. D, Vol.77, 072002 (34 pages), 2008.

- [6] Maki Z, Nakagawa M, and Sakta S, **Remarks on the Unified Model of Elementary Particles**, Progress of Theoretical Physics, Vol.28, No.5, pp.870-880, 1962.
- [7] Wolfenstein L, **Neutrino oscillations in matter**, Physical Review D, Vol.17, pp.2369-2374, 1978; Mikheev S P, Smirnov A Y, **Resonance oscillations of neutrinos in matter**, Soviet Physics Uspekhi, Vol.30, pp.759-790, 1987.
- [8] Vergados J D, **The neutrinoless double beta decay from a modern perspective**, Physics Reports-Review section OF Phys. Lett., Vol.361, pp.1-56, 2002; Vogel P, **Neutrinoless double beta decay**, arXiv:0611243v1[hep-ph], 2006.
- [9] Moe M, Vogel P, **DOUBLE-BETA DECAY**, Annual review of Nuclear and Particle science, Vol.44, pp.247-283, 1994.
- [10] Aalseth C E et al., **Recent results from the IGEX double-beta decay experiment**, Nucl. Phys. B, Suppl. 48, pp.223-225, 1996.
- [11] Simkovic F, Faessler A, **Distinguishing the $0\nu\beta\beta$ -decay mechanisms**, arXiv:0112272v1[hep-ph], 2001.
- [12] Elliot S R, Vogel P, **Double beta decay**, Annual Review of Nuclear and Particle Science, Vol.52, No.1, pp.115-151, 2002.
- [13] Chkvorets O, **Search for Double Beta Decay with HPGe Detectors at the Gran Sasso Underground Laboratory**, Phd Thesis, 2008, arXiv:0812.1206v1[nucl-ex].
- [14] Klapdor-Kleingrothaus H V et al., **Latest results from the HEIDELBERG-MOSCOW double beta decay experiment**, European Phys. Journal A, Vol.12, pp.147-154, 2001.
- [15] Aalseth C E et al., **Neutrinoless double-beta decay of Ge-76: First results from the International Germanium Experiment (IGEX) with six isotopically enriched detectors**, Physical Review C, Vol.59, pp.2108-2113, 1999.
- [16] Klapdor-Kleingrothaus H V, Krivosheina I V, and Chkvorets O, **Search for neutrinoless double beta decay with enriched ^{76}Ge in Gran Sasso 1990-2003**, Phys. Lett. B, Vol.586, pp.198-212, 2004.
- [17] Aalseth C E et al., **Comment on "Evidence for Neutrinoless double beta decay"**, arXiv:0202018v3[hep-ex], 2002.

- [18] Ardito R et al., **CUORE: A Cryogenic Underground Observatory for Rare Events**, arXiv:0501010v1[hep-ex], 2005.
- [19] Danilov M et al., **Detection of very small neutrino masses in double-beta decay using laser tagging**, Phys. Lett. B, Vol.480, pp.12-18, 2000.
- [20] Super NEMO collaboraton, **SuperNEMO ^{150}Nd statement**, URL: http://nemo.in2p3.fr/nemodocs/nemo/public/SuperNEMO_150Nd_stttement.pdf, 2007.
- [21] Abt I et al., **The GERmanium Detector Array for the search of neutrinoless $\beta\beta$ decays of ^{76}Ge at LNGS**, Proposal to the LNGS P38/04, 2004, arXiv:0404039v1[hep-ex].
- [22] Elliott S R et al, **The Majorana Project**, arXiv:0807.1741v1[nucl-ex], 2008.
- [23] Simgen H, Zuzel G, **Analysis of the Rn-222 concentration in argon and a purification technique for gaseous and liquid argon**, 5th International Conference on Radionuclide Metrology - Low-Level Radioactivity Measurement Techniques ICRM-LLRMT'08, Applied Radiation and Isotopes, Vol.67, No.5, pp.922-925, 2009.
- [24] Baudis L et al., **GENIUS-TF: a test facility for the GENIUS project**, arXiv:0012022v1[hep-ex], 2000.
- [25] Budjaš D et al., **Pulse Shape Analysis with a Broad-Energy Germanium Detector for the GERDA experiment**, arXiv:0812.1735[nucl-ex], 2008.
- [26] Abt I et al., **Identification of photons in double beta-decay experiments using segmented germanium detectors-Studies with a GERDA phase II prototype detector**, Nucl. Instrum. Meth. A, Vol.583, pp.332-340, 2007.
- [27] Peiffer P et al., **Operation of bare HP-Germanium detectors in liquid argon (LAr)**, Nucl. Phys. B - Proc. Suppl., Vol.143, pp.511, 2005.
- [28] Maneschg W, Merle A, Rodejohann W, **Statistical Analysis of future Neutrino Mass Experiments including Neutrino-less Double Beta Decay**, arXiv:0812.0479v1[hep-ph], 2008.
- [29] Heusser G, **Low-radioactivity background techniques**, Annual review of Nuclear and Particle science, Vol.45, pp.543-590, 1995.
- [30] Bellini G, **The Borexino experiment and its expected performances**, Nucl. Phys. B, Proceedings Supplements, Vol.118, pp.55-61, 2003.

- [31] Heusser G et al., **^{222}Rn detection at the $\mu\text{Bq}/\text{m}^3$ range in nitrogen gas and a new Rn purification technique for liquid nitrogen**, Applied radiation and isotopes, Vol.52, pp.691-695, 2000.
- [32] Klapdor-Kleingrothaus H V, Hellmig J, Hirsch M, **GENIUS-Proposal**, 1997.
- [33] Zdesenko Y G, Ponkratenko O A, Tretyak V I, **High sensitivity GEM experiment on 2 beta decay of Ge-76**, Journal of G-Nuclear and Particle physics, Vol.27, pp.2129-2146, 2001.
- [34] Klapdor-Kleingrothaus H V, Hellmig J, Hirsch M, **Future perspectives of double beta decay and dark matter search - GENIUS**, Journal of Phys. G-Nuclear and Particle physics, Vol.24, pp.483-516, 1998.
- [35] Klapdor-Kleingrothaus H V, Krivosheina I V, **Status of GENIUS-TF-II and TF-III The long-term stability of naked detectors in liquid nitrogen**, Nucl. Inst. Meth, Section A, Vol.566, pp.472-476, 2006.
- [36] Gilmore G, Hemingway J, **Practical gamma-ray spectrometry**, John Wiley & Sons Ltd, 1995.
- [37] Vetter K, **Recent developments in the fabrication and operation of germanium detectors**, Annu. Rev. Nucl. Part. Sci.2007.57:363-404, 2007.
- [38] **Canberra Semiconductor, NV**, Lammerdries 25, B-2250, Olen, Belgium.
- [39] **PerkinElmer instruments**, 801 S.Illinois Ave, Oak Ridge, TN.37830.
- [40] Schönert S, **Analysis of background contributions from support structure**, talk at GERDA collaboration meeting, Dubna, June 2005.
- [41] Budjáš D et al., **Gamma-ray spectrometry of ultra low levels of radioactivity within the material screening program for the GERDA experiment**, Appl. Radiat. Isotopes, doi:10.1016/j.apradiso.2009.01.019., 2009.
- [42] Budjáš D, et al., **Highly Sensitive Gamma-Spectrometers of GERDA for Material Screening: Part 1**, arXiv:0812.0723v1, [physics.ins-det], 2008.
- [43] Leonard D S et al., **Systematic study of trace radioactive impurities in candidate construction materials for EXO-200**, SLAC-Pub-12916, 2007.
- [44] Gibbons D F, **Thermal expansion of some crystals with the diamond structure**, Physical review, Vol.112, No.1, 1958.

- [45] **Useful thermal and mechanical properties**, www.yutopian.com/Yuan/prop.
- [46] Knoll G F, **Radiation detection and measurement**, second edition, John Wiley & Sons, Inc., 1989.
- [47] Schönert S, **LENS:Spectroscopy of low energy solar neutrinos**, ICHEP 2000, Osaka, 2000.
- [48] Barnabé Heider M et al., **Measurements of the leakage current of a phase I prototype detector operated in liquid argon in response to γ radiation**, GERDA Scientific and Technical Report, GSTR-07-005, 2007.
- [49] **GammaVision-32 v6.08**, Gamma Spectrum Analysis Software, <http://www.ortec-online.com/pdf/a66.pdf>.
- [50] **Poligrat GmbH**, Paul-Ehrlich-Strasse 13, D-63322 Rödermark, Germany.
- [51] Guazzoni C, **Fundamentals of Pulse Processing and Noise Filtering in Radiation Detectors**, Talk at Bonn University, 2003.
- [52] Lancashire R J, **The JSpecView Project: an Open Source Java viewer and converter for JCAMP-DX, and XML spectral data files**, Chemistry Central Journal, Vol.1, 2007.
- [53] D'Andragora A. et al., **Results of the cold charge sensitive preamplifier tests with SUB detector**, talk at GERDA collaboration meeting, LNGS, June 2008.
- [54] Pullia A et al., **A cryogenic low-noise JFET-CMOS preamplifier for the HPGe detectors of GERDA**, poster at IEEE, Dresden, 2008.
- [55] Doke T, Masuda K, Shibamura E, **Extimination of absolute photon yields in liquid argon and xenon for relativistiv (1 MEV) electrons**, Nucl. Inst. Meth., Section A, Vol.291, pp.617-620, 1990.
- [56] Di Vacri A, **Report on the MAXWELL 2D electrostatic model of the GERDA prototype detector operated in infrared shield**, GERDA Scientific and Technical Report, GSTR-07-008, 2007.
- [57] Agostinelli S et al., **Geant4 - a simulation toolkit**, Nucl. Instr. Meth. A, Vol.506, pp.250-303, 2003.
- [58] Barnabé Heider M et al., **Notes on the dependence of the reverse current of a naked Ge crystal operated in liquid argon, on the ionization rate of the surrounding liquid argon**, GERDA Scientific and Technical Report, GSTR-07-009, 2007.

- [59] Doke T et al., **Absolute scintillation yields in Liquid Argon and Xenon for various particles**, Japanese Journal of Applied Physics, Vol.41, pp.1538, 2002.
- [60] Di Vacri A, **Update of the empirical interpretative model of the γ -ray induced leakage current (LARIILC)**, talk at GERDA collaboration meeting, Krakow, February 2008.
- [61] Pacchioni G, Skuja L and Griscom D L, **Defects in SiO₂ and related dielectrics: Science and Technology**, NATO Science Series, 2000; Moazzami R and Hu C, **Stress induced current in thin silicon dioxide films**, Int Electron Dev Meeting, pp.139-142, 2000; Bhattacharyya A, **The leakage current in an SiO₂/Si₃N₄/SiO₂ interpoly dielectric layer in EPROM devices**, J. Phys. D: Appl. Phys., Vol. 21, pp.1287-1290, 1988.
- [62] Sze S M, Kwok K Ng, **Physics of Semiconductor Devices**, Third Edition, John Wiley & Sons, Inc., 2006.
- [63] Schroder D K, **Contactless surface charge semiconductor characterization**, Material Science and Engineering B91-92, pp.196-210, 2002.
- [64] Tretyak V I , Zdesenko Yu G, **Atomic Data and Nuclear Data Tables**, Vol.80, pp.83-116, 2002.
- [65] Ekström L P and Firestone R B, **WWW Table of Radioactive Isotopes**, database version 2/28/99 from URL <http://ie.lbl.gov/toi>.
- [66] Maier B, **Der Ausbau des Heidelberg-Moskau Doppelbetaexperimentes auf fünf angereicherte ⁷⁶Ge-Detektoren und quantitative Beschreibung des Untergrundes**, Dissertation, MPI-Heidelberg, 1995.
- [67] Petry F, **Erweiterung des Heidelberg-Moskau Experiments um zwei angereicherte Low-Background ⁷⁶Ge-Detektoren und Entwicklung einer digitalen Pulsformanalyse zur Untergrundidentifikation bei Germanium-Detektoren**, Dissertation, MPI-Heidelberg, 1995.
- [68] Hellmig J, **Elektronik und Auswertung des HEIDELBERG-MOSKAU- $\beta\beta$ -Experiments**, Dissertation, MPI-Heidelberg, 1996.
- [69] Majorovits B, **High Purity Germanium detectors for the search of rare events: Background discrimination and future prospects with the GENIUS project**, Dissertation, MPI-Heidelberg, 2000.

- [70] Dietz A, **Auswertung des neutrinolosen Doppelbetazerfalls von ^{76}Ge im Heidelberg-Moskau-Experiment mit verbesserten statistischen Methoden**, Dissertation, MPI-Heidelberg, 2003.
- [71] Zuber K, **Angereicherte Ge-Detektoren zur Untersuchung teilchenphysikalischer Fragestellungen**, Dissertation, MPI-Heidelberg, 1992.
- [72] Avignone F T et al., **Theoretical and experimental investigation of cosmogenic radioisotope production in germanium**, Nucl. Phys. B (Proc. Suppl.), Vol.28A, pp.280-285, 1992.
- [73] Avignone F T, **Private communication**, 2005.
- [74] **3M Deutschland GmbH**, Hauptverwaltung, Carl-Schurz-Str. 1, 41453 Neuss.
- [75] Bauer M et al., **MaGe: a Monte Carlo Framework for the Gerda and Majorana double beta decay experiments**, J. Phys. Conference Series 39, Vol.362, 2006.
- [76] Chan Y D et al., **MaGe - a Geant4-based Monte Carlo framework for low-background experiments**, arXiv:0802.0860v1[nucl-ex], 2008.

Appendix A

Heidelberg-Moscow and IGEX cryostats and
detector holders

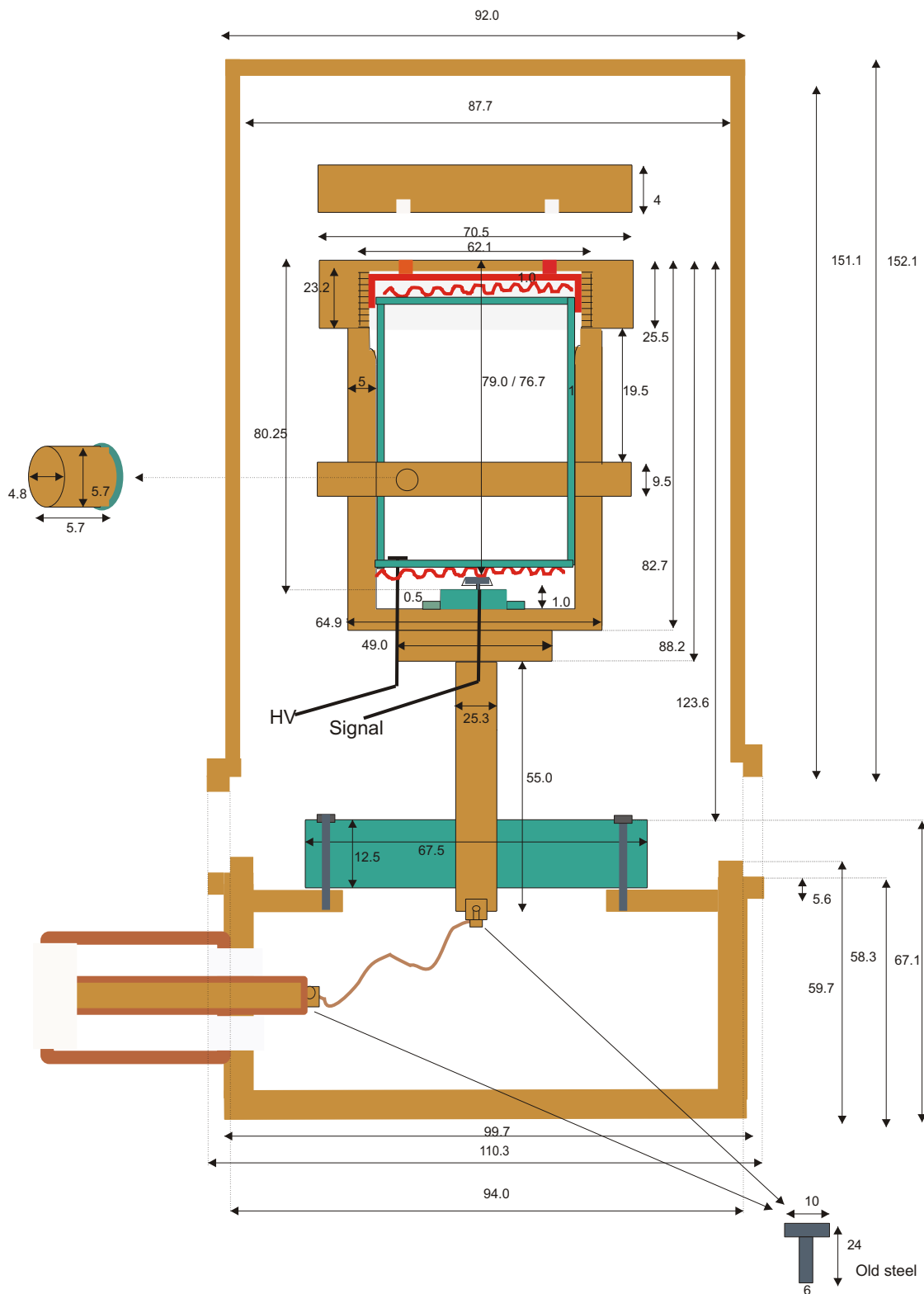


Figure A.1: Drawing of ANG 1 cryostat and detector holder.

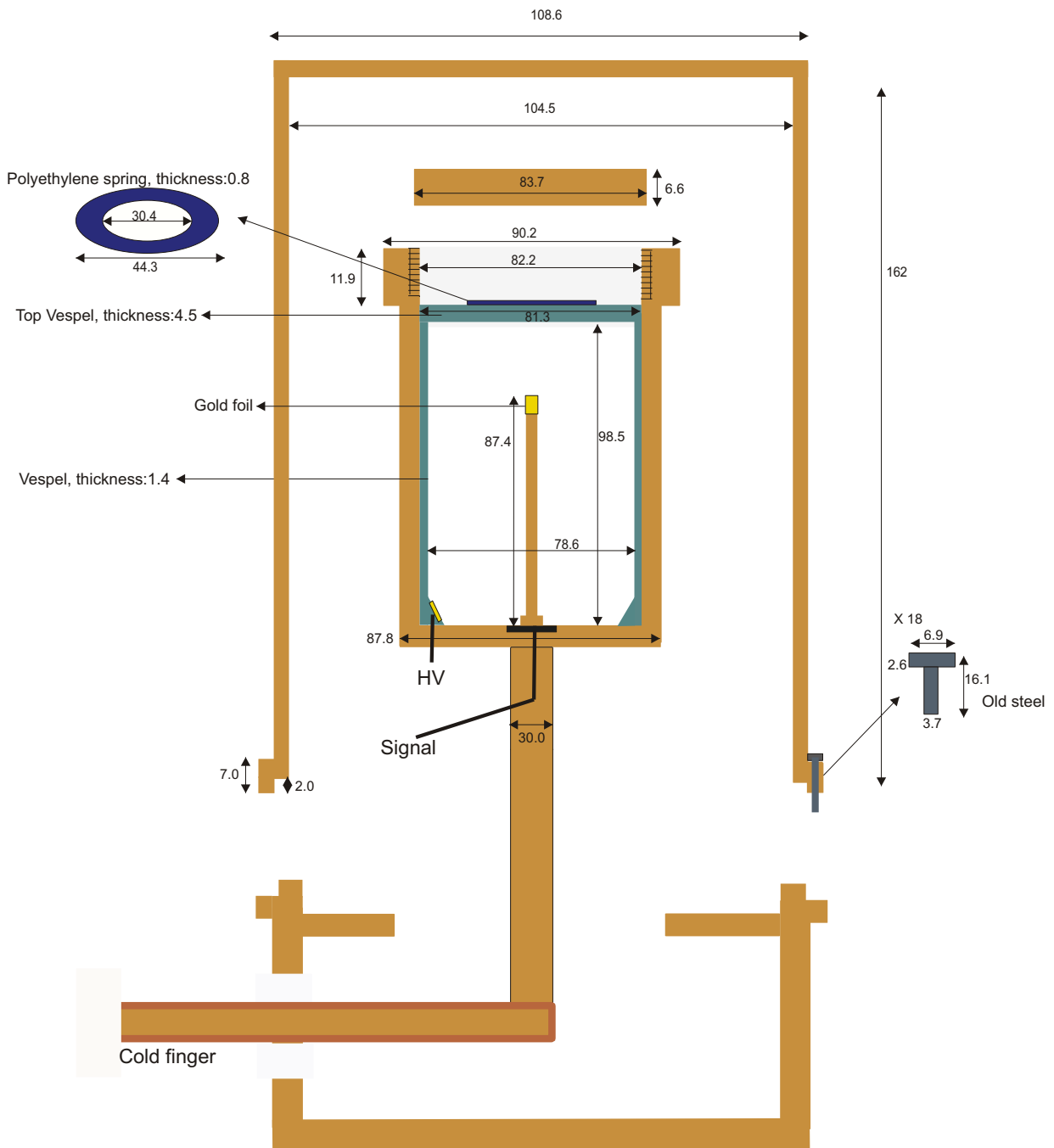


Figure A.3: Drawing of ANG 3 cryostat and detector holder.

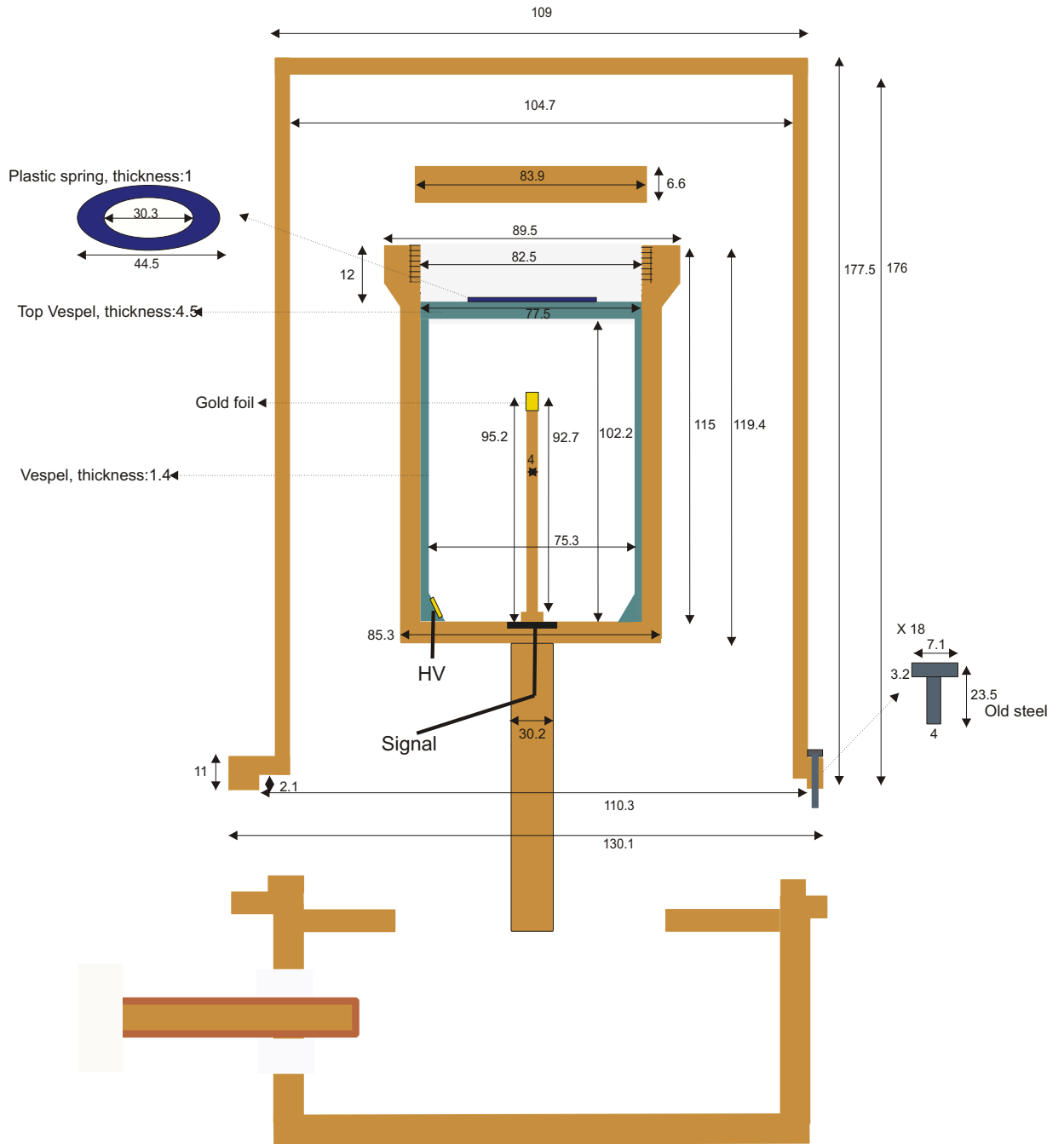


Figure A.4: Drawing of ANG 4 cryostat and detector holder.

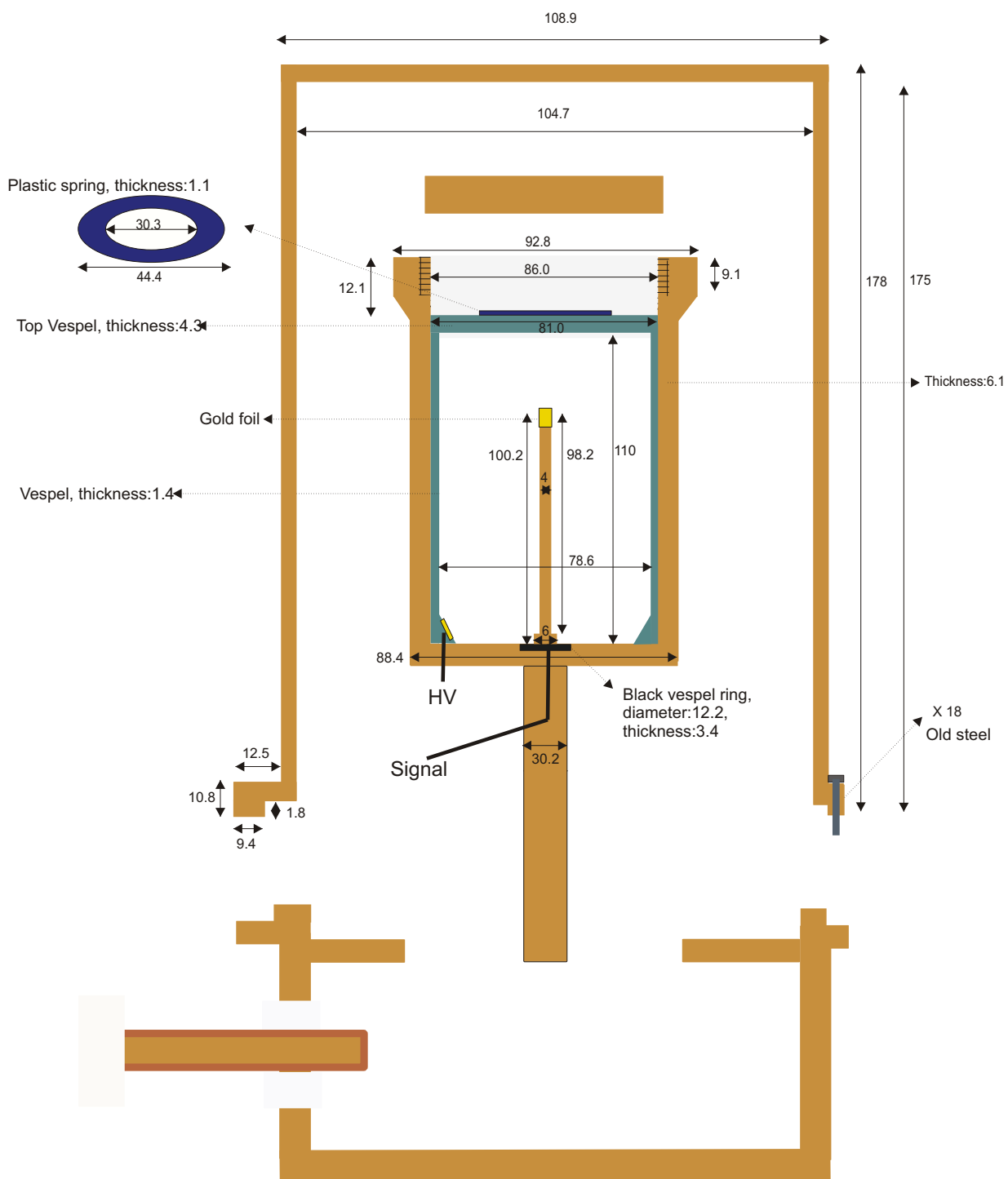


Figure A.5: Drawing of ANG 5 cryostat and detector holder.

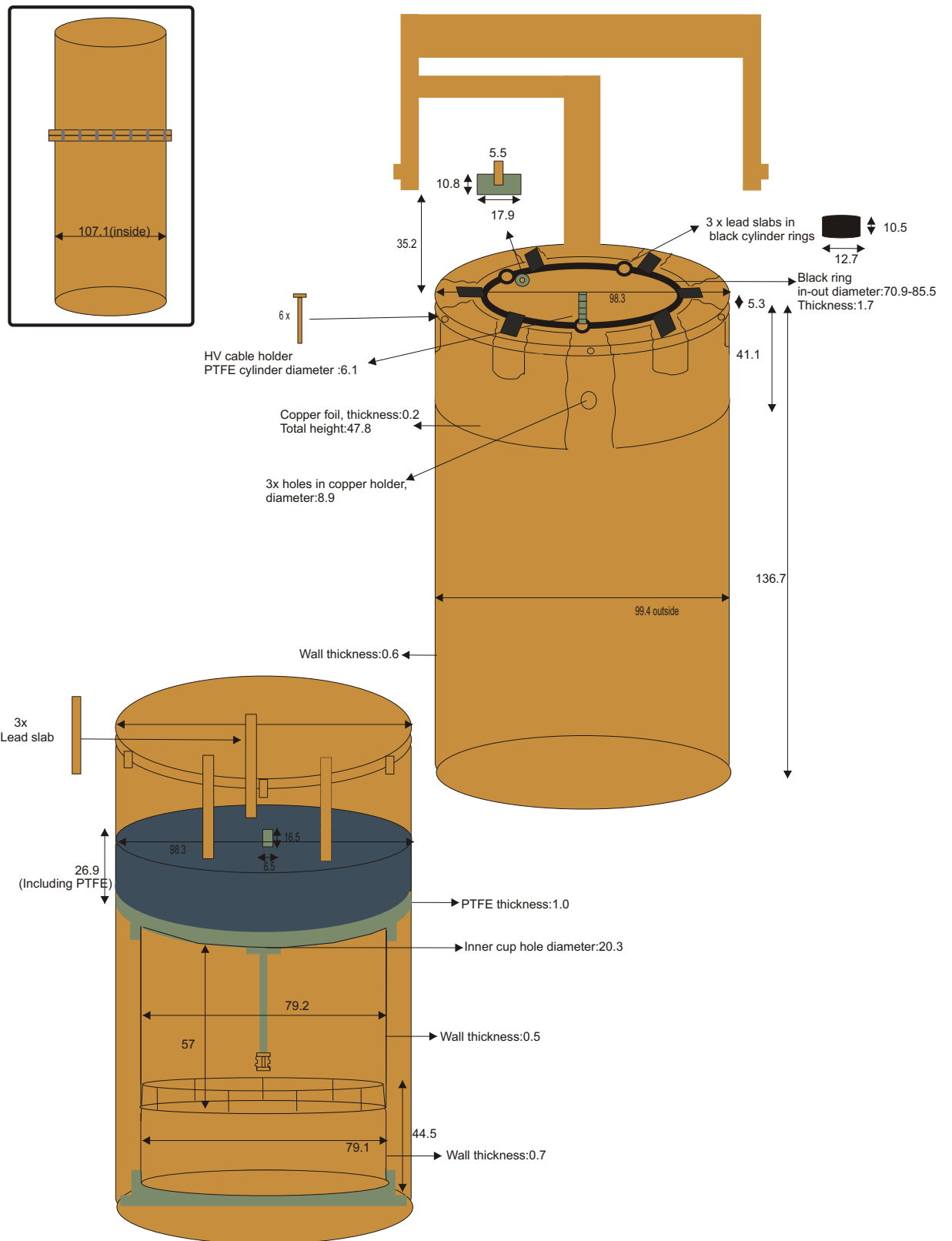


Figure A.6: Drawing of RG 1 cryostat and detector holder.

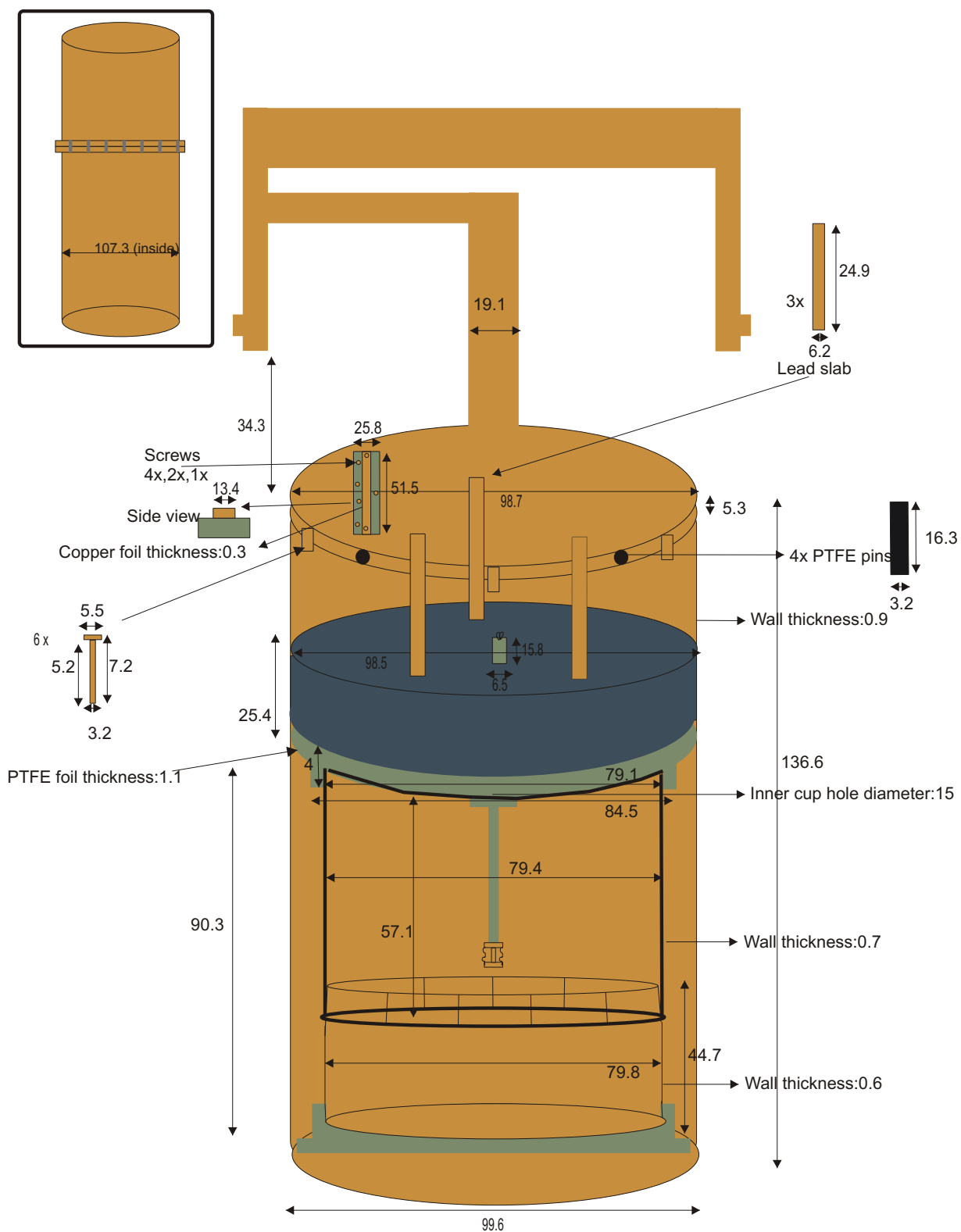


Figure A.7: Drawing of RG 2 cryostat and detector holder.

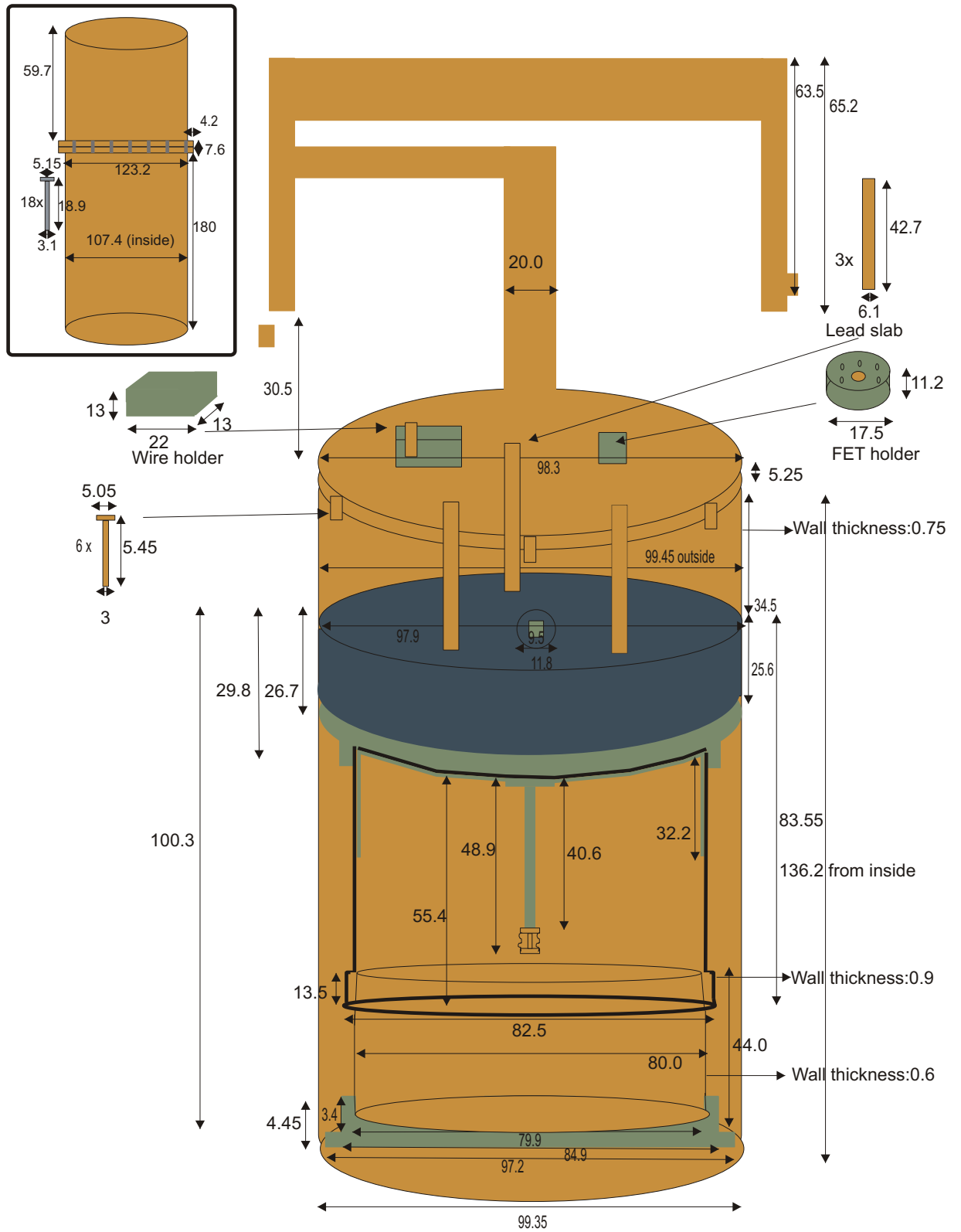


Figure A.8: Drawing of RG 3 cryostat and detector holder.

Appendix B

Phase-I detector holders and contacts

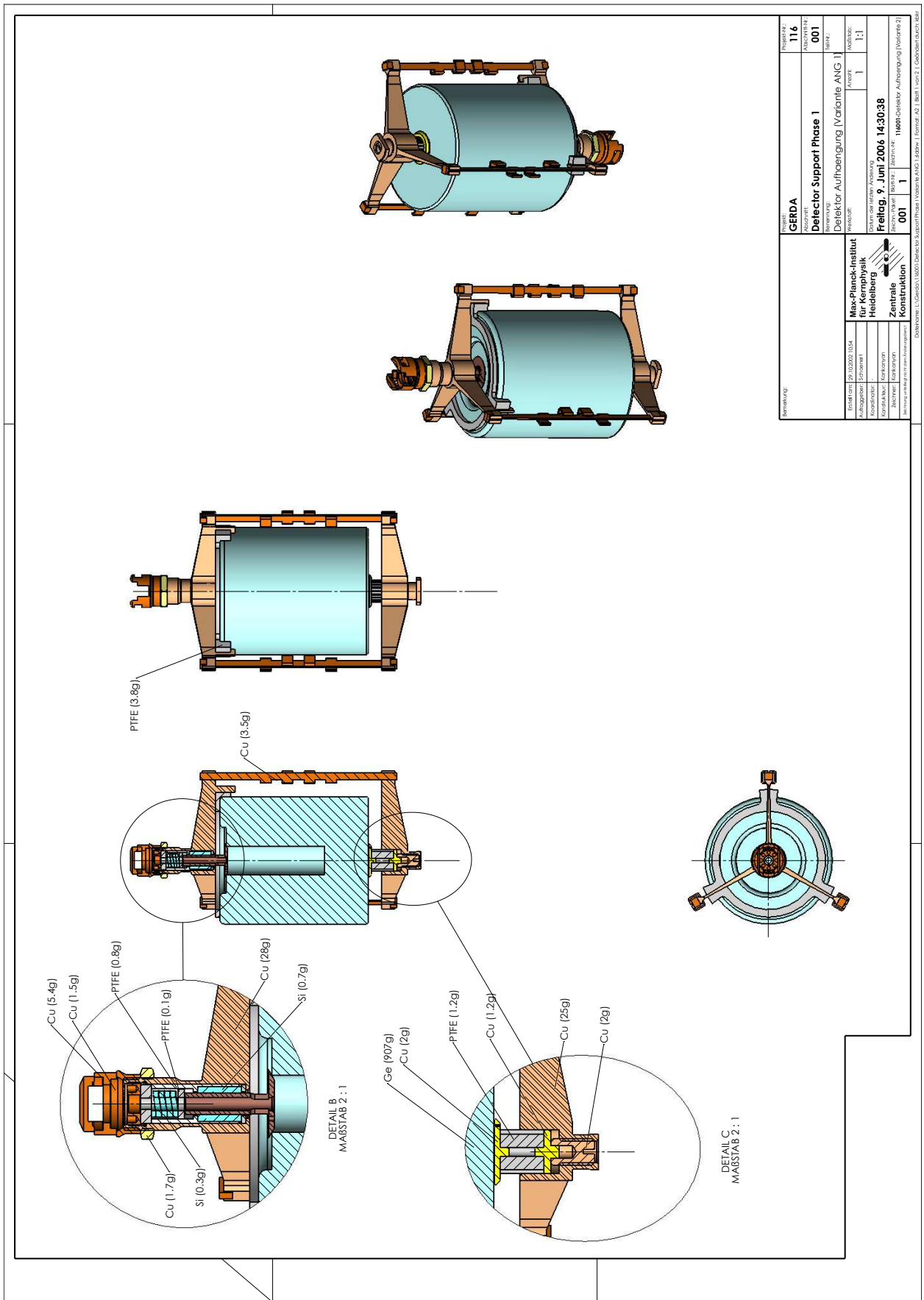


Figure B.1: ANG 1 detector holder and contacts

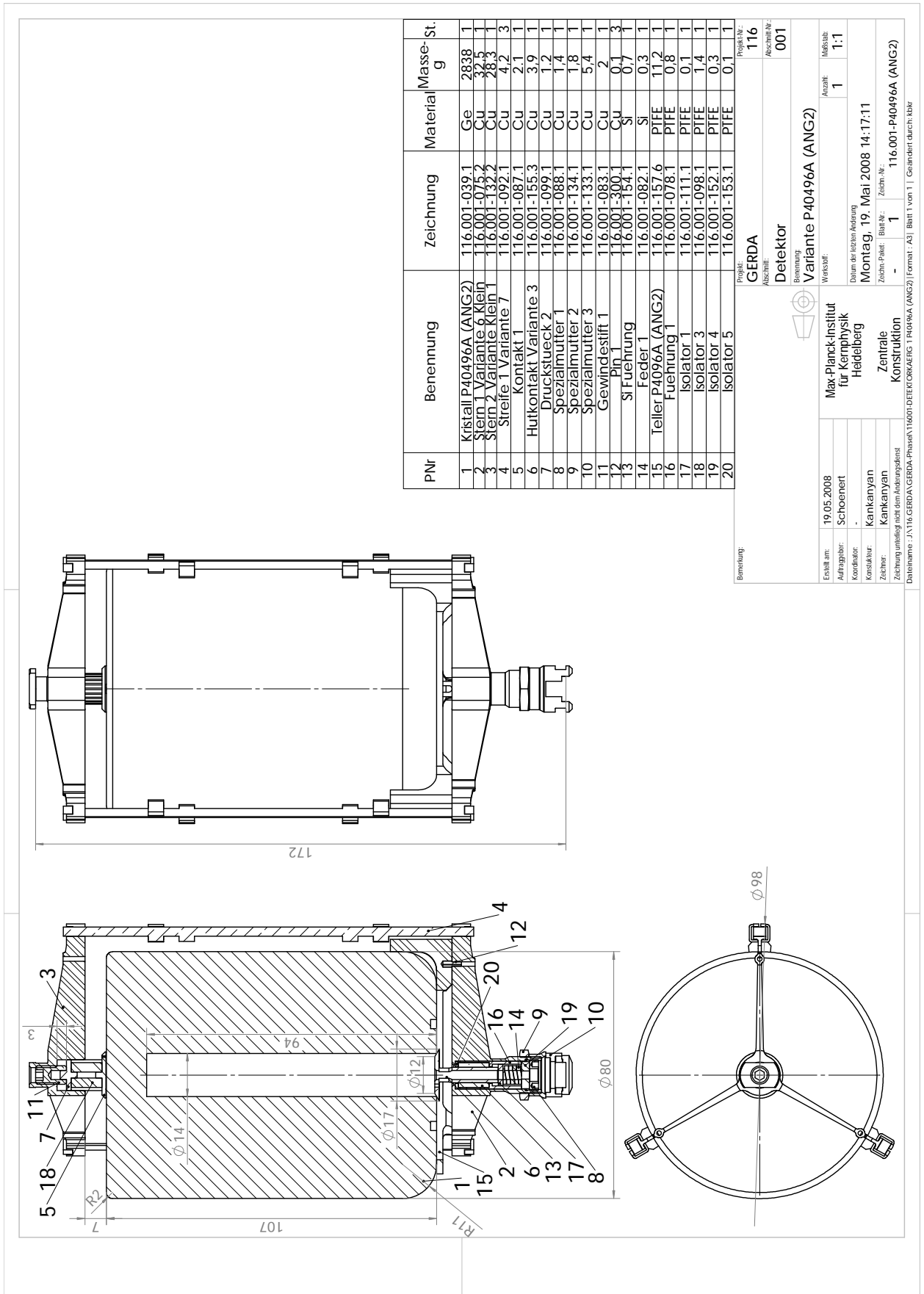
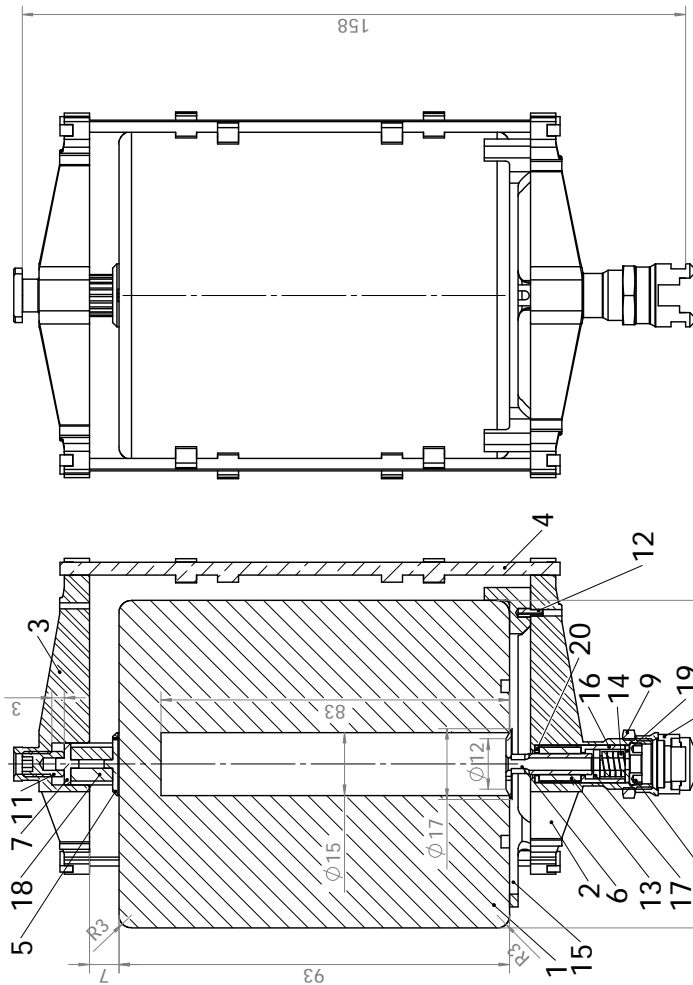


Figure B.2: ANG 2 detector holder and contacts



PNr	Benennung	Zeichnung	Material	Masse- St.
1	Kristall P40270A (ANG3)	16.001-039.1	Ge	2399
2	Stein Variante Klein	16.001-035.2	Cu	26.5
3	Stein 2 Variante Klein	16.001-032.2	Cu	29.3
4	Streifen Variante 14	16.001-082.2	Cu	21
5	Kontakt Variante 1	16.001-087.1	Cu	21
6	Hulkontakt Variante 3	16.001-087.2	Cu	3.9
7	Drahtkontakt 2	16.001-088.3	Cu	3.9
8	Spezialmutter 1	16.001-088.1	Cu	1.4
9	Spezialmutter 2	16.001-088.1	Cu	1.4
10	Spezialmutter 3	16.001-134.1	Cu	1.8
11	Gewindestift 1	16.001-133.1	Cu	5.4
12	Pin 1	16.001-083.1	Cu	2
13	SI Fuehrung	16.001-300.1	Cu	0.1
14	SI Fuehrung	16.001-154.1	Si	0.7
15	Feder 1	16.001-082.1	Si	0.3
16	eller P40270A (ANG3)	16.001-157.4	PIFE	5.6
17	Fuehrung 1	16.001-078.1	PIFE	0.8
18	isolator 1	16.001-111.1	PIFE	0.1
19	isolator 2	16.001-098.1	PIFE	1.1
20	isolator 3	16.001-098.1	PIFE	0.4
20	isolator 3	16.001-153.1	PIFE	0.3

Bemerkung

Projekt: GERDA
 Abschritt: 116
 Defektor
 Benennung: Variante P40270A (ANG3)
 Werkstoff: 

Esellt am: 19.05.2008
 Auftraggeber: Schoenert
 Koordinator: -
 Konstruktor: Kankanyan
 Zeichner: Kankanyan
 Zeichnung umfasst nicht dem Änderungsläng

Max-Planck-Institut
 für Kernphysik
 Heidelberg
 Montag, 19. Mai 2008 14:25:55
 Zeichn. Paket: Blatt Nr.: -
 Zeichn. Nr.: 116.001-P40270A (ANG3)
 Konstruktions
 Blatt Nr.: 1
 Projekt-Nr.: 116
 Anzahl: 1
 Maßstab: 1:1

Datum der letzten Änderung
 Zeichn. Paket: Blatt Nr.: -
 Zeichn. Nr.: 116.001-P40270A (ANG3)
 Konstruktions
 Blatt Nr.: 1
 Projekt-Nr.: 116.001-P40270A (ANG3)

Dateiname: J:\116.GERDA\GERDA-Phase\116001-DEFektor\ANG3 [Format: A3] [Blatt 1 von 1] | Geändert durch: kkr

Figure B.3: ANG 3 detector holder and contacts

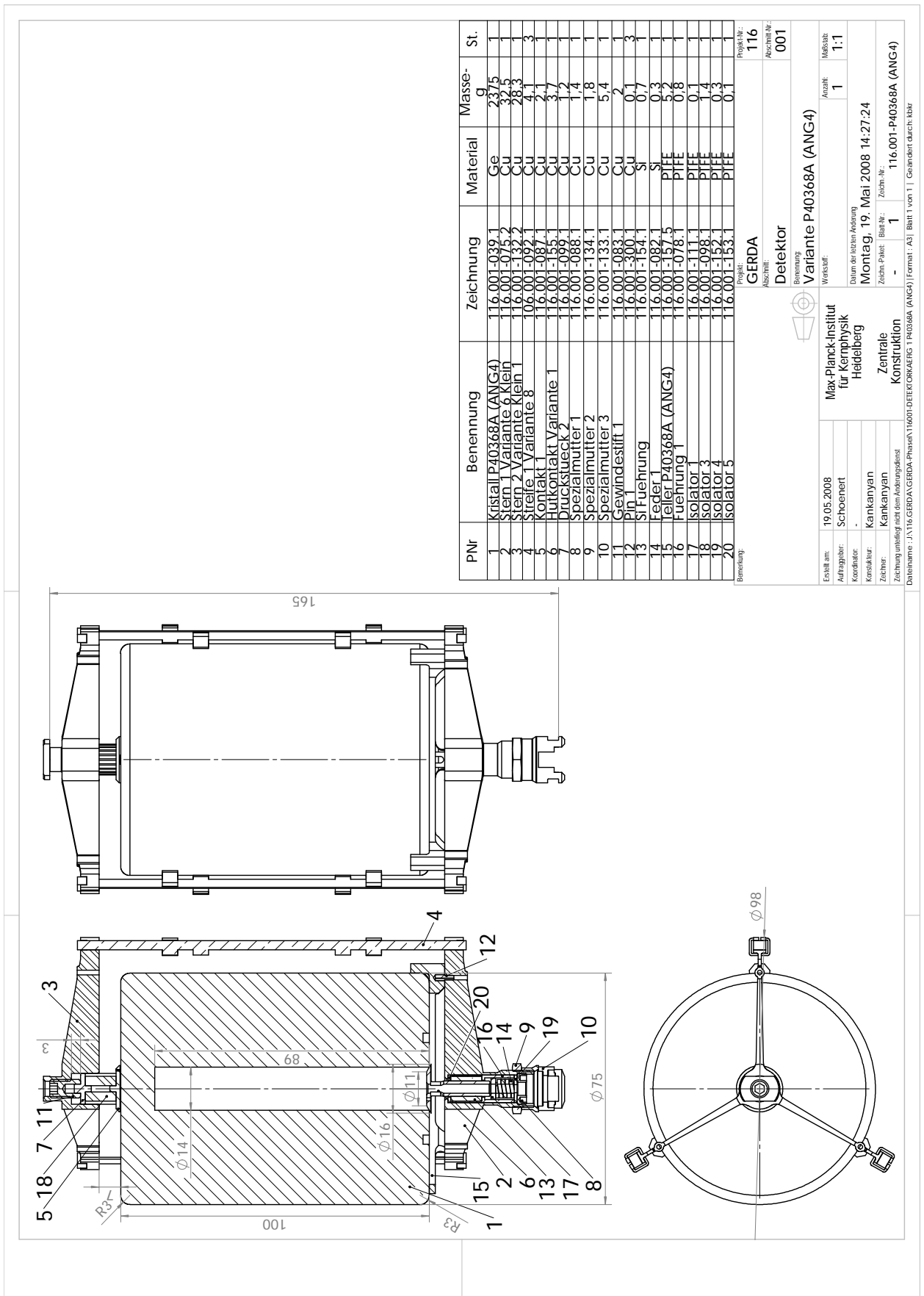


Figure B.4: ANG 4 detector holder and contacts

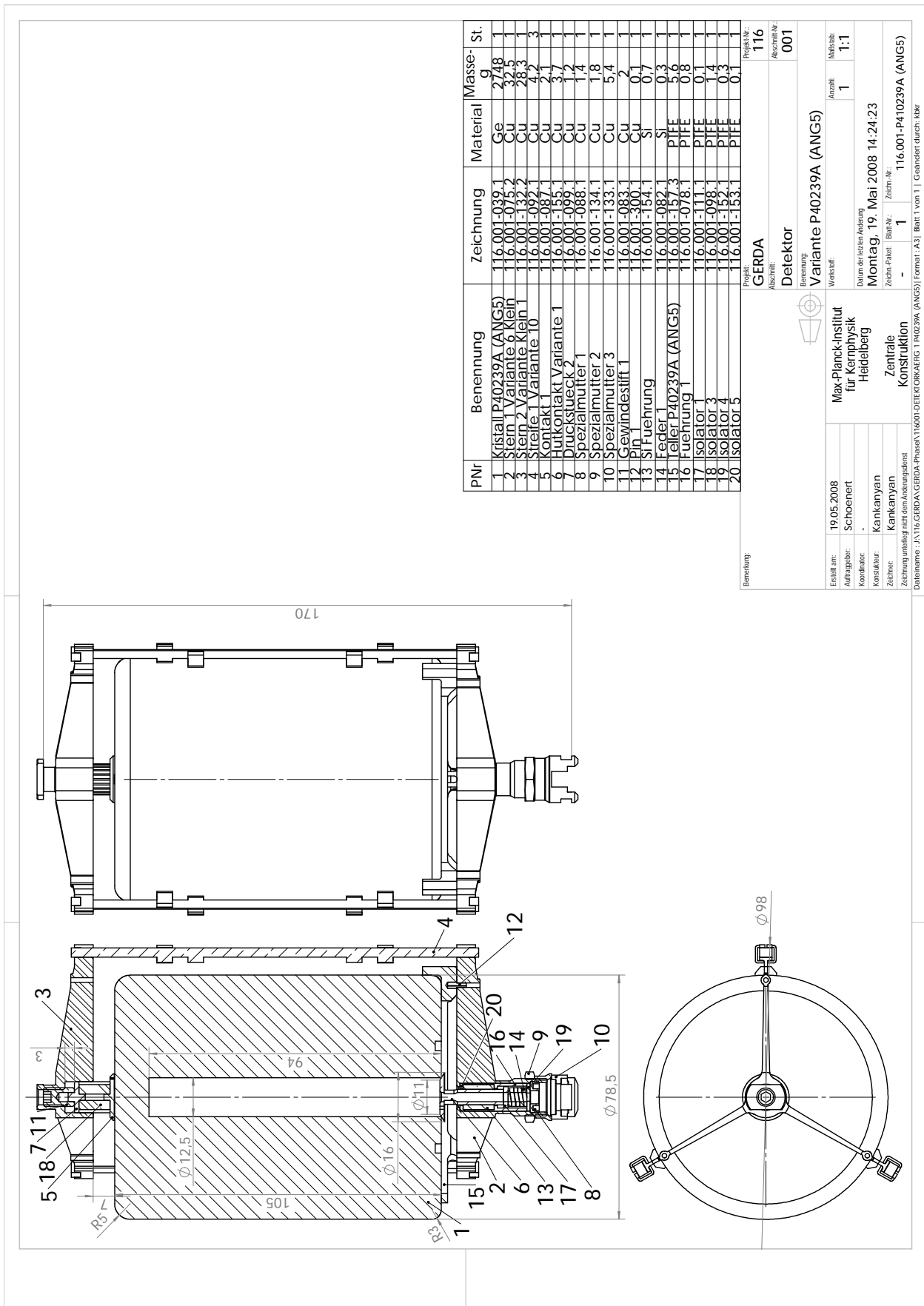


Figure B.5: ANG 5 detector holder and contacts

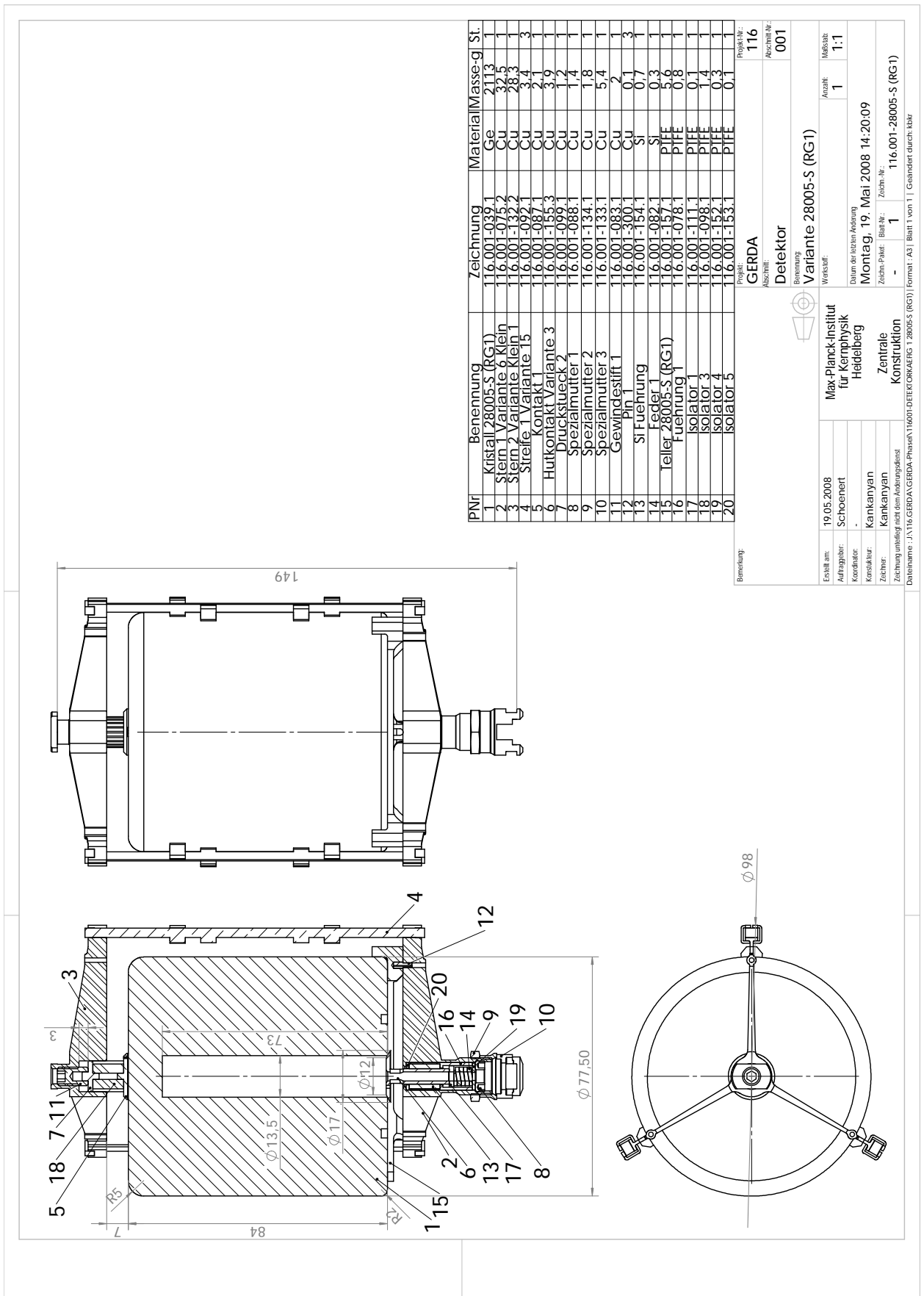
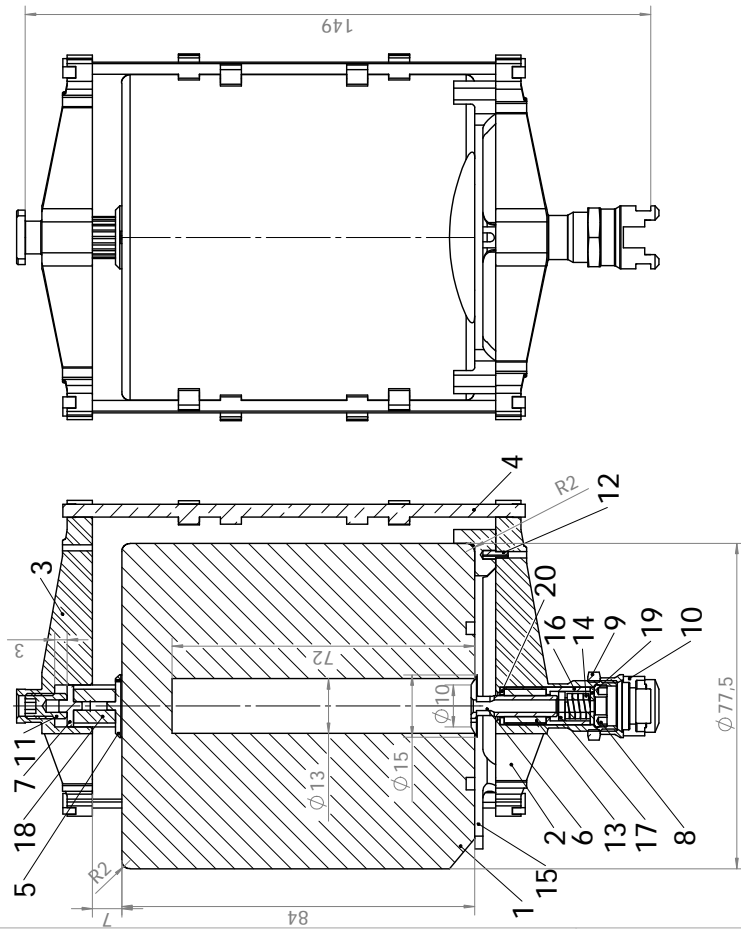


Figure B.6: RG 1 detector holder and contacts



PNr	Benennung	Zeichnung	Material	Masse- g	St.
1	Kristall 28006-S (RG2)	116.001-039.1	Ge	21,68	1
2	Stein 1 Variante Klein	116.001-075.2	Cu	32,5	1
3	Stein 2 Variante Klein 1	116.001-132.2	Cu	28,3	1
4	Streife 1 Variante 15	116.001-092.1	Cu	3,8	3
5	Kontakt 1	116.001-087.1	Cu	2,1	1
6	Hutkontakt Variante 4	116.001-155.4	Cu	3,4	1
7	Druckstueck 2	116.001-099.1	Cu	1,2	1
8	Spezialmutter 1	116.001-088.1	Cu	1,4	1
9	Spezialmutter 2	116.001-134.1	Cu	1,8	1
10	Spezialmutter 3	116.001-133.1	Cu	5,4	1
11	Gewindestift 1	116.001-083.1	Cu	2	1
12	Pin 1	116.001-300.1	Cu	0,1	3
13	SI Fuehrung	116.001-154.1	Si	0,7	1
14	Feder 1	116.001-082.1	Si	0,3	1
15	Teller 28005-S (RG1)	116.001-157.1	PIFE	3,6	1
16	Fuehrung 1	116.001-078.1	PIFE	0,8	1
17	Isolator 1	116.001-111.1	PIFE	0,1	1
18	Isolator 3	116.001-098.1	PIFE	1,4	1
19	Isolator 4	116.001-152.1	PIFE	0,3	1
20	Isolator 5	116.001-153.1	PIFE	0,1	1

Bemerkung

Projekt: GERDA
 Abschil.: 116
 Abschnitt-Nr.: 001

Benennung: Detektor
 Variante 28006-S (RG2)

Werkstoff:

Anzahl: 1
 Maßstab: 1:1

Max-Planck-Institut
 für Kernphysik
 Heidelberg

Datum der letzten Änderung: Montag, 19. Mai 2008 14:21:46

Zeichn. Palet.: -
 Blatt-Nr.: 1
 Zeichn.-Nr.: 116.001-28006-S (RG2)

Zentrale
 Konstruktion

Datenname: J:\116.GERDA\GERDA-Phase\116001-DETEKTOR\AEIG_1_28006_S (RG2) | Format: A3 | Blatt 1 von 1 | Gezeichnet durch: KBR

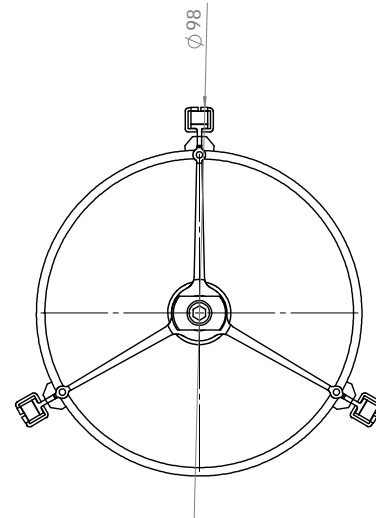


Figure B.7: RG 2 detector holder and contacts

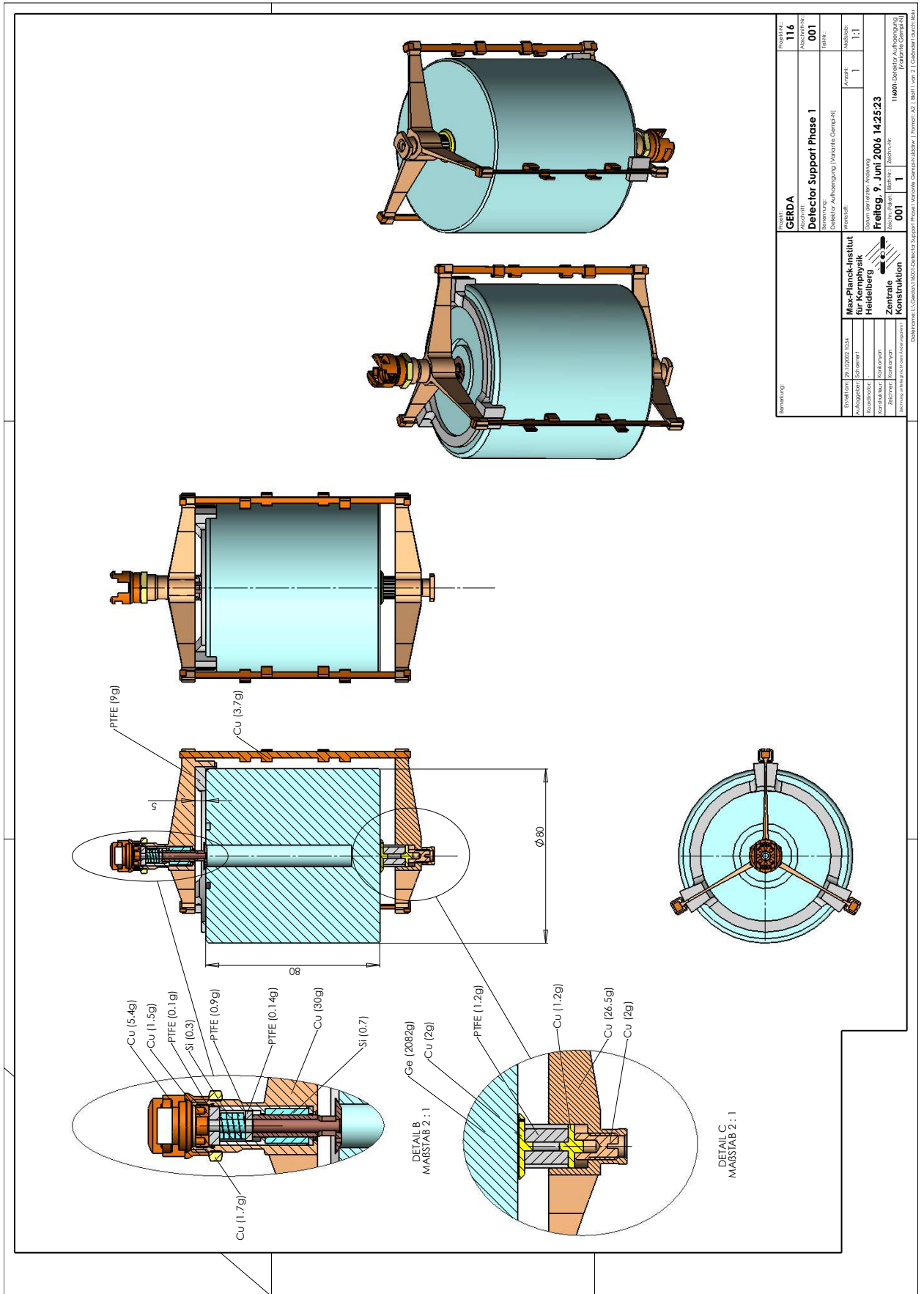


Figure B.8: RG 3 detector holder and contacts